

**Determination of paracetamol at the electrochemically reduced graphene oxide-metal nanocomposite modified pencil graphite (ERGO-MC-PGE) electrode using adsorptive stripping differential pulse voltammetry**



**UNIVERSITY** *of the*  
**WESTERN CAPE**

A thesis submitted in fulfillment of the requirement for the degree of

**Magister Scientiae in Nanoscience (Chemistry)**

Department of Chemistry: SensorLab

University of the Western Cape

October 2019

**By**

**Zandile Dennis Leve**

Supervisor: Prof. N. Jahed

Co-supervisor: Prof. E. Iwuoha

## KEYWORDS

Graphene

Graphene oxide

Pencil graphite electrode

Electrochemically reduced graphene oxide pencil graphite electrode

Electrochemically reduced graphene oxide-antimony nanocomposite pencil graphite electrode

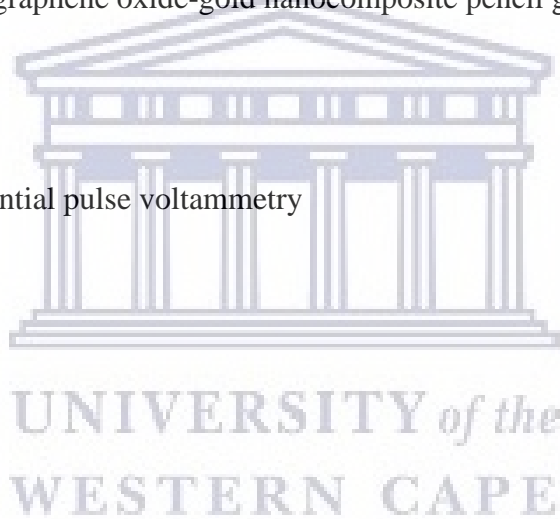
Electrochemically reduced graphene oxide-gold nanocomposite pencil graphite electrode

Cyclic voltammetry

Adsorptive stripping differential pulse voltammetry

Electro-oxidation

Paracetamol



## ABSTRACT

This project focuses on the development of simple, highly sensitive, accurate, and low cost electrochemical sensors based on the modification of pencil graphite electrodes by the electrochemical reduction of graphene oxide-metal salts as nanocomposites (ERGO-MC-PGE; MC = Sb or Au nanocomposite). The electrochemical sensors ERGO-Sb-PGE and ERGO-Au-PGE were used in the determination of paracetamol (PC) in pharmaceutical formulations using adsorptive stripping differential pulse voltammetry. The GO was prepared from graphite via a modified Hummers' method and characterized by FTIR and Raman spectroscopy to confirm the presence of oxygen functional groups in the conjugated carbon-based structure whilst, changes in crystalline structure was observed after XRD analysis of graphite and GO. Morphological differences were also analyzed using HRTEM in which exfoliation of graphite into few layers of GO were observed. Furthermore, HRSEM was used to indicate the presence of electrochemically reduced metal nanoparticles (MNPs) between unmodified and modified pencil graphite electrodes. Cyclic voltammetry in conjunction with HRSEM was used in to reveal the presence of MNPs. The parameters namely, deposition time and number of deposition cycles that were used for the electro-deposition of GO-metal salts were optimized for preparing ERGO-Sb-PGE and ERGO-Au-PGE, and characterized electrochemically using CV and EIS in  $K_3[Fe(CN)_6]$  in  $0.1 \text{ mol.L}^{-1}$  KCl solution. Electro-oxidation of PC at the ERGO-Sb-PGE and ERGO-Au-PGE was achieved by adsorptive stripping differential pulse voltammetric analysis at a potential of -0.7 V in  $0.1 \text{ mol.L}^{-1}$  PBS at  $\text{pH} = 7.0$ . The optimum current response was used to record the detection limits for PC, which were found to be  $0.57 \text{ nmol.L}^{-1}$  and  $11.0 \text{ nmol.L}^{-1}$  at ERGO-Sb-PGE and ERGO-Au-PGE, respectively. The electrochemical sensors were further used in real sample analysis of PC in a commercially available pharmaceutical tablet (500 mg PC). The percentage recovery of PC was between 98.3 % and 101.6 % for ERGO-Sb-PGE, and between 97.7 % and 101.06 % for ERGO-Au-PGE.

## DECLARATION

I declare that this work “**Determination of paracetamol at the electrochemically reduced graphene oxide-metal nanocomposite pencil graphite electrode using adsorptive stripping differential pulse voltammetry**” is my own work, that has not been submitted for any degree or examination at any universities and that all the sources I have used or quoted have been properly indicated and acknowledged by complete references.



**Zandile Dennis Leve**

**October 2019**

**Signature.....**

A handwritten signature in black ink, appearing to be "Z. Leve".

.....

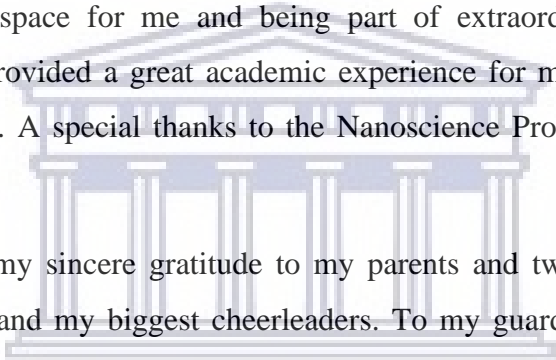
## ACKNOWLEDGEMENTS

To God be the glory, I thank You for always guiding me, giving me strength, perseverance, endurance, and instilling patience within me. Thank You for giving me purpose during this difficult period, and I pray that You will continue to do the same always.

To my supervisor Prof. Jahed, I am grateful for the great opportunity and wisdom you have given to me and thankful for always challenging me intellectually, it continues to groom me to be a better researcher and student. A huge gratitude to Dr. Pokpas for guiding me and sharing your academic insight, I am truly grateful.

I would also like to thank my co-supervisor Prof. Iwuoha and the whole SensorLab research group for creating a workspace for me and being part of extraordinary researchers at the Chemistry department. It provided a great academic experience for me and I hope you do the same for future researchers. A special thanks to the Nanoscience Programme for the financial support.

Lastly, I would to extend my sincere gratitude to my parents and two brothers for being my pillar, my support system, and my biggest cheerleaders. To my guardian angel my late sister, thank you for believing in me. I thank God for all of you.



UNIVERSITY *of the*  
WESTERN CAPE

## LIST OF ABBREVIATION

AA– Ascorbic acid

ABS – Acetate buffer solution

AdSV – Adsorptive stripping voltammetry

ASV – Anodic stripping voltammetry

BDDE – Boron-doped diamond electrode

BET – Brunauer-Emmett Teller

CAFF – Caffeine

CE – Capillary electrophoresis

CNTs – Carbon nanotubes

CSV – Cathodic stripping voltammetry

CV – Cyclic voltammetry

CVD – Chemical vapour deposition

DPV – Differential pulse voltammetry

EDS – Energy dispersive X-ray spectroscopy

EG – Expanded graphite

EIS – Electrochemical impedance spectroscopy

ERGO-MC-PGE – Electrochemically reduced graphene oxide-metal nanocomposite pencil graphite electrode

FA – Folic acid

FESEM – Field emission scanning electron microscopy



UNIVERSITY of the  
WESTERN CAPE

FTIR – Fourier Transform infrared spectroscopy

GCE – Glassy carbon electrode

GNP – Graphene nano-platelet

GO – Graphene oxide

GO-MNPs – Graphene oxide-metal nanoparticles

HMDE – Hanging mercury drop electrode

HOPG – High oriented pyrolytic graphite

HPLC – High performance liquid chromatography

HRSEM – High resolution scanning electron microscopy

HRTEM – High resolution transmission electron microscopy

ITO – Indium-doped titanium oxide

LOD – Limit of detection

M-GO – Metal graphene oxide

MPa – Mega Pascals

NAPQI – N-acetyl-*p*-benzoquinone imine

NMP – N-methylpyrrolidone

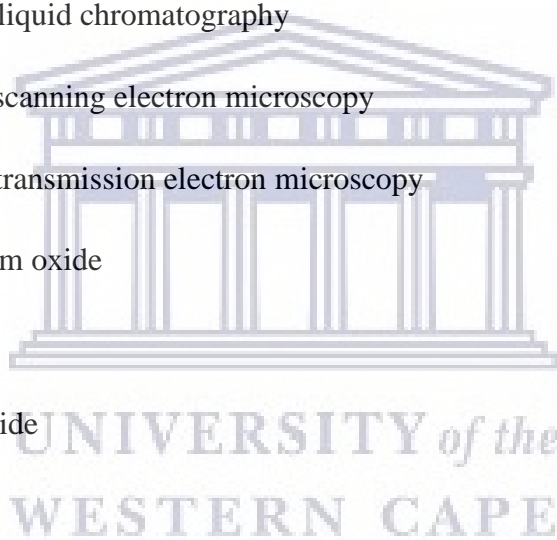
NPs – Nanoparticles

NSAIDs – Non-steroidal anti-inflammatory drugs

OTCs – Over-the-counter drugs

PAH – Polycyclic aromatic hydrocarbon

PBS – Phosphate buffer solution



PC – Paracetamol

PGE – Pencil graphite electrode

PSS – Poly(styrenesulfonate)

QED – Quantum electrodynamics

QHE – Quantum Hall effect

RGO – Reduced graphene oxide

RSD– Relative standard deviation

SAED – Selected area electron diffraction

SAXS – Small-angle X-ray scattering

SCE – Saturated calomel electrode

SDS – Sodium dodecyl sulfate

SEM – Scanning electron microscopy

SG – Single-layer graphene

STDEV – Standard deviation

TEM – Transmission electron microscopy

TGA – Thermogravimetric analysis

TPa – Tetrapascals

UV – Ultraviolet

WAXS – Wide-angle X-ray scattering

XPS – X-ray photon spectroscopy

XRD – X-ray diffraction

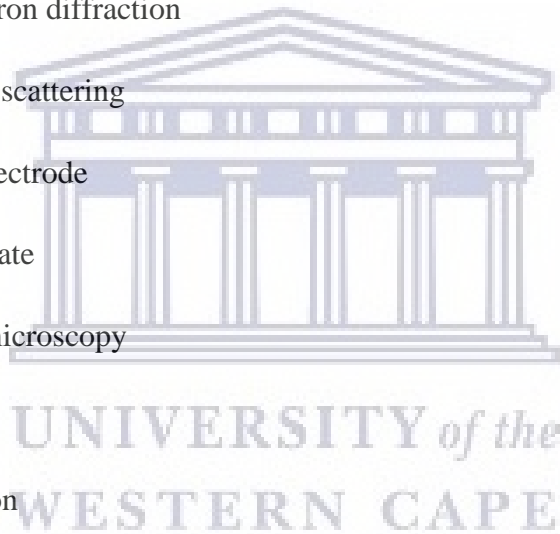
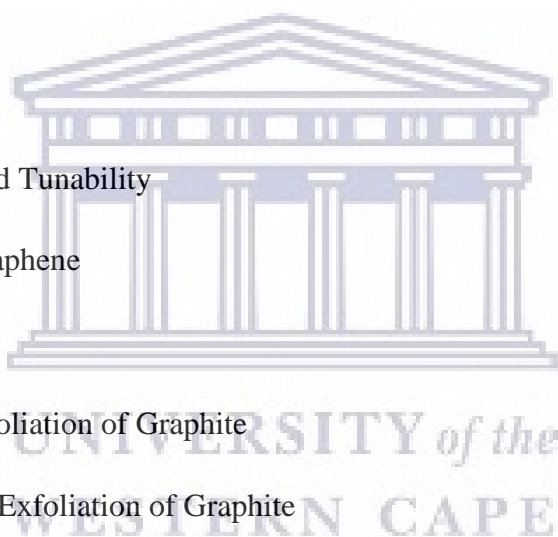


# TABLE OF CONTENTS

<b>KEYWORDS</b>	<b>ii</b>
<b>ABSTRACT</b>	<b>iii</b>
<b>DECLARATION</b>	<b>iv</b>
<b>ACKNOWLEDGEMENTS</b>	<b>v</b>
<b>LIST OF ABBREVIATION</b>	<b>vi</b>
<b>TABLE OF CONTENTS</b>	<b>ix</b>
<b>LIST OF FIGURES</b>	<b>xvi</b>
<b>LIST OF TABLES</b>	<b>xxi</b>
<b>CHAPTER ONE</b>	<b>1</b>
<b>Introduction</b>	<b>1</b>
1.1. Background	1
1.2. Problem Statement	3
1.3. Research Aims and Objectives	4
1.4. Hypothesis	5
1.5. Research Questions	5
1.6. Research Approach	6
1.7. Scope	7
1.8. Delimitations	7
<b>Thesis Outline</b>	<b>8</b>



<b>CHAPTER TWO</b>	<b>10</b>
<b>Literature Review</b>	<b>10</b>
2.1. Introduction	10
2.2. Carbon Allotropes	10
2.3. Structural Properties	12
2.4. Surface Properties	13
2.5. Magnetic Properties	14
2.6. Quantum Properties	14
2.7. Optical Properties	15
2.8. Electrical Properties and Tunability	16
2.9. Synthetic Routes of Graphene	16
2.9.1. Top-Down Method	17
2.9.1.1. Mechanical Exfoliation of Graphite	17
2.9.1.2. Solution-Based Exfoliation of Graphite	18
2.9.1.3. Electrochemical Exfoliation of Graphite	19
2.9.1.4. Chemical Oxidation of Graphite	20
2.9.2. Bottom-Up Methods	21
2.9.2.1. Chemical Synthesis	21
2.9.2.2. Epitaxial Growth on SiC	22
2.9.2.3. Chemical Vapour Deposition	23



2.10. Characterizations	24
2.10.1. FTIR Spectroscopy	24
2.10.2. Raman Spectroscopy	25
2.10.3. XRD	26
2.10.4. SEM and TEM	27
2.11. Graphene Oxide-Metal Nanoparticles	28
2.12. Pencil Graphite Electrode	30
2.13. Cyclic Voltammetry	31
2.14. Electrochemical Impedance Spectroscopy	32
2.15. Electrochemical Stripping Voltammetric Techniques	34
2.15.1. Anodic Stripping Voltammetry	35
2.15.2. Cathodic Stripping Voltammetry	37
2.15.3. Adsorptive Stripping Voltammetry	39
<b>CHAPTER THREE</b>	<b>41</b>
<b>Materials and Methods</b>	<b>41</b>
3.1. Introduction	41
3.2. Reagents and Chemicals	41
3.3. Instrumentation	41
3.4. Synthesis of Graphene Oxide	42
3.5. Preparation of Graphene Oxide-Metal Nanoparticles	43

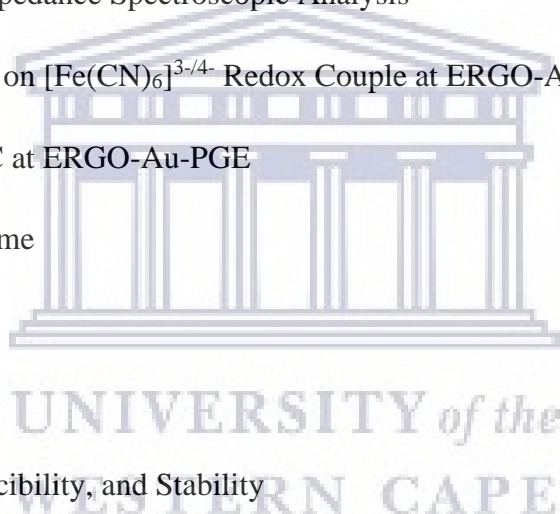
3.6. Electrochemical Treatment of PGEs	43
3.7. Batch Preparation of ERGO-MC-PGEs	44
3.8. Adsorptive Stripping Differential Pulse Voltammetric Analysis of PC at ERGO-MC-PGEs	45
3.9. Characterizations	46
3.9.1. FTIR Spectroscopy	46
3.9.2. Raman Spectroscopy	46
3.9.3. X-ray Diffraction	46
3.9.4. HRSEM	47
3.9.5. HRTEM	47
<b>CHAPTER FOUR</b>	<b>48</b>
<b>Structural and Morphological Characterizations</b>	<b>48</b>
4.1. Introduction	48
4.2. FTIR Spectra	48
4.3. Raman Spectra	49
4.4. X-ray Diffraction	51
4.5. HRSEM	52
4.6. HRTEM	56



UNIVERSITY of the  
WESTERN CAPE

<b>CHAPTER FIVE</b>	<b>58</b>
<b>Electrochemical Oxidation of Paracetamol at the Electrochemically Reduced Graphene Oxide-Antimony Nanocomposite Modified Pencil Graphite Electrode</b>	<b>58</b>
5.1. Introduction	58
5.2. Electrochemical Characterizations	58
5.2.1. Electrochemical Properties	58
5.2.2. Electrochemical Impedance Spectroscopic Analysis	60
5.2.3. Effect of Scan Rate on $[\text{Fe}(\text{CN})_6]^{3-/4-}$ Redox Couple at ERGO-Sb-PGE	61
5.3. Electro-oxidation of PC at ERGO-Sb-PGE	68
5.4. Effect of Deposition Time	69
5.5. Effect of Cycles	71
5.6. Effect of pH	72
5.7. Repeatability, Reproducibility, and Stability	74
5.8. Interference Studies	77
5.9. Limit of Detection	80
5.10. Analytical Application of ERGO-Sb-PGE for PC	82
5.11. Conclusion	84

<b>CHAPTER SIX</b>	<b>86</b>
<b>Electrochemical Oxidation of PC at Electrochemically Reduced Graphene Oxide-Gold Nanocomposite Modified Pencil Graphite Electrode</b>	<b>86</b>
6.1. Introduction	86
6.2. Electrochemical Characterizations	86
6.2.1. Electrochemical Properties	86
6.2.2. Electrochemical Impedance Spectroscopic Analysis	88
6.2.3. Effect of Scan Rate on $[\text{Fe}(\text{CN})_6]^{3-/4-}$ Redox Couple at ERGO-Au-PGE	89
6.3. Electro-oxidation of PC at ERGO-Au-PGE	94
6.4. Effect of Deposition Time	95
6.5. Effect of Cycles	96
6.6. Effect of pH	97
6.7. Repeatability, Reproducibility, and Stability	98
6.8. Interference Studies	101
6.9. Limit of Detection	104
6.10. Analytical Application of ERGO-Au-PGE for PC	105
6.11. Electro-oxidation of PC at Other ERGO-MC-PGEs	107
6.12. Conclusion	109



<b>CHAPTER SEVEN</b>	<b>110</b>
<b>Conclusions and Future Work</b>	<b>110</b>
<b>REFERENCES</b>	<b>112</b>



UNIVERSITY *of the*  
WESTERN CAPE

## LIST OF FIGURES

<b>Figure 1.1:</b> Structure of paracetamol (PC)	2
<b>Figure 2.1:</b> Forms of carbons allotropes [65]	12
<b>Figure 2.2:</b> Schematic of Dirac-cone and interband optical transitions in graphene [96]	15
<b>Figure 2.3:</b> Overview for the production methods of graphene [97, 129]	17
<b>Figure 2.4:</b> FT-IR spectra of GO prepared from (a) commercial and (b) ball-milled graphite [188]	24
<b>Figure 2.5:</b> Raman spectrum of graphene at 0 V (applied bias voltage), excited by a 2.33 eV laser radiation, in an electrochemical environment. The asterisks (*) indicate Raman bands of the electrolyte [97]	25
<b>Figure 2.6:</b> XRD of ball-milled and commercial graphite in (A), and graphite with GO and graphene in (B) [83, 188]	27
<b>Figure 2.7:</b> SEM images of monolayer graphene and aggregated reduced GO sheets, and TEM images of graphene nanosheets [199]	28
<b>Figure 2.8:</b> Cyclic voltammogram of 6 mM $K_3Fe(CN)_6$ in 1 M $KNO_3$ [236]	32
<b>Figure 2.9:</b> Electrochemical impedance spectroscopy demonstration and Nyquist plots obtained with different kinetic parameters in [237]	33
<b>Figure 2.10:</b> Potential-current-time relationships during an anodic stripping voltammetric analysis: accumulation time, rest period, determination or stripping step, anodic dissolution of mercury [238]	37

<b>Figure 2.11:</b> An example showing the differential pulse cathodic and anodic stripping voltammograms of arsenic [238]	38
<b>Figure 2.12:</b> Adsorptive stripping voltammograms of Co and Ni using HMDE [245]	39
<b>Figure 3.1:</b> A 797 VA Computrace voltammetry instrument connected to a personal computer, and the three-electrode system consisting of reference electrode (RE), platinum wire as an auxiliary electrode (AE), and the ERGO-MC-PGE (MC = Au or Sb nanocomposite) as a working electrode (WE)	42
<b>Figure 3.2:</b> A plastic syringe holder with a connected copper wire and a pencil rod	43
<b>Figure 3.3:</b> Batch preparation of ERGO-MC-PGEs; the materials used for the experiment apparatus, an 8-hole cap consisting of 8 PGEs, and the apparatus used	45
<b>Figure 4.1:</b> FTIR spectra of graphite and GO	49
<b>Figure 4.2:</b> Raman spectra of graphite and GO	50
<b>Figure 4.3:</b> XRD spectra of graphite and GO	51
<b>Figure 4.4 (I):</b> HRSEM images of bare PGE, ERGO-PGE, ERGO-Sb-PGE, and ERGO-Au-PGE at different magnifications	54
<b>Figure 4.4 (II):</b> EDS of ERGO-Sb-PGE and ERGO-Au-PGE	55
<b>Figure 4.4 (III):</b> Cyclic voltammetry characterization in 0.5 mol.L <sup>-1</sup> HCl	

at a scan rate of  $50 \text{ mV}\cdot\text{s}^{-1}$  for the electrodes: ERGO-PGE with  
ERGO-Sb-PGE, and ERGO-PGE with ERGO-Au-PGE 56

**Figure 4.5:** HRTEM images of graphite and GO at different scan positions  
and magnification and the corresponding SAED pattern 57

**Figure 5.1:** Cyclic voltammograms of  $5 \text{ mmol}\cdot\text{L}^{-1} [\text{Fe}(\text{CN})_6]^{3-/4-}$  in  $0.1 \text{ mol}\cdot\text{L}^{-1}$   
KCl solution at bare PGE, ERGO-PGE, and ERGO-Sb-PGE at  
a scan rate of  $50 \text{ mV}\cdot\text{s}^{-1}$  59

**Figure 5.2:** Nyquist plot of  $5 \text{ mmol}\cdot\text{L}^{-1} [\text{Fe}(\text{CN})_6]^{3-/4-}$  in  $0.1 \text{ mol}\cdot\text{L}^{-1}$  KCl  
solution at bare PGE, ERGO-PGE, and ERGO-Sb-PGE.  
Insert: Equivalent circuit fitting 61

**Figure 5.3 (I):** CVs of bare PGE in  $5 \text{ mmol}\cdot\text{L}^{-1} [\text{Fe}(\text{CN})_6]^{3-/4-}$  in  $0.1 \text{ mol}\cdot\text{L}^{-1}$   
KCl solution over a scan rate range of  $10 - 100 \text{ mV}\cdot\text{s}^{-1}$  and the  
accompanying linear plots of scan rate and square root of scan rate  
with peak currents along with the plot of  $\ln I_p$  and  $\ln v$  62

**Figure 5.3 (II):** CVs of ERGO-PGE in  $5 \text{ mmol}\cdot\text{L}^{-1} [\text{Fe}(\text{CN})_6]^{3-/4-}$  in  
 $0.1 \text{ mol}\cdot\text{L}^{-1}$  KCl solution over a scan rate range of  $10 - 100 \text{ mV}\cdot\text{s}^{-1}$  and  
the accompanying linear plots of scan rate and square root of scan rate with  
peak currents along with the plot of  $\ln I_p$  and  $\ln v$  63

**Figure 5.3 (III):** CVs of ERGO-Sb-PGE in  $5 \text{ mmol}\cdot\text{L}^{-1} [\text{Fe}(\text{CN})_6]^{3-/4-}$  in  
 $0.1 \text{ mol}\cdot\text{L}^{-1}$  KCl solution over a scan rate range of  $10 - 100 \text{ mV}\cdot\text{s}^{-1}$  and  
the accompanying linear plots of scan rate and square root of scan rate with

peak currents along with the plot of  $\ln I_p$  and  $\ln v$  64

**Figure 5.4:** Differential pulse voltammograms of bare PGE, ERGO-PGE, and ERGO-Sb-PGE in  $0.1 \text{ mol.L}^{-1}$  PBS at pH 7.0 containing  $10 \mu\text{mol.L}^{-1}$  PC solution 69

**Figure 5.5:** Influence of the deposition time on the surface modification of electrode for the electro-oxidation of PC at ERGO-Sb-PGE 70

**Figure 5.6:** Influence of the number of cycles on the surface modification of electrode for the electro-oxidation of PC at ERGO-Sb-PGE 71

**Figure 5.7:** Effect of pH on the electro-oxidation of PC ERGO-Sb-PGE represented by DPV responses and linear plots of current and potential as a function of pH 72

**Figure 5.8 (I):** DPVs obtained on same ERGO-Sb-PGEs, respectively in  $10 \mu\text{mol.L}^{-1}$  PC solution in  $0.1 \text{ mol.L}^{-1}$  PBS for repeatability, reproducibility, and stability, and the accompanying bar graph showing peak current on different days 75

**Figure 5.8 (II):** DPVs obtained on multiple ERGO-Sb-PGEs, respectively in  $10 \mu\text{mol.L}^{-1}$  PC solution in  $0.1 \text{ mol.L}^{-1}$  PBS for repeatability, reproducibility, and stability, and the accompanying bar graph showing peak current on different days 76

**Figure 5.9:** DPV results displaying electro-oxidation of  $10 \mu\text{mol.L}^{-1}$  PC in

0.1 mol.L<sup>-1</sup> PBS (pH = 7.03) at ERGO-Sb-PGE in the presence of  
interferents 78

**Figure 5.10:** DPVs obtained at ERGO-Sb-PGE in 0.1 mol.L<sup>-1</sup>  
PBS (pH 6.98) containing concentrations of PC and the corresponding  
calibration plots 80

**Figure 5.11:** DPV measurements for the recovery of PC at ERGO-Sb-PGE  
with standard additions at different concentrations of sample 83

**Figure 6.1:** CVs of 5 mmol.L<sup>-1</sup> [Fe(CN)<sub>6</sub>]<sup>3-/4-</sup> containing 0.1 mol.L<sup>-1</sup> KCl  
solution at bare PGE, ERGO-PGE, and ERGO-Au-PGE at a scan rate  
of 50 mV.s<sup>-1</sup> 87

**Figure 6.2:** Nyquist plot of [Fe(CN)<sub>6</sub>]<sup>3-/4-</sup> (5 mmol.L<sup>-1</sup>) containing 0.1 mol.L<sup>-1</sup>  
KCl at bare PGE, ERGO-PGE, and ERGO-Sb-PGE 88

**Figure 6.3 (I):** CVs of bare PGE in 5 mmol.L<sup>-1</sup> [Fe(CN)<sub>6</sub>]<sup>3-/4-</sup> in 0.1 mol.L<sup>-1</sup>  
KCl solution over a scan rate range of 10 – 100 mV.s<sup>-1</sup> and the accompanying  
linear plots of scan rate and square root of scan rate with peak currents along  
with the plot of lnI<sub>p</sub> and lnv 89

**Figure 6.3 (II):** CVs of ERGO-PGE in 5 mmol.L<sup>-1</sup> [Fe(CN)<sub>6</sub>]<sup>3-/4-</sup> in  
0.1 mol.L<sup>-1</sup> KCl solution over a scan rate range of 10 – 100 mV.s<sup>-1</sup> and the  
accompanying linear plots of scan rate and square root of scan rate with  
peak currents along with the plot of lnI<sub>p</sub> and lnv 90

**Figure 6.3 (III):** CVs of ERGO-Au-PGE in 5 mmol.L<sup>-1</sup> [Fe(CN)<sub>6</sub>]<sup>3-/4-</sup>

in 0.1 mol.L<sup>-1</sup> KCl solution over a scan rate range of 10 – 100 mV.s<sup>-1</sup> and the accompanying linear plots of scan rate and square root of scan rate with peak currents along with the plot of lnI<sub>p</sub> and lnv 91

**Figure 6.4:** Differential pulse voltammograms of bare PGE, ERGO-PGE, and ERGO-Au-PGE in 0.1 mol.L<sup>-1</sup> PBS at pH 7.0 containing 10 μmol.L<sup>-1</sup> PC solution 95

**Figure 6.5:** Influence of the deposition time on the surface modification of electrode for the electro-oxidation of paracetamol at ERGO-Au-PGE 96

**Figure 6.6:** Influence of the number of cycles on the surface modification of electrode for the electro-oxidation of PC at ERGO-Au-PGE 97

**Figure 6.7:** Effect of pH on the electro-oxidation of PC at ERGO-Au-PGE represented by DPV responses and linear plots of current and potential as a function of pH 98

**Figure 6.8 (I):** DPV measurements obtained on the same ERGO-Au-PGE in 10 μmol.L<sup>-1</sup> PC solution in 0.1 mol.L<sup>-1</sup> PBS for repeatability, reproducibility, and stability and the accompanying bar graph on different days 99

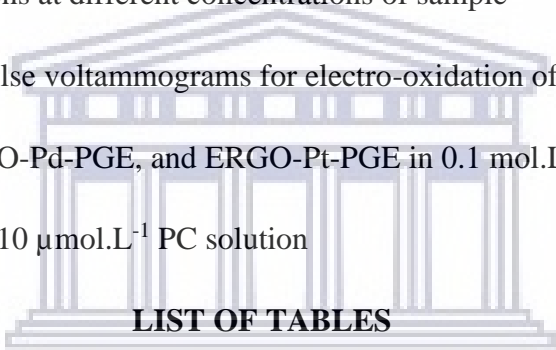
**Figure 6.8 (II):** DPV measurements obtained on multiple ERGO-Au-PGE in 10 μmol.L<sup>-1</sup> PC solution in 0.1 mol.L<sup>-1</sup> PBS for repeatability, reproducibility, and stability and the accompanying bar graph on different days 100

**Figure 6.9:** DPV results showing electro-oxidation of  $10 \mu\text{mol.L}^{-1}$  PC in  $0.1 \text{ mol.L}^{-1}$  PBS (pH = 7.03) at ERGO-Sb-PGE in the presence of interferences at different concentrations 101

**Figure 6.10:** DPVs obtained at ERGO-Au-PGE in  $0.1 \text{ mol.L}^{-1}$  PBS (pH 6.98) containing concentrations of PC and the corresponding calibration plots 104

**Figure 6.11:** DPV measurements for the recovery of PC at ERGO-Au-PGE in (A) with standard additions at different concentrations of sample 106

**Figure 6.12:** Differential pulse voltammograms for electro-oxidation of PC at ERGO-Ag-PGE, at ERGO-Pd-PGE, and ERGO-Pt-PGE in  $0.1 \text{ mol.L}^{-1}$  PBS at pH 7.03 containing  $10 \mu\text{mol.L}^{-1}$  PC solution 108



**LIST OF TABLES**

**Table 5.1:** The summary of results of the effect of interferences on the oxidation peak current of PC at different concentrations, and their RSDs (%) 79

**Table 5.2:** Calibration data from the experiments conducted for analytical performance of PC at ERGO-Sb-PGE 81

**Table 5.3:** Comparable results of calculated detection limits summarized from previous studies for PC at modified electrodes 82

**Table 5.4:** Results of the recovered PC from a commercial tablet containing 500 mg PC at ERGO-Sb-PGE using standard addition and calibration curve methods 84

<b>Table 6.1:</b> The results depicting the effect of interferences on the oxidation peak current of PC at different concentrations with their relative standard deviations (%)	103
<b>Table 6.2:</b> Calibration data from the experiments conducted for analytical performance of PC at ERGO-Au-PGE	105
<b>Table 6.3:</b> Results of the recovered PC from a commercial tablet containing 500 mg PC at ERGO-Sb-PGE using standard addition and calibration curve methods	107



# CHAPTER ONE:

## Introduction

### 1.1. Background

Drugs are compounds that are designed to have biological activity, and therefore it is not surprising that under certain conditions they may prompt toxic reactions. The danger to the individual depends upon several factors, including the nature of the toxic response, the dose necessary to produce the toxic response, and the margin between the therapeutic dose and the toxicity threshold. Thus, the use of a very dangerous drug with only a narrow margin between the therapeutic and toxic dosage may not be justified if a safer drug as medication for that particular disease is available [1].

It has been reported that over the last decades, numerous drugs have been switched from prescription only to over-the-counter (OTC) status in Europe [2, 3]. While this development permits more patient autonomy, contributes to higher appreciation of pharmacists' knowledge and puts less fiscal pressure on European publicly funded healthcare systems [2, 4], concerns about misuse and abuse of OTC drugs have been expressed in the German scientific [2, 5] as well as the popular media [2, 6, 7]. Much concern is raised by public and professional fronts on the irrational use of drugs [8, 9]. The prevalence rates are reported to be high globally; estimated up to 68% in European countries [8, 10], while figures are much higher in the developing countries [8, 11] with rates going as high as 92 % in the adolescents of Kuwait [8, 12].

Several studies have estimated the 1- or 4-week period prevalence of OTC drug consumption among German adults during the last three decades, ranging between 13.1 and 38.5 % [2, 13–15]. More recent studies also investigated specific knowledge and risk awareness of OTC drugs among adults in England [2, 16], Italy [2, 17], The Netherlands [2, 18], and Northern Ireland [2, 19]. It was found that acute paracetamol poisoning is common in Cape Town [20, 21], however very little data is available in South Africa.

Paracetamol (*para*-Acetylamino-phenol) or APAP (*N*-Acetyl-*para*-aminophenol), also called acetaminophen (*N*-(4-Hydroxyphenyl)ethanamide or *N*-(4-Hydroxyphenyl)acetamide), is a synthetic non-opioid analgesic and antipyretic drug. Since it is not ominously anti-inflammatory,

it is not an NSAID (non-steroidal anti-inflammatory drug). However, in general its analgesic and antipyretic capabilities are equivalent to those of NSAIDs [22]. Paracetamol is regarded as the effective and the safe analgesic drug used to relieve mild to moderate associated with headache, backache, arthritis, and postoperative pain. It is also used for the reduction of fevers of bacterial and viral origin [23].

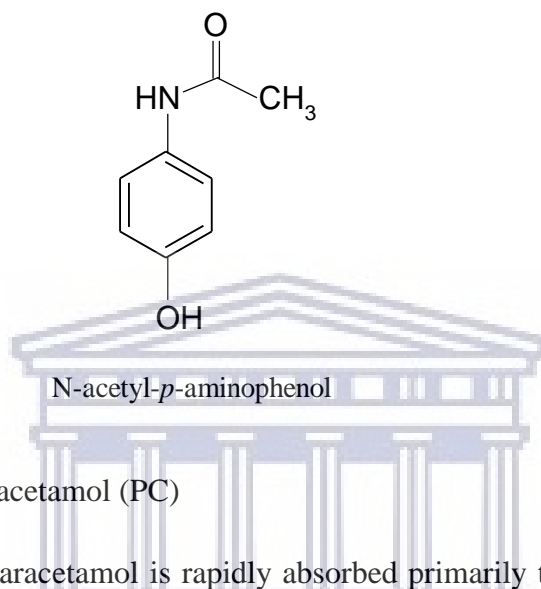


**Figure 1.1:** Structure of paracetamol (PC)

Upon oral administration, paracetamol is rapidly absorbed primarily through the small intestine of the gastrointestinal tract, where it is minimally distributed in the stomach (bioavailability of 85-98%) [22, 24-26]. Metabolism primarily occurs in the liver where it involves conjugated glucuronidation, sulphation, and oxidation through an enzymatic pathway [22]. The main reactive metabolite of oxidation is the *N*-acetyl-*p*-benzoquinone imine (NAPQI). *N*-acetyl-*p*-benzoquinone imine is hepatotoxic but is normally rapidly converted to an inert cysteine and/or mercapturic acid metabolite by conjugation with glutathione [22, 27]. However, build-up of the toxic metabolite may take place if this pathway is saturated or glutathione stores are depleted. As a result, this can prompt liver failure [22]. Quantitative determination of PC is important in the quality assurance of the pharmaceutical industry and vital for the healthcare community [28].

There is an opportunity for development of novel sensors that are simple, highly sensitive, stable, accurate, and detect at the lowest analytical limits. Literature has reported on the many methods that have been used for the determination of PC, which may include capillary electrophoresis (CE) [29, 30], high performance liquid chromatography (HPLC) [29, 31], UV-spectrophotometry [29, 32], HPLC-tandem mass spectrometry [29, 33], and thermogravimetric analysis (TGA) [29,

34]. The determinations of PC using these techniques show high sensitivities, but these methods are generally performed at centralized laboratories, requiring expensive instruments, skilled operators, multi-step sample preparations and complicated analysis procedures, which limit their applications for the on-site determination [29].

Electrochemical methods have been strongly considered for the determination of PC as alternative to aforementioned methods. Most electroanalytical techniques are considered selective, highly sensitive, inexpensive, less time-consuming, and of a wide dynamic range and quick response [35].

## **1.2. Problem Statement**

Paracetamol has been recognized as one of the most commonly used analgesics in the world [33]. The drug is often used as an alternative to aspirin and available as self-medication or without a prescription [8, 36]. The definition of self-medication is described as attaining and consuming drugs without the advice of a physician either for diagnosis, prescription, or surveillance of treatment. This includes acquiring medicines without a prescription, resubmitting old prescriptions to purchase medicines, sharing medicines with relatives or members of social association, or using leftover medicines stored at home [8, 9]. Estimation between 82 000 and 90 000 patients has been reported each year in the UK for PC overdose [37].

Electrochemical methods are more and more widely used for the study of electroactive compounds in pharmaceutical forms and physiological fluids due to their simple, rapid, and economical properties [38, 39]. Paracetamol is a phenolic compound and therefore electroactive, and as such, these present sluggish voltammetric responses at the traditional electrode [23, 40]. It has a core aromatic (benzene) ring substituted in *para* orientation by two groups: a hydroxyl and an acetamide (ethanamide). Multiple portions of the molecule are conjugated, including the benzene ring, the hydroxyl oxygen, the amide nitrogen, and the carbonyl carbon and oxygen. As a result, the benzene ring is highly reactive toward electrophilic aromatic substitution, in which all positions being about equally activated, both oxygens and the nitrogen much less basic, and the hydroxyl acidic [22]. Phenolic compounds can foul solid state electrodes. During phenol oxidation, the tarry deposits of the compound are formed on the electrodes thus resulting in polymerization products. The fouling agents lead to the loss of electrode activity, and therefore

determining phenolic compounds by electrochemical sensors usually presents poor signal stability [23, 41-43].

There have been several materials reported that have been developed in solving such sensor problem, especially those that are carbon-based such as graphite electrodes [44 – 46], glassy carbon electrodes [44, 47 – 49], carbon paste electrodes [44, 50, 51], modified glassy carbon electrodes [44, 52 – 55], modified carbon paste electrodes [44, 56, 57], graphite–polyurethane composite electrodes [44, 58], carbon ionic liquid electrodes [44, 59], carbon fiber microelectrodes [44, 60], and screen-printed electrodes [44, 52]. These previously described electrodes have successfully determined PC; however, there is improvement still required for selectivity and sensitivity while maintaining use of cost-effective and simple electrodes. There have been some procedures reported in attempt to diminish such problems; for example, the use of chemically modified carbon electrodes in voltammetric sensors [22, 61].

Modification of electrodes usually requires difficult procedure and increased analytical time. However, this could be required for sensitive and selective determination of overdose levels of PC in whole blood or urine [62]. Electrochemical sensors that are graphene-based have been reported to have recently exhibited excellent analytical performance for small biomolecules. Graphene greatly promotes electrochemical reactivity of biomolecules on modified surfaces; due to its extraordinary electronic transport properties and high electrocatalytic activity; whilst the unique two-dimensional crystal structure of graphene makes it extremely attractive as a support material for metal and metal oxide catalyst nanoparticles [63]. Strong adhesion of metals onto graphene oxide (GO) is highly important for building suitable contacts when GO or reduced GO (rGO) is used in electronic and electrochemical devices. Moreover, the metal/graphene oxide (M/GO) interface itself sometimes acts as a catalytic site for chemical reactions. Therefore, the synergistic effect of this combination can prove beneficial for developing a functional sensor [64].

### ***1.3. Research Aims and Objectives***

The main purpose of this study is to determine PC at the electrochemically reduced graphene oxide-metal nanocomposite modified pencil graphite electrode (ERGO-MC-PGE) by means of adsorptive stripping voltammetric analysis. The aim is to develop an electrochemically modified

sensor under optimized conditions, which will subsequently be used in analytical detection of PC in pharmaceutical formulations. In order to achieve this goal, the following objectives need to be fulfilled:

- (i) Synthesis of graphene oxide using modified Hummers method.
- (ii) Characterization of graphene oxide using FTIR spectroscopy, Raman spectroscopy, XRD, HRSEM, and HRTEM.
- (iii) Deposition of metal nanoparticles *in situ* onto the graphene oxide and consequently electro-deposit onto the pencil graphite electrode.
- (iv) To characterize the developed ERGO-MC-PGE using cyclic voltammetry (CV) and electrochemical impedance spectroscopy (EIS)
- (v) To detect PC through electro-oxidation at the ERGO-MC-PGE using adsorptive stripping differential pulse voltammetry
- (vi) To optimize instrumental and analytical parameters for the detection of PC at ERGO-MC-PGE
- (vii) To use the analytical response of the electro-oxidation of PC for detection in pharmaceutical formulations.

#### **1.4. Hypothesis**

Paracetamol can be detected at an electrochemical sensor such as ERGO-MC-PGE using adsorptive differential pulse voltammetry. Under optimal conditions, the ERGO-MC-PGE can be highly sensitive and selective for the analysis due to its modification. The proposed sensing platform can be able to produce reproducible results at low detection limits for PC.

#### **1.5. Research Questions**

- (i) How does the binding of metal nanoparticles onto the electrochemically graphene oxide influence the synergistic effect of the electrode?
- (ii) What are the instrumental parameters used for the electro-deposition of graphene oxide-metal salts onto the PGE surface?
- (iii) At what potential is PC electro-oxidized at the proposed ERGO-MC-PGE sensor?
- (iv) Is the proposed sensor reproducible under optimal conditions for detection of PC?

## 1.6. Research Approach

In the current study, it was crucial for the proposed sensor to establish optimal conditions by evaluating the effect of each parameter of the voltammetric procedure towards the sensitivity of PC at the electrode surface, one at a time while others were kept constant. It was important to follow a designed experimental procedure for clarity, therefore the steps considered for the investigation of synergistic influence of electrode modification towards PC detection included:

- (i) Oxidation of graphite by specific reagents during GO synthesis.
- (ii) The introduction of metal nanoparticles onto the GO sheets.
- (iii) The technique used for depositing electrochemically reduced graphene oxide-metal nanoparticles on the electrode surface.
- (iv) Instrumental parameters for electro-deposition of electrochemically graphene oxide-metal nanoparticles onto the electrode.

Cyclic voltammetry (CV) was used for the electro-deposition of graphene oxide-metal nanoparticles, which was described as coating on the electrode surface. In this regard, the oxidation and reduction (redox) potential range, the deposition potential, deposition time, the number of sweeps, and sweep rate were considered.

- (v) Structural and morphological characterization of graphite, GO, and ERGO-MC-PGEs.

Graphite and GO were structurally characterized by FT-IR, Raman spectroscopy, and XRD. The developed sensor was morphologically characterized via HRSEM and HRTEM.

- (vi) Adsorptive stripping of PC by DPV.

Adsorptive differential pulse voltammetry was used for the stripping of PC on the modified electrochemically reduced graphene oxide- metal nanocomposite electrode. The effect of pH of the electrolyte used, the oxidation potential range, and sweep rate on the sensitivity of PC were investigated.

- (vii) Optimizations of instrumental parameters.
- (viii) Reproducibility of ERGO-MC-PGEs.

Response of PC oxidation was investigated for reproducibility through optimized parameters for calibration curves and establishing detection limits.

- (ix) Analytical performance of ERGO-MC-PGEs in real samples.

### **1.7. Scope**

The framework of the current study on the development of ERGO-MC-PGE sensors forms part of the research work conducted at Analytical Research and Instrumentation laboratory of SensorLab at the University of the Western Cape (UWC). In previous investigation, the authors developed an electrochemically reduced graphene oxide-pencil graphite electrode *in situ* bismuth-film plated electrode for the determination of trace metals in water [65]. In this study, a similar sensor was developed using similar experimental protocols for the detection of PC in pharmaceutical formulations.

### **1.8. Delimitations**

The research work based on the development of pencil sensors is conducted under primary supervision of Prof. N. Jahed and guidance of Dr. Pokpas. The work is solely performed at the laboratories located at the Department of Chemistry in the university, with no collaboration undertaken in the context thereof. Pencil graphite electrode graphene-based sensors are part of development of novel and cost-effective sensors studies conducted by the SensorLab research group.

## THESIS OUTLINE

This thesis is composed of seven chapter detailed as follows:

### **Chapter One: Introduction**

This chapter is composed of brief introduction of drugs and especially OTCs, which eventually gives insight into PC as an electroactive species. Several previous detection methods for PC are listed, and the focus on the electrochemical technique as a cheap and simple route. Motivation and research approach of the study are included.

### **Chapter Two: Literature Review**

The chapter focuses on literature survey based on the content of the study. The reviewed aspects include background on graphene and its fellow carbon allotropes, characterization methods, graphene-metal nanoparticles, PGEs and other similar electrodes used for other analytes, and the electrochemical stripping methods.

### **Chapter Three: Materials and Methods**

In this chapter, the experimental description is outlined along with the equipment utilized therein. This include the synthesis of GO and the subsequent GO-metal salts used for the modification of PGEs. Characterization methods are also described.

### **Chapter Four: Structural and Morphological Characterizations**

First part of results and discussion section outlines the outcome of structural characterizations and as well as studying the morphology of the synthesized graphite, GO, and ERGO-MC-PGEs. The techniques include FTIR spectroscopy, Raman spectroscopy, XRD, HRTEM, and HRSEM.

### **Chapter Five and Six: Electrochemical Oxidation of Paracetamol at ERGO-MC-PGEs**

These two chapters describe the electrochemical determination of PC at the developed sensors; ERGO-MC-PGE. In Chapter Five, the electro-oxidation is at ERGO-Sb-PGE and in Chapter Six at ERGO-Au-PGE. The electrochemical characterization of the sensors is detailed in each section, as well as application in pharmaceutical tablet containing PC.

## **Chapter Seven: Conclusion and Future Work**

This chapter concludes the investigation of the study based on the outcomes provided. It also marks the recommendations for future work based on the findings of the study.



## CHAPTER TWO:

### Literature Review

#### *2.1. Introduction*

This chapter intends to give background on the extensive research covered in graphene and ultimately graphene oxide science throughout literature. It purposely concentrates on the structure, characterization and properties of graphene which then influence its application in research, specifically modification in the sensing field including the use of PGE, and electrochemical stripping voltammetric analysis.

#### *2.2. Carbon Allotropes*

Carbon is the element in the periodic table that provides the basis for life on Earth. It is also vital for many technological applications, which vary from drugs to synthetic materials. Such role is facilitated by its ability to bind to itself and to nearly all elements in almost limitless variety [66]. The consequential structural diversity of organic compounds and molecules is supplemented by a broad range of chemical and physical properties. The tools of modern synthetic chemistry allow the tailored design of these properties by the controlled combination of structural and functional building blocks in new target systems [66].

Elemental carbon exists in two natural allotropes namely; diamond and graphite. These consist of extended networks of  $sp^3$ - and  $sp^2$ -hybridized carbon atoms, respectively. Both forms show unique physical properties such as hardness, thermal conductivity, lubrication behaviour or electrical conductivity [66]. Conceptually, many other ways to construct carbon allotropes are possible by changing the periodic binding motif in networks consisting of  $sp^3$ -,  $sp^2$ - and  $sp$ -hybridized carbon atoms [67, 68]. As a result of the expected remarkable physical properties of these elusive carbon allotropes, it has been thus possible to conjure concepts for their preparation in macroscopic quantities [66].

Diamond is the most well-known carbon allotrope and the most stable form of pure carbon. The arrangement of the carbon atoms is in a lattice, which is a variation of the face-centered cubic crystal structure. It is characterized by exceptional physical qualities, most of which are

attributed to the strong covalent bonds between its atoms. Each carbon atom in a diamond is covalently bonded to four other carbons in a tetrahedral coordination [69]. The distance between carbon atoms along the bond is  $1.54 \times 10^{-8}$  cm, and it is known as the single-bond length. The tetrahedrons together form a three-dimensional network of six-membered carbon rings in the chair conformation. Subsequently, this allows for a zero bond-angle strain. The incredibly strong character of diamond as a substance is due to a stable network of covalent bonds and hexagonal rings [70].

For a long period of time, diamond and graphite were represented as the only known carbon allotropes, however that changed with the introduction of fullerenes in 1985 by Kroto *et al.* [66, 70]. This was then followed by marked discovery of carbon nanotubes in 1991 by electron microscopist, Sumio Iijima of NEC laboratories in Japan [71]. These were described as molecular carbon fibres characterized by tiny cylinders of graphite, which were closed at each end with caps containing precisely six pentagonal rings [72]. Therefore, three forms of nanoscale carbon that have attracted attention in recent years due to their novel properties are namely fullerenes, carbon nanotubes, and graphene [73].

Fullerenes have a similar structure to graphite; it is particularly composed of stacked of linked hexagonal rings, which may also be pentagonal or sometimes heptagonal rings [69, 74, 75]. This carbon nanostructure is a super stable species, with its shape resembling a soccer ball. Fullerenes have 60 carbon atoms in their structure with 32 faces [76]. The discovery of fullerenes sparked further research into other structures that can be formed from graphite.

Carbon nanotubes (CNTs) are seamless 1-D structure of rolled-up graphene [77] and have exceptional electrical, mechanical, and thermal properties [75], which made them attractive in the research field. Iijima found CNTs in the solid deposit on the negative electrode after electric discharge [71]. It was discovered that the solids were consisted of tiny tubes made up of numerous concentric graphene cylinders, with each cylinder wall consisting of a sheet of carbon atoms arranged in hexagonal rings. The cylindrical structures commonly have closed-off ends with a length ranging from 2 to 10  $\mu\text{m}$  and a diameter of 5 to 40 nm [78].

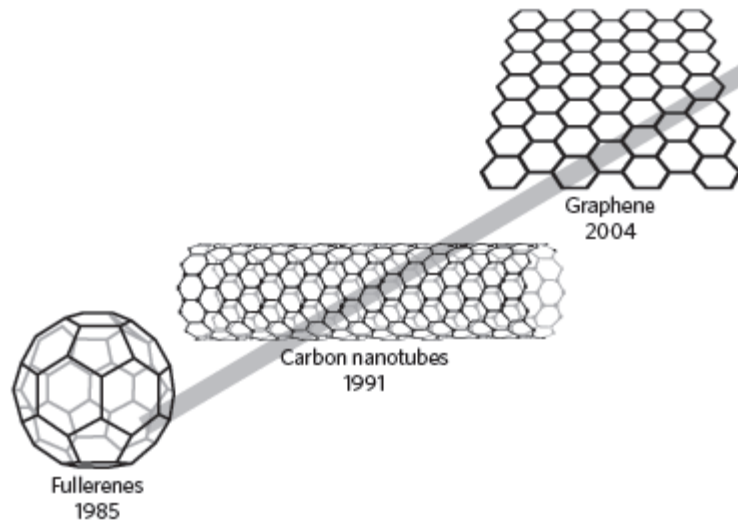


**Figure 2.1:** Forms of carbons allotropes [66].

Graphite is the most common form of naturally occurring polymorphs of crystalline carbon other than diamond. Natural graphite resources are classified based on a multitude of properties, including not only grade but also crystallinity as well as grain (flake) size and shape. Graphite is soft, greasy to the touch, and soils fingers and paper (due to small van der Waals energy between sheets of carbon) [79]. It has many unique physical and chemical properties such as refractoriness, high-heat and electrical conductivity, greasiness, high-thermal resistance, inertness, and readily soluble in iron [79, 80]. Graphite has both metallic and nonmetallic properties [79]. The main graphite derivatives include expanded graphite (EG), graphite oxide, graphene oxide (GO), reduced graphene oxide (RGO), graphene nanoplatelet (GNP) and graphene [81].

### ***2.3. Structural Properties***

Graphene has emerged as the most interesting nanomaterial in the scientific community prospect since its discovery. It is attributed to its fascinating chemical and physical properties that are a driving force towards promising applications. In 2010, Geim and Novoselov received a Nobel Prize in Physics for their work in the isolation of graphene by mechanical exfoliation of graphite in 2004 [82]. Since then, scientific researchers have investigated and exploited the various properties of graphene.

Graphene, a two-dimensional honeycomb sheet of  $sp^2$ -hybridized carbon atoms, exhibits a number of extraordinary characteristics, such as a large theoretical specific surface area ( $2630 \text{ m}^2.\text{g}^{-1}$ ), high intrinsic mobility ( $200,000 \text{ cm}^2.\text{v}^{-1}.\text{s}^{-1}$ ) [83 – 85], high Young's modulus ( $\sim 1.0 \text{ TPa}$ ) [83, 86] and thermal conductivity ( $\sim 5000 \text{ W.m}^{-1}.\text{K}^{-1}$ ) [83, 87], optical transmittance ( $\sim 97.7\%$ ) [83, 88], and good electrical conductivity [83, 89]. These characteristics render graphene popular and useful for applications such as transparent conductive electrodes [83, 90, 91] and supercapacitors, among many other potential applications. The thermal, mechanical, and electrical properties of graphene are derived from long range  $\delta$ -conjugation [83].

Graphene has a remarkable band structure which is attributed to its crystal structure. Carbon atoms form a hexagonal lattice on a two-dimensional plane. Each carbon atom is about  $\alpha = 1.42 \text{ \AA}$  from its three neighbors, with each of which it shares one  $\sigma$  bond. The fourth bond is a  $\pi$ -bond, which is oriented out of the plane in the  $z$ -direction [92]. One can visualize the  $\pi$  orbital as a pair of symmetric lobes oriented along the  $z$ -axis and centered on the nucleus. Each atom has one of these  $\pi$ -bonds, which are then hybridized together to form what are referred to as the  $\pi$ -band and  $\pi^*$ -bands. These bands are responsible for most of the peculiar electronic properties of graphene. The hexagonal lattice of graphene can be regarded as two interleaving triangular lattices [92]. This perspective was successfully used as far back as 1947 when Wallace calculated the band structure for a single graphite layer using a tight-binding approximation [92, 93].

#### **2.4. Surface Properties**

The estimated theoretical surface area of single-layer graphene (SG) is  $\sim 2,600 \text{ m}^2.\text{g}^{-1}$ . The measured Brunauer-Emmett Teller (BET) [94] of few-layer graphene was found to be 270 to  $1550 \text{ m}^2.\text{g}^{-1}$ . Hydrogen can be stored in high-surface-area graphenes. High-surface-area graphene structures can be expected to possess high adsorption properties. They can be used for energy storage devices [95].

The measured surface areas of single-layer and multilayer graphenes were found to be similar to each other. Dervishi *et al.* [96] reported on the Langmuir and BET surface areas for four different samples. The samples were prepared using acetylene or methane with different catalyst systems [95, 96]. Surface area of samples prepared using acetylene was found to be higher than

those of samples prepared using methane. This may be due to the lower molecular diameter of acetylene compared with that of methane [95].

### ***2.5. Magnetic Properties***

With the high electron mobility, SG can be expected to possess excellent magnetic properties. A current-carrying conductor has a magnetic field associated with it. Edge states, such as “armchair” and “zig-zag” configurations of graphene sheets, and adsorbed or intercalated species in the graphene materials can have a salient effect on the magnetic properties [95].

The source of magnetism is not clear in graphene materials. Defects and edge effects can be critical factors. Molecular charge transfer was studied using adsorption studies and the magnetization values were found to decrease with adsorption. Evidence that magnetism found in graphene is intrinsic can be found in the concentration-dependent effects [95]. Dominant ferromagnetic and antiferromagnetic interactions can be seen to coexist as in phase-separated systems by examination of magnetic properties of graphene [95].

### ***2.6. Quantum Properties***

Graphene can be used to examine quantum phenomena in two dimensions. Consider a current flowing in the plane of a two-dimensional graphene sheet. A magnetic field is applied in the normal direction to the current flowing in the sheet. This induces a transverse voltage that is found to increase in discrete quantum steps. This is called the quantum Hall effect (QHE). This can be seen in metals at low temperatures. This phenomenon occurs in graphenes at ambient temperatures. Two different types of QHEs have been found in bilayer graphene and SG [95].

Some aspects of quantum electrodynamics (QED) can be tested using graphene sheets. Otherwise, these experiments would need high-energy particle accelerators. Waves of electric charges across the hexagonal lattice of graphene can be considered as quasi-particles. They are analogous to photons-massless and have quantum character of electrons [95].

## 2.7. Optical Properties

It is widely established that graphene has numerous fascinating properties [89, 98 – 102]. Though considered as a semimetal, graphene has unique electromagnetic/plasmonic effects compared to conventional noble metals [97, 103, 104]. First, its plasma frequency is described in terms of long-wavelength limit [97, 105 – 108]. The difference in the plasma frequencies between graphene and metals is due to the Dirac fermions in graphene, rather than to ordinary Schrodinger fermions in normal metals [97].

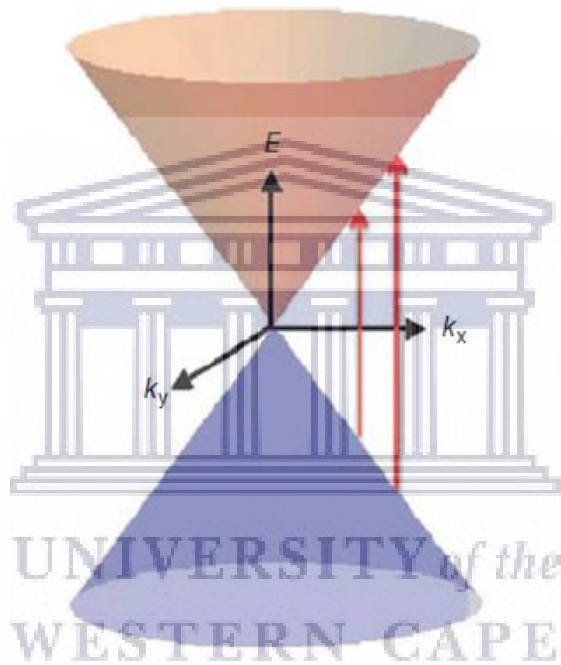


**Figure 2.2:** Schematic of Dirac-cone and interband optical transitions in graphene [97].

Second, single-layer graphene has a linear dispersion relation and a uniform 2.293 % light absorption across a wide frequency range [97, 104, 109 – 111], resulting from its Dirac-cone band structure and linear energy-momentum relation. Many works have studied the surface plasmonic properties of graphene or graphene ribbons, with different experimental techniques, including optical measurements, electron energy loss spectroscopy, angle-resolved photoemission spectroscopy, and surface tunneling spectroscopy [97, 112 – 116].

## ***2.8. Electrical Properties and Tunability***

Graphene transport and optical properties sensitive and tunability by doping is one of its greatest advantages in its studies. The Fermi level can easily be shifted by introduction of either electrons (n-doping) or holes (p-doping). Several ways of establishing a desired doping level have been investigated, for instance, by chemical doping [97, 117, 118], electrochemical doping [97, 119 – 123], electrostatically by top or back gating [97, 124 – 126], and by the direct introduction of heteroatoms into the lattice [97, 127].

One of the most studied and widely used techniques is to introduce the charge by top or back gating [97, 124 – 126]. This technique is appealing due to its similarity to present use in gating field-effect transistors, which allows the knowledge and expertise learned from standard microelectronics to be used more widely in graphene electronics. However, one drawback of this approach is the extremely high gating potential ( $\sim 100\text{V}$ ) that is required, because the present gate dielectrics have a relatively large thickness that restricts the gate capacitance value. For example, bias voltages as high as  $80\text{V}$  had to be used to achieve a carrier density of  $\sim 5 \times 10^{12} \text{ cm}^{-2}$  [97, 126], and such a high bias voltage could cause charge trapping from the substrate, thereby altering the properties of both the substrate and the graphene [97].

## ***2.9. Synthetic Routes of Graphene***

Several synthetic routes have been established to prepare graphene, but each one of them, besides possessing different scalability, generates graphene with very different characteristics, which strongly influence its properties. The preparation methods of graphene can be classified into two distinct approaches: top-down and bottom-up [128].

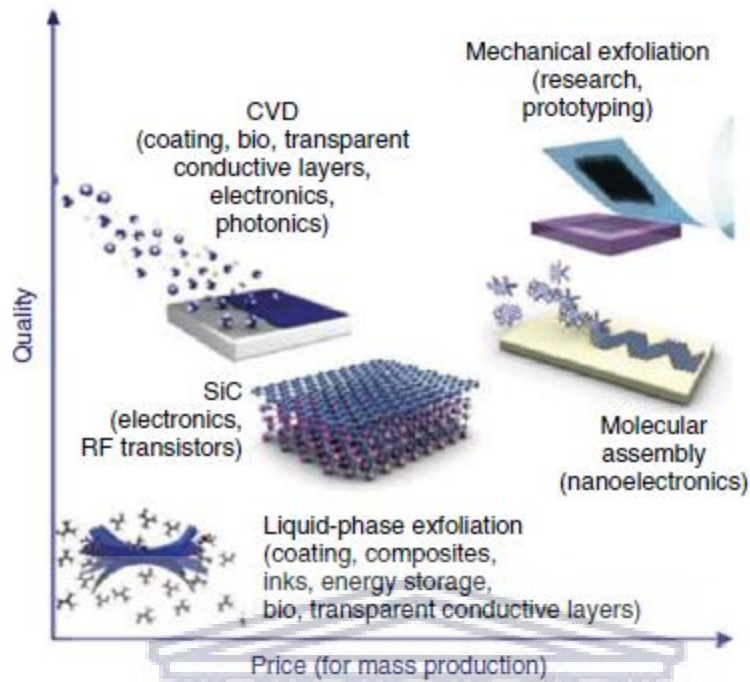


**Figure 2.3:** Overview for the production methods of graphene [97, 129].

### 2.9.1. Top-Down Methods

The top-down methods generally include the exfoliation of graphite as starting material through mechanical (e.g., Scotch tape), chemical (e.g., solution-based exfoliation, graphite oxide exfoliation/reduction), or electrochemical (oxidation/reduction and exfoliation) processes, which aim at weakening the van der Waals forces between the graphene layers [128].

#### 2.9.1.1. Mechanical Exfoliation of Graphite

Micromechanical cleavage of highly oriented pyrolytic graphite (HOPG) is the first proposed method to isolate a single layer graphene. It was described for the first time by Geim and Novoselov in 2004 [82, 128]. This method involves repeatedly peeling off layers of graphene from HOPG by means of an adhesive tape to eventually give single graphene layers that can be transferred successively onto an appropriate surface (e.g., SiO<sub>2</sub> wafers) through a wet or dry transfer technique. More commonly referred to as the “Scotch-tape method”, such micromechanical cleavage has facilitated the initial experimental measurements on the extraordinary electronic [82, 128, 130 – 132], mechanical [86], and thermal conductivity [128,

133] properties of graphene, which subsequently triggered a burst of interest for graphene in several branches of science [89].

The Scotch-tape method is extremely simple, enables the isolation of single layer graphene with a dimension up to 1 mm [128, 134] in size and causes minimal or no alteration to the graphene sheet in the process. In fact, graphene obtained by this method is considered pristine and is of the highest quality achievable thus far. However, it can only be adopted for fundamental studies and basic research due to the low reproducibility and the impossibility of large-scale implementation [128].

Pristine graphene isolated by such micromechanical exfoliation of graphite is expected to possess poor electrochemical activity, most likely comparable to the basal plane of graphite [128, 135]. Although recent studies showed an improved electron transfer kinetic for pristine graphene with certain redox probes compared to the basal plane of graphite. Such improvement was possibly attributed to the presence of corrugations on the graphene sheets [128, 136, 137].

#### ***2.9.1.2. Solution-Based Exfoliation of Graphite***

There have been efforts made to develop a chemical method that is able to facilitate the separation of the graphene sheets with minimal alteration, while considering the high quality of graphene that can be obtained by the mechanical exfoliation of HOPG [128]. Excellent solution-based exfoliation of HOPG can be achieved when the energy loss during exfoliation is minimized, specifically in organic solvents with surface tensions of  $\sim 40 \text{ mJ}\cdot\text{m}^{-2}$  [128, 138].

Moreover, good organic solvents have a Hildebrand solubility parameter close to  $23 \text{ MPa}^{1/2}$  and non-zero values for the polar and H-bonding parameters of Hansen solubility parameters [128, 139]. Concurrent ultrasonication treatment is generally adopted to drive the exfoliation process. Coleman and co-workers obtained good quality graphene sheets at about 1% concentration in N-methylpyrrolidone (NMP) solvent [128, 138]. Similarly, Novoselov and co-workers prepared a graphene suspension by ultrasonically HOPG for 3 hours in N, N-dimethylformamide (DMF) [128, 140].

Solution-based exfoliation of graphite is certainly an appealing approach considering the possibility to produce good-quality graphene and the ease for large-scale adoption. However,

several drawbacks should be taken into consideration. The majority of the exfoliated flakes remain in a multilayer structure, thus giving rise not only to low yields but also to a large variety of flakes consisting of different number of layers that are difficult to further separate [128, 141]. More importantly, prolonged ultrasonication treatments damage the graphene sheets to result in small-sized graphene flakes and nanometric graphitic impurities. The presence of such impurities is capable of altering the density of edge-like planes, thus dramatically affecting the electrochemical properties of the graphene [128, 142].

### ***2.9.1.3. Electrochemical Exfoliation of Graphite***

Electrochemical methods aiming at the intercalations of ions and compounds within graphite are known since the 1980s when sulfuric acid [128, 143],  $\text{Li}^+$  [128, 144],  $\text{F}^-$  [128, 145, 146] and  $\text{Ni}^{2+}$  [128, 147] intercalated graphite were prepared in both aqueous and organic solvents. After the development of micromechanical cleavage of HOPG in 2004, electrochemical methods of isolating graphene from exfoliated graphite have regained much interest [128, 148].

The electrochemical exfoliation method involves the application of cathodic (reduction) or anodic (oxidation) potentials or currents in aqueous or organic electrolytes to a graphite-based (i.e., HOPG) working electrode in the presence of auxiliary (usually Pt) and reference (SCE, Ag/AgCl, etc.) electrodes [128]. When a positive potential is applied, the graphite electrode is oxidized and the intercalation of negatively charged ions from the solution into the graphitic layers takes place. This is then followed by the application of a negative potential that facilitates the exfoliation process [128].

The exfoliation of graphite into graphene sheets has been achieved by using sulfuric acid [128, 149] and poly(styrenesulfonate) (PSS) [128, 150] as electrolytes, among others. More recently, SDS surfactant in aqueous solution was used for the graphite intercalation process by applying a positive potential of +2 V to intercalate the SDS molecules into the graphitic layers followed by a negative potential of -1 V to drive the exfoliation process. Graphene flakes with an average size of 500 nm and a thickness of 1 nm (one or two layers) were successfully obtained [128, 151].

Electrochemical exfoliation methods of graphite have several advantages as compared to other methods. These methods are certainly more environmentally friendly, can be performed under

ambient conditions, can be precisely tweaked by controlling the applied potential or current, and are generally fast. However, it is still very difficult to fabricate graphene with a homogeneous size and layer distribution [128].

Furthermore, the use of anodic potentials to intercalate ions causes unwanted oxidation of graphite and the introduction of oxygen functional groups disrupt the  $sp^2$ -hybridized carbon network. This process is highly irreversible, since neither electrochemical nor chemical processes are able to regenerate the  $sp^2$ -hybridized carbon network to the state of pristine graphene [128]. Moreover, the presence of both structural damage and oxygen functional groups has profound influence on the electrochemical properties of the resulting graphene [128].

#### ***2.9.1.4. Chemical Oxidation of Graphite***

While micromechanical exfoliation of graphite relies on the strong interaction between graphene layers and sticky tape to overcome the cohesive interlayer van der Waals forces of graphite, a chemical route based on a similar principle can also be carried out to facilitate the exfoliation process. This involves the intercalation of chemical species within the graphitic layers followed by a subsequent expansion/decomposition process that forces the layers apart [128].

One of the most well-known approaches to expand graphitic layers is through oxidative intercalation by means of strong oxidizing agents in the presence of concentrated sulfuric and nitric acids. Brodie, in 1859, used potassium chlorate as an oxidant in his attempt to determine the exact formula of graphite by generating highly oxidized graphite. The newly oxidized graphite contained several oxygen functional groups disseminated all over the graphitic structure, which therefore introduced  $sp^3$ -hybridized carbon atoms within the  $sp^2$ -hybridized carbon network of graphite [128, 152].

This method was then perfected and improved, in the following chronological order, by Staudenmaier (1898) [128, 153], Hofmann and König (1937) [128, 154], Hummers and Offeman (1958) [128, 155], and lately Tour and co-workers (2010) [97], to obtain what is now called graphite oxide [128, 156]. The methods introduced by Staudenmaier, and Hofmann and König applied potassium chlorate as an oxidizing agent, while Hummers and Offeman, and Tour and co-workers applied potassium permanganate instead to avoid the formation of dangerous, explosive  $ClO_2$  gas. The formation of several oxygen functional groups within the graphitic

layers increased the interlayer distance from 3.35 Å in graphite to over 6 Å in graphite oxide (humidity dependent). As a result of that, the cohesion strength between graphene layers is weakened such that even a simple ultrasonication treatment can further separate the layers [128, 157].

Isolated sheets from GO, called graphene oxide, is an attractive material, because it can be obtained in a solution form and offers great opportunities for large-scale production of graphene [128, 158]. In contrast to pristine graphene, graphene oxide demonstrates several interesting and unique properties. Graphene oxide exhibits high electrical resistivity due to the disrupted  $sp^2$ -hybridized carbon network by oxygen functional groups and also exhibits photoluminescence due to band gap opening as a result of quantum confinement effect from small  $sp^2$  domains [128].

The chemical reduction method is an attractive and highly scalable synthetic route that allows for the fabrication of graphene materials with unique characteristics that can be exploited in electrochemical sensors, energy storage devices, transparent conductive films, and composites [128]. As a matter of fact, the surface compositions and structural properties of the graphene materials obtained from this fabrication method can be very different. Starting from GO, which is non-conductive, highly defective, and rich in oxygen functional groups (C/O ratio  $\sim 2$ ), a wide variety of chemically reduced graphene materials with different electrical properties, surface compositions, and density of defects can be obtained by varying the types of reducing agents, the starting GO material, and the synthetic conditions [128].

### **2.9.2. Bottom-up Methods**

On the other hand, the bottom-up methods generate graphene by assembling small molecular building blocks into single or few layer graphene structures by means of catalytic (e.g., CVD), thermal (e.g. SiC decomposition), or chemical (organic synthesis) processes [128].

#### **2.9.2.1. Chemical Synthesis**

The synthesis of small “graphene molecules” represents a very interesting route because it allows for the preparation of graphene with well-defined shape and controlled edge structures. Considering graphene as a polycyclic aromatic hydrocarbon (PAH) of infinite size, it only makes

sense to combine small PAH molecules to create graphene [128]. The main drawback of this method is that graphene molecules that are larger than a few nanometers become highly insoluble in most organic solvents, which impedes further synthetic growth and facilitates uncontrolled side reactions instead [128].

The pioneers and main actuators of this synthetic route are Müllen and co-workers, who demonstrated the synthesis of graphene nanoribbons of 30 nm in length [128, 159] and the largest graphene molecule consisting of 222 carbons with a size of 3.2 nm [128, 160], among others which are well-described in another recent review [128, 161]. Although the chemical synthesis method has to deal with several challenges, with the size limitation of graphene being the main obstacle, it represents a promising route for a clean and scalable fabrication method of graphene [128].

### ***2.9.2.2. Epitaxial Growth on SiC***

Graphene growth has been achieved on SiC substrates by heat treatment at high temperatures under ultrahigh vacuum (UHV) conditions [128, 162]. During the process, Si atoms sublime to leave an exposed layer of carbon atoms that will rearrange to form graphitic layers (epitaxial graphene). Precise control of the sublimation temperatures may lead to the formation of very thin graphitic layers, occasionally of single sheets [128, 163]. A wafer-scale coating of monolayer graphene was recently achieved by annealing at a higher temperature (1650 °C) in Ar atmosphere rather than at a lower temperature (1150 °C) under UHV conditions [128, 164].

The properties of graphene grown on SiC are somehow different than those of mechanically exfoliated graphene. This is mainly due to the presence of substrate-induced corrugations and irregular orientations of the graphene layers, which alter the electronic properties [128, 162, 165]. The use of SiC wafers to grow graphene is very promising due to the fact that it can be easily integrated into current industrial procedures used in the electronics industry.

However, the high cost of single-crystal SiC wafers is the main limiting factor for large-scale fabrication. The electrochemical properties of epitaxial graphene were investigated by Loh and co-workers, who concluded that as-prepared epitaxial graphene possessed poor electrocatalytic properties, specifically, slow electron transfer rates. The application of an anodizing potential

increased the density of defects and introduced oxygen functionalities on the epitaxial graphene that substantially enhanced its electrochemical performance [128, 166].

### ***2.9.2.3. Chemical Vapour Deposition***

Large area, single or few layer, high-quality graphene has been produced recently by using chemical vapour deposition (CVD), which makes this one of the most promising techniques for industrial-scale fabrication of graphene [128, 129]. Although CVD graphene has poorer electronic and structural properties than mechanically exfoliated graphene, it still demonstrates excellent performances in applications such as electronic transistors [128, 167], transparent conductive electrodes [128, 91], electrochemical devices [128, 168], and corrosion-inhibiting coatings [127, 169 – 171]. Chemical vapour deposition (CVD) is a well-known procedure that has been previously used to fabricate carbon nanotubes.

The procedure involves a high-temperature decomposition step of a carbon source (feedstock) in the presence of a transition-metal catalyst on which carbon atoms will deposit and rearrange into  $sp^2$ -hybridized carbon structures. One-dimensional CNTs are grown over metal nanoparticle catalysts [128, 172], while two-dimensional graphene is grown over metal surfaces such as ruthenium [128, 173], platinum [128, 174], iridium [128, 175], nickel [128, 176], or copper [128, 181]. Lately, nickel and copper metal substrates are very popular due to their high availability and low cost as compared to other types of metal substrates [128, 176 – 181].

In the event that CVD graphene is adopted as an electrode material without any transfer process, it is of crucial importance to consider the efficiency of the CVD process to form a continuous and homogeneous graphene film on the metal catalyst substrate. Any fractures or holes, even at the sub-micrometer level on the graphene film, can leave the metal catalyst exposed and available to interact with external agents. As such, the overall electrochemical properties of the CVD graphene layer may be wrongly evaluated, since the exposed metal catalyst substrates are redox active [128, 182, 183]. In addition, CVD graphene can contain small graphitic islands that can dominate its electrochemistry toward simple inorganic or biologically active molecules [128, 184, 185].

## 2.10. Characterizations

### 2.10.1. Fourier Transform Infrared (FTIR) Spectroscopy

Fourier Transform infrared spectroscopic analysis is known to provide information to confirm the presence of oxygen-containing functional groups in the structure of synthesized and exfoliated GO. Literature reports on the many characteristic structural features of GO observed in its FT-IR spectrum [186 – 191]. In the reported spectra, there is a strong and broad O-H stretching vibration at the following peaks;  $3410\text{ cm}^{-1}$  [186],  $\sim 3430\text{ cm}^{-1}$  [187], and in the region  $\sim 3700$  to  $3000\text{ cm}^{-1}$  [188]. These are attributed to phenolic OH or OH of carboxylic groups [189]. There are peaks exhibited around  $2925$  and  $2845\text{ cm}^{-1}$  which are due to  $\text{sp}^2$  and  $\text{sp}^3$  C-H stretching bands reported to have resulted from defects sites of the graphene network [187]. The presence of peaks at  $1721\text{ cm}^{-1}$  [186] or  $1730\text{ cm}^{-1}$  [187] are reported due to C=O stretching of the carboxylic groups, while at  $1620\text{ cm}^{-1}$  the peak is attributed to the aromatic C-C stretching [187]. At  $1400$  or  $1404\text{ cm}^{-1}$  there is a peak corresponding to the O-H deformation [186, 190]. There is also a reported C-OH stretching at  $1260\text{ cm}^{-1}$  [191] and at  $1087\text{ cm}^{-1}$  due to C-O stretching vibration [186, 188]. An example of FT-IR spectra of GO prepared from (a) commercial and (b) ball-milled graphite in Figure 2.4 [188].

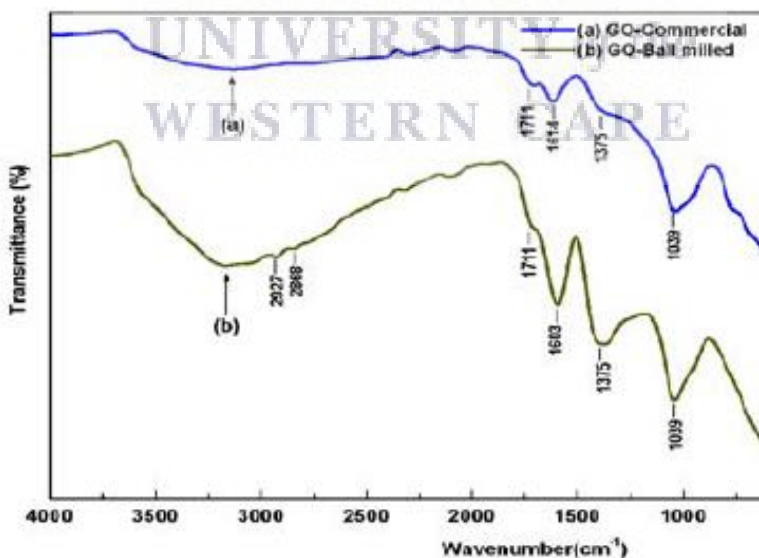


**Figure 2.4:** FT-IR spectra of GO prepared from (a) commercial and (b) ball-milled graphite [188].

### 2.10.2. Raman Spectroscopy

In Raman spectroscopy, the inelastic scattering of light from a laser is used to study vibrational and rotational modes in a material. In this way, important physical and chemical phenomenon in graphene is studied in a fast and non-destructive way [192]. The commonly studied features in the Raman spectra of graphene are the G, D, and G' bands (the G' band is also called the 2D band), shown in Figure 2.5. The shapes of the electronic bands can be probed by varying the laser excitation energy, which shifts the peak position of the D and G' bands and thus provides additional important information [97].

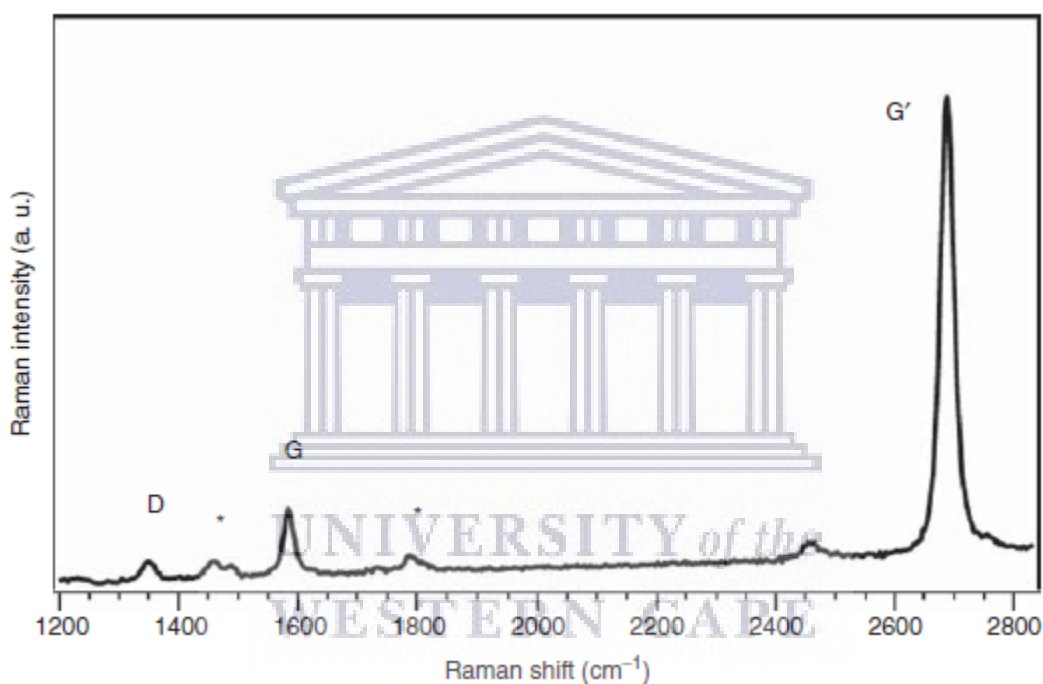


**Figure 2.5:** Raman spectrum of graphene at 0 V (applied bias voltage), excited by a 2.33 eV laser radiation, in an electrochemical environment. The asterisks (\*) indicate Raman bands of the electrolyte [97].

The G band in Figure 2.5 is observed to be due to the optical phonon of graphene, which occurs at a high frequency of  $\sim 1580\text{cm}^{-1}$ , because the carbon atoms are very light, having atomic number 6. From a many-body point of view, the origin of the G band can be explained as that of an electron that is excited from the valence band into a conduction band by absorbing a phonon. An electron-hole pair is thus created. When the electron and the hole then recombine, a phonon is emitted, which has a slightly shifted frequency and a lifetime connected to its bandwidth [97].

The energy of the phonon and the charge carriers will thus be renormalized by the various interactions. Since the band structure of graphene is conical with a linear  $E(k)$  relation, and thereby symmetric for electrons and holes with respect to the Dirac point, the frequency shift of the G band upon doping can be expected to be equal for positive and negative doping. However, the C-C bond strength is also changed somewhat when the graphene is doped [97, 126].

The G' or 2D band in Figure 2.5 is also sensitive to doping, although to a lesser extent than the G band. Doping induces changes in the frequency of the G' band due to changes in the C-C bond strength, the electron-phonon coupling, and electron-electron interactions. The frequency of the G' band increases for positive doping, whereas it first increases for negative doping followed by a relatively large decrease at higher negative potentials. It has been found both experimentally [97, 123] and theoretically [97, 194] that the G band frequency shifts by  $\sim 0.5$  times as much as the G' band per volt in the range from 0 to 1V. Strain can also influence the frequency of the G and G' band. The two effects can be disentangled from one another by correlating the peak positions in the Raman spectra [97, 123, 195].

### **2.10.3. X-Ray Diffraction (XRD)**

X-ray diffraction has been used to study nanostructured materials such as graphene, where carbon atoms are linked to form nanoplatelets present in the material [196]. A typical XRD of graphite possess two characteristic peaks at  $2\theta = 26^\circ$  where the d-spacing is 0.34 nm ( $d = 3.36 \text{ \AA}$ ) attributed to (001) in the crystal plane, and one at  $2\theta = 55^\circ$  ( $d = 0.17 \text{ nm} \sim 1.7 \text{ \AA}$ ) corresponding to (004) in the crystal plane [196]. Following oxidation to form GO, the peaks shift to smaller angles in the crystal plane (002) where  $2\theta = 10^\circ$  with  $d = 0.83 \text{ nm} \sim 8.33 \text{ \AA}$  [83],  $2\theta = 11.4^\circ$ ;  $0.77 \text{ nm} \sim 7.7 \text{ \AA}$  [188], and  $2\theta = 12.8^\circ$ ;  $d = 0.69 \text{ nm} \sim 6.9 \text{ \AA}$  [196]. The difference in the d-spacing or interlayer spacing is due to the introduction of oxygen-containing functional groups on the edge of each layer causing the increase from graphite to GO [197, 198]. Figure 2.6 shows XRD of graphite (A) and GO (B), with graphene also shown [83, 188].

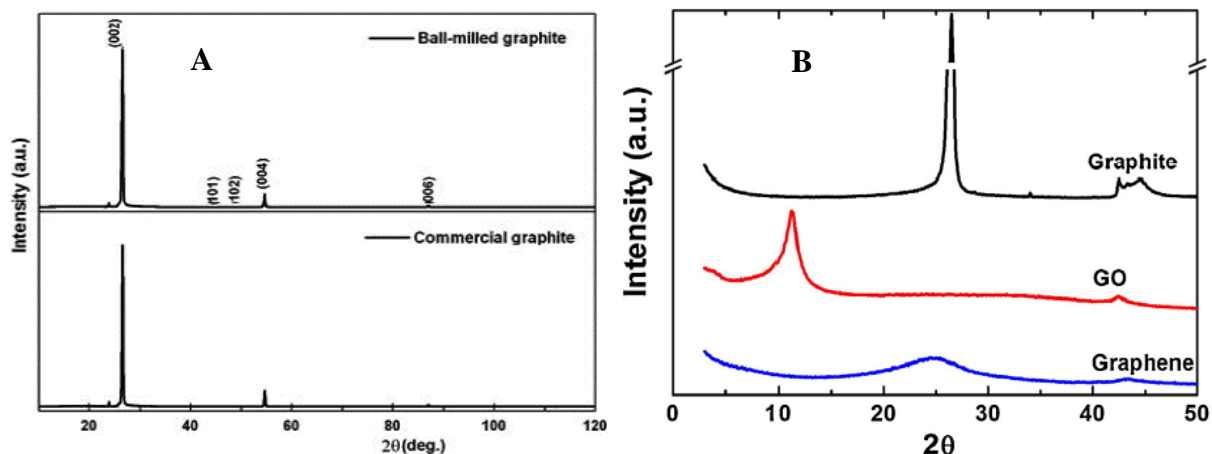


**Figure 2.6:** XRD of ball-milled and commercial graphite in (A), and graphite with GO and graphene in (B) [83, 188].

#### 2.10.4. Scanning Electron Microscope (SEM) and Transmission Electron Microscope (TEM)

Scanning electron microscope (SEM) or field emission scanning electron microscope (FESEM) is used to study the topography, morphology, composition, and crystallographic information of materials. These investigate the materials with sizes and shapes of crystallites that constitute graphene sheets [199, 200]. Samples are scanned using electron beam in a SEM or FESEM. Charge accumulation in a sample occurs with electron beam moved across the surface of it, thereby affecting the imaging if the sample is not conducting.

Transmission electron microscope (TEM) can also accurately identify the thickness of graphene sheets. In this technique, a beam of electrons is transmitted through the sample and an image is formed onto a phosphor screen so that the image can be observed that differs from SEM [199]. Reports on the appearance of stable and transparent sheets were made by Hernandez et al. [138], which indicated the presence of SG. High resolution transmission electron microscope (HRTEM) provides a precise approach to measure the number of layers at multiple locations on a film [176].

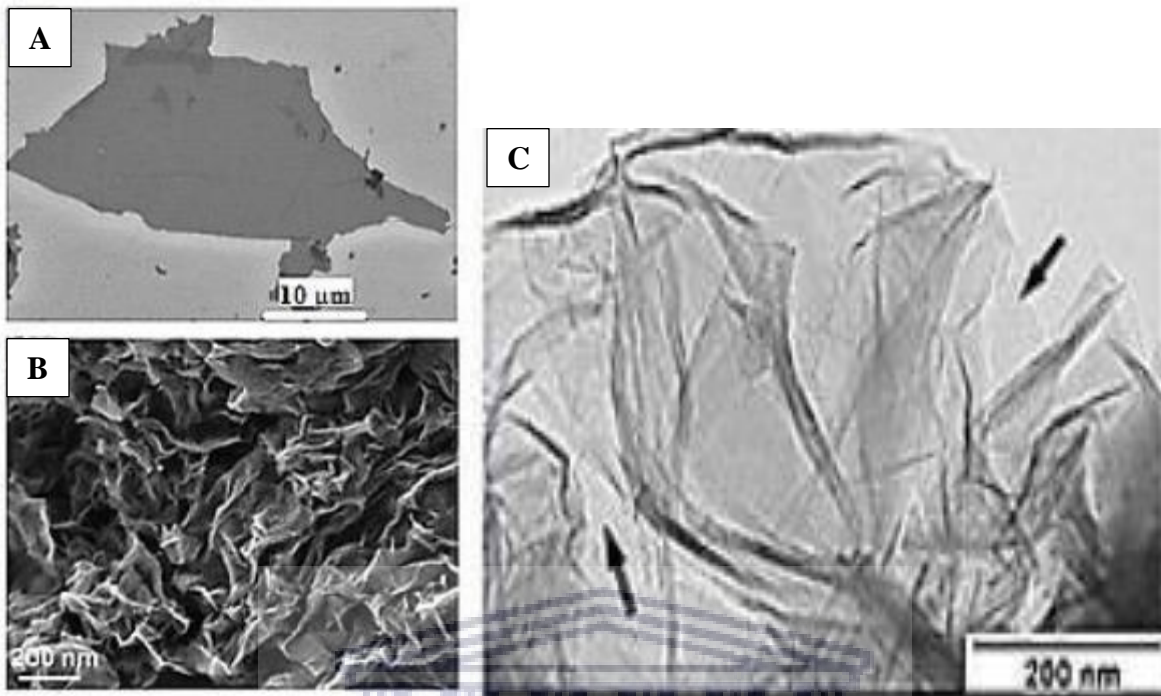


**Figure 2.7:** SEM images of monolayer graphene (A) and aggregated reduced GO sheets (B), and TEM images of graphene nanosheets; monolayer graphene regions indicated by arrows (C) [199].

### 2.11. Graphene Oxide-Metal Nanoparticles

Nanocomposites are described as hybrid materials made up of individual properties of the component materials, which results in synergistic and novel properties. Graphene oxide is known to be a good substrate for metal or semiconductor NPs to be dispersed in. This is attributed to the functional groups such as hydroxyl, carbonyl, and epoxy moieties [201].

It is important to understand chemical and physical properties of metal-graphene oxide (M-GO) interfaces when GO is utilized in electronic and electrochemical devices. This is said to be essential for the metal layer to be firmly attached to GO. Strong adhesion of metals onto GO is very vital for building suitable contacts when GO or RGO is used in electronic and electrochemical devices [202, 203, 204].

Furthermore, the M-GO interface itself sometimes acts as a catalytic site for chemical reactions [202, 205]. The content of oxygenated functional groups at this interface is expected to be strongly affected by the attachment of metals [202, 206 – 208]. Hence, understanding M-GO

interfaces at atomic and/or electronic scale may bring about the development of new electronic/spintronic, photochemical, and electrochemical devices because their properties are affected by defects and the content of oxygenated functional groups [202, 209 – 214].

The electronic and magnetic properties of transition metals deposited on graphene have been theoretically studied on the basis of *ab initio* density functional theory [202, 215 – 220]. Gold (Au) is well-known as a suitable contact material in electronic devices. It has been widely studied at Au-graphene or Au-graphite interfaces toward the development of new electronic devices. It has been reported that Au atoms attached to graphene nanoribbons move along the edges together with Au-C bonds at high temperature [202, 218]. On the other hand, metal sputtering onto graphene and GO surfaces damages and/or removes the top layer and at the same time changes the GO composition (through reduction) [202, 205].

The compositional changes are dependent on the metal type [202, 205], which suggest that some reactions occur between the metal and the GO surface. Ogata *et al.* [202] conducted a study on the permeation of metal from the surface into GO paper bulk at the M-GO interface observed at room temperature for metals such as Cu, Ag, Ni, Au, and Pt. Copper (Cu), Ag, and Ni quickly permeated GO as ions into the bulk under humid conditions. At first, these metals changed to hydrated ions as a result of redox reactions (with reduction of GO) at the surface, and then permeated the interlayers. Gold (Au) and Pt were observed to permeate GO as atoms into the GO bulk at room temperature, although the permeation rates were low [202].

Advantages of graphene used as a substrate for dispersion of NPs include (i) the limited growth of NPs and their improved stability and dispersion on GO or RGO; (ii) the attached NPs are useful for enlarging the interplanar spacing of GO or RGO in the solid state, and for avoiding the aggregation of GO or RGO sheets into graphitic structure [221 – 223]; (iii) a high specific area which could prevent the aggregation of NPs; (iv) excellent properties of individual GO or RGO sheets such as thermal conductivity with excellent thermal stability [132], high mobility of charge carriers, optical transmittance [224, 225], etc. Due to these advantages, graphene-based nanocomposites have been intensively developed and shown a range of unique and excellent applications attracting interest to explore.

## ***2.12. Pencil Graphite Electrodes***

Glassy carbon (GC), pencil graphite (PG) and boron doped diamond (BDD) electrodes are commonly employed carbon-based working electrode. Graphite is the main composition of PG that is found in coal, ore, and other natural minerals. It is considered as the most stable form of carbon. The carbons composed in graphite and GC are all  $sp^2$ -hybridized, hence the high conductivity and easy adsorption of analyte on GCE and PGE [226].

Pencil graphite electrode is a subtype of the graphitic electrodes that has specialized characteristics of the high surface area, good conductivity, and ease to use. However, the uniqueness of PGE is attributed to some of its specific properties such as it being cheap [227, 228], commercially available and easily disposable. Moreover, PGEs are mechanically rigid, easy to modify and miniaturize [227, 229].

PGEs are most attractive electrodes because they offer a simple and faster surface renewal compared to other commonly used electrodes which involve tedious surface polishing procedures [227]. Because of renewable surfaces, PGEs are expected to give reasonably reproducible results. Additionally, PGEs show strong adsorption properties, low background current, and wide potential window [227, 230].

Recently, a very simple method for the determination of phenol was developed. In this method, PGE surface was charged by pretreating in NaOH solution. The charged PGE showed the capability of self-electropolymerization of phenol on its surface, and this led to the sensitive detection of phenol. The self-electropolymerized phenol was detected using square wave voltammetry. Very low limit of detection ( $4.17 \text{ nmol.L}^{-1}$ ) was achieved using this pre-charged sensor [227, 231]. The simplest phenol derivative, 4-nitrophenol, is a major threat to the environment. 4-Nitrophenol is widely used in the fungicides, pesticides, and organic dyes and also in some pharmaceutical products [227].

As a result of excessive use, these products eventually led to 4-nitrophenol being released into the environment. It has good solubility in water [227, 232], and it does not degrade easily into other components, which in turn makes it more persistent in the ground water [227]. Kawde, and Aziz [227, 233] introduced a single step modification of PGE by electrochemical reduction of the Cu (II) on its surface. Copper is more cost effective compared to Au, Ag, and Pt. The

amperometric based electrochemical method was developed for the determination of 4-nitrophenol and the wide linear range was obtained from 50 to 850 mM with LOD of 1.91 mM [227, 233].

The presence of potential interferences like phenol, 4-aminophenol and 3, 4-dichlorophenol showed no effect on the detection of 4-nitrophenol [227, 233]. In another method, the pencil graphite electrode was modified by the bismuth film and was used for the simultaneous analysis of 2-nitrophenol and 4-nitrophenol. Differential pulse voltammetry was used for the electrochemical analysis of 2-nitrophenol and 4-nitrophenol. Bismuth film electrodes are considered as alternate of the mercury film electrode due to environmental friendliness [227, 234].

The PGEs can be easily modified directly with nanostructures, polymers, or a combination of both, similar to precious metal electrodes. Various ways can be used to change the surface characteristics of an electrode [235]. Usually one or more modifiers such as compounds are attached to the electrode surface by coating, casting, or dispersion within a conductive matrix in order to combine the chemical/electrochemical/optical or catalytic properties of the modifier (s) with those of the electrode, thus generating a modified electrode with enhanced figures of importance [235].

### **2.13. Cyclic Voltammetry**

Cyclic voltammetry (CV) is perhaps the most versatile electroanalytical technique for the study of electroactive species. Its versatility combined with ease of measurement has resulted in extensive use of CV in the fields of electrochemistry, inorganic chemistry, organic chemistry, and biochemistry. Cyclic voltammetry is often the first experiment performed in an electrochemical study of a compound, a biological material, or an electrode surface. The effectiveness of CV results from its capability for rapidly observing the redox behaviour over a wide potential range. The resulting voltammogram is analogous to a conventional spectrum in that it conveys information as a function of an energy scan [236].

CV consists of cycling the potential of an electrode, which is immersed in an unstirred solution, and measuring the resulting current. The potential of this working electrode is controlled versus a reference electrode such as a saturated calomel electrode (SCE) or a silver/silver chloride

electrode (Ag/AgCl). The controlling potential which is applied across these two electrodes can be considered an excitation signal [236]. The excitation signal for CV is a linear potential scan with a triangular waveform. This triangular potential excitation signal sweeps the potential of the electrode between two values, sometimes called the switching potentials. A typical cyclic voltammogram is shown in Figure 2.8 for a platinum working electrode in a solution containing 6.0 mM  $\text{K}_3\text{Fe}(\text{CN})_6$  as the electroactive species in 1.0 M  $\text{KNO}_3$  in water as the supporting electrolyte [236].

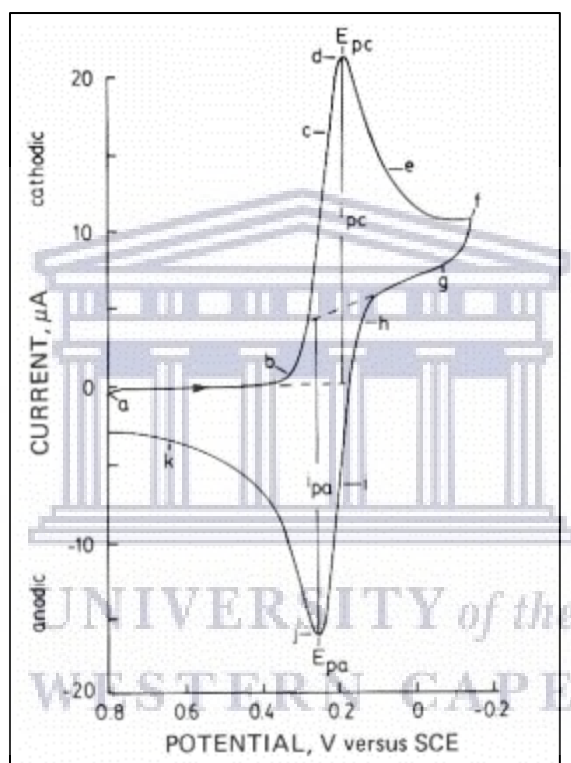


**Figure 2.8:** Cyclic voltammogram of 6 mM  $\text{K}_3\text{Fe}(\text{CN})_6$  in 1 M  $\text{KNO}_3$ . Scan initiated at 0.8 V versus SCE in negative direction at  $50 \text{ mV} \cdot \text{s}^{-1}$ . Platinum electrode, area =  $2.54 \text{ mm}^2$  [236].

#### 2.14. Electrochemical Impedance Spectroscopy

Electrochemical impedance spectroscopy (EIS) has been known to the electrochemistry community for more than a century. Chang and Park [237] describe an electrochemical reaction that takes place at the electrode/electrolyte interface, using an EEC as a model. We then examine whether an EEC can indeed be used as a model for the reaction at the electrified interface. The current flowing at an electrified interface due to an electrochemical reaction,



always contains non-faradaic components, no matter how well the measurement is made. In this equation,  $n$  is the number of electrons transferred,  $O$  is the oxidant, and  $R$  is its reduced product (reductant). The electron is transferred across the electrified interface, as illustrated in Figure 2.9 (a) [237].

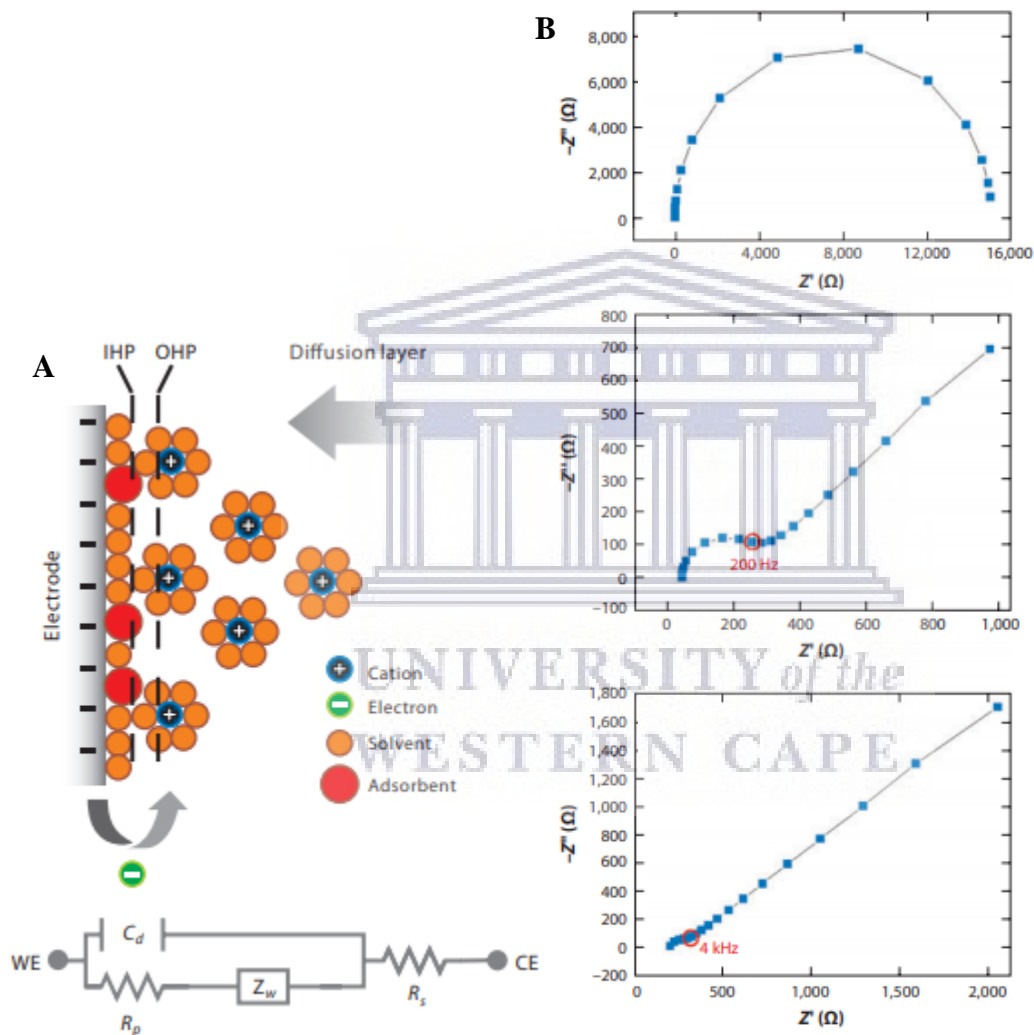


**Figure 2.8:** At top is an electrified interface in which the electrode is negatively charged; counter-cations are aligned along the electrified surface. At bottom are the electrical circuit elements corresponding to each interface component and an idealized Randles electrical equivalent circuit for the interface, shown with no specifically adsorbed anions in (A). Nyquist plots obtained with different kinetic parameters in (B) [237].

The charge transfer leads to both faradaic and non-faradaic components. The faradaic component arises from the electron transfer via a reaction (1) across the interface by overcoming an appropriate activation barrier, namely the polarization resistance ( $R_p$ ), along with the uncompensated solution resistance ( $R_s$ ). The non-faradaic current results from charging the double-layer capacitor ( $C_d$ ). When the charge transfer takes place at the interface, the mass transports of the reactant and product take on roles in determining the rate of electron transfer, which depends on the consumption of the oxidants and the production of the reductant near the electrode surface [237]. The mass transport of the reactants and the products provides another class of impedance ( $Z_w$ ), which can be exploited by electroanalytical chemists because it shows up in the form of a peak current in a voltammogram or a current plateau in a polarogram. The EEC first proposed by Randles (2), displays both the high-frequency components (e.g.,  $R_s$ ) and the low-frequency components (e.g.,  $Z_w$ ). The left-to-right arrangement of the EECs is important because the impedance data are normally displayed in this manner shown in Figure 2.9 (B) [237].

### ***2.15. Electrochemical Voltammetric Stripping Techniques***

Electrochemical stripping techniques are among the most sensitive of instrumental analytical techniques. Due to their high sensitivity and selectivity, these are considerably important in trace analysis and speciation studies. Generally, the detection limits range between  $10^{-11}$  and  $10^{-9}$  mol.L<sup>-1</sup> range, with some cases as low as  $10^{-12}$  mol.L<sup>-1</sup>. These are three or four orders of magnitude more sensitive than the simple polarographic methods [238]. The high sensitivity and selectivity of stripping techniques are attributed to two distinct controlled electrochemical steps involved [238].

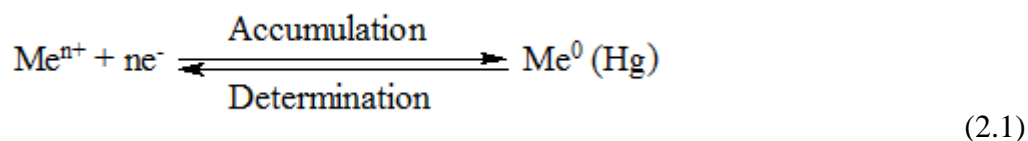
In the first step the analyte, initially existing in the test solution, is transferred to the electrode surface in one of two ways namely: (i) by electrolytic oxidation (anodic) or reduction (cathodic) which results in the analyte forming a deposit on the working electrode. This is considered when the analyte is a metal ion in which case its reduction onto a mercury electrode may produce an amalgam rather than a deposit, or (ii) by the adsorption of the analyte directly or in combination with other reagents onto the electrode surface [238].

This first step is known as a pre-concentration, enrichment, or accumulation step and it proceeds with the working electrode held at a constant potential. Constant area mercury (hanging drop or thin film), carbon, noble metal or modified electrodes may be used. The transfer of the analyte to the electrode surface is usually enhanced by stirring the solution or in some cases by rotating the electrode. In the accumulation process a certain amount of the analyte is transferred from the test solution matrix and forms a phase on or in the electrode in which its concentration is orders of magnitude higher than it is in the test solution [238]. On completion of the accumulation step, a rest period of 15 to 30 s is observed so that the test solution accomplishes a resting period before the second step commences [238].

In the second step, the amount of analyte accumulated at the working electrode is determined by monitoring the electrical response produced as this accumulated material is either oxidized or reduced from the electrode. This is referred to as the stripping step due to the material accumulated during the first step being stripped from the electrode and normally passes back into solution. The stripping is carried out in one of three ways namely: (i) varying the potential on the working electrode and monitoring the current response (voltammetry), (ii) passing a constant current through the cell and measuring the potential that the working electrode develops as a function of time (chronopotentiometry), or (iii) chemically and monitoring the potential of the working electrode during the stripping process (potentiometry) [238].

### **2.15.1. Anodic Stripping Voltammetry**

During the 1960s and 1970s the theoretical principles of stripping voltammetry were established [238, 239, 240] and the method was successfully applied to the analysis of metals at the trace and ultra-trace level [238, 241, 242] and to the environmentally important problem of trace metal speciation in natural waters [238, 243 – 245]. The two processes involved when the analyte is accumulated by electrolytic reduction and determined by voltammetric oxidation are summarized in equation (2.1):



Since the determination step is the inverse of the accumulation processes, the term Inverse Voltammetry was at one time used to describe the stripping technique [238, 246]. After a variation on this technique was developed in which the enriched analyte was determined by a reduction rather than an oxidation step, the above technique became referred to by the more clearly descriptive name anodic stripping voltammetry or its acronym, ASV. In those cases where the analyte accumulated on the electrode is measured by a reduction step, the technique is referred to as cathodic stripping voltammetry or CSV [238].

The steps and resultant current-potential profile for an analysis by ASV are illustrated in Figure 2.10. The left side of the diagram represents the accumulation step while the right side depicts the determination step. During the time interval (A), referred to as the accumulation time,  $t_{acc}$  the analyte is transported to the working electrode surface by convection and diffusion and deposited on the electrode by electrolysis at a constant potential,  $E_{acc}$ . The convective transport is achieved by stirring the solution or rotating the electrode at a constant rate so that a constant diffusion layer thickness is maintained [238]. During accumulation, the electrolysis is not exhaustive and only a small fraction of the analyte is transferred from the test solution to the working electrode [238].

The time interval (B), after stopping the stirring or rotation, must also be carefully controlled. During this time, called the rest period, the working electrode is held at the accumulation potential, the motion of the solution ceases and the cathodic current drops to a small value as the contribution from the forced convection falls to zero. In analyses where a metal amalgam is produced in a mercury drop electrode, the rest period also allows time for the metal concentration to become uniform throughout the drop. At the end of the rest period, a linear or staircase anodic voltage scan is applied to the working electrode from an initial value of  $E_{acc}$  thus initiating the determination or stripping step (C) [238].

The recorded voltammogram exhibits a peak as a result of the oxidation and transfer of the enriched analyte from the working electrode back into the cell solution. Ideally, this transfer should be complete but, particularly with an HMDE, it may be incomplete because the metal dissolved in the amalgam may not have completely diffused from the centre of the drop during the time of the potential scan. This is indicated by 'peak tailing'. The peak is characterized by the peak potential,  $E_p$ , and the peak current,  $i_p$ , which are determined by the nature and concentration

of the analyte, respectively. The rise in the current in the fourth section (D) is due to the anodic dissolution of the mercury working electrode [238].

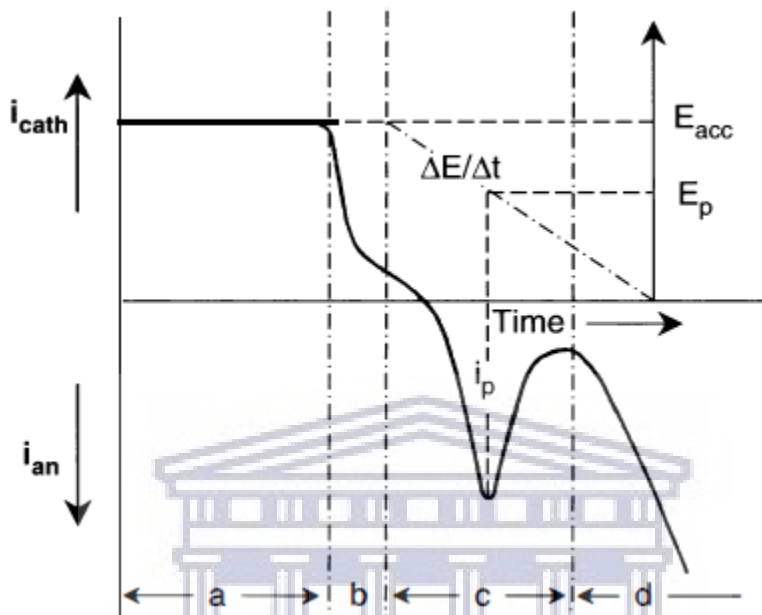
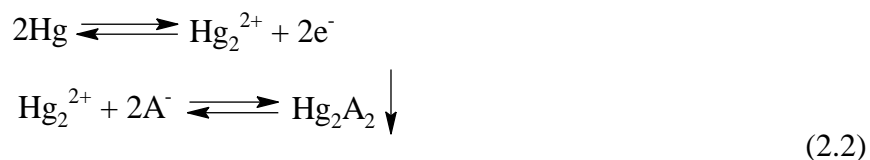


**Figure 2.10:** Potential-current-time relationships during an anodic stripping voltammetric analysis: (A) accumulation time, (B) rest period, (C) determination or stripping step, (D) anodic dissolution of mercury [238].

### 2.15.2. Cathodic Stripping Voltammetry

Cathodic stripping voltammetry (CSV) is used for the indirect determination of inorganic and organic anions which form sparingly soluble salts with Hg (I) or Ag (I). When a mercury (or silver) electrode is anodically polarized,  $\text{Hg}_2^{2+}$  (or  $\text{Ag}^+$ ) are produced and react with the analyte to form the sparingly soluble Hg (I) [or Ag (I)] salt which accumulates on the electrode surface. The accumulation potential depends on the supporting electrolyte, the solubility product of the Hg (I) or Ag (I) salt, and the concentration of the analyte in the test solution. For mercury electrodes  $E_{\text{acc}}$  is usually in the range +0.4 V to -0.2 V (versus Ag/AgCl, 3 mol.L<sup>-1</sup> KCl). In the determination step, a cathodic potential scan is applied to reduce the Hg (I) or Ag (I) in the sparingly soluble salt accumulated on the electrode surface which gives rise to the voltammetric current peak [238].

The technique can be used for the determination of trace levels of halides, pseudo-halides or sulfide (mercury [238, 247] or silver [238, 248] electrodes) and a number of oxometallate ions such as vanadate, chromate, tungstate and molybdate and organic anions (mercury electrodes). The analytical process is summarized in the following equations (for a mercury electrode). Accumulation is described by:



This is followed by determination step which is described by:

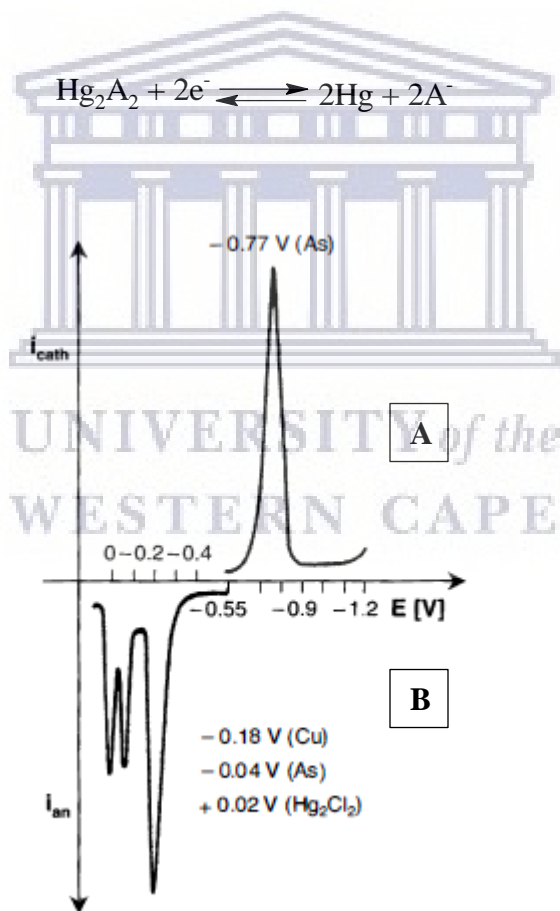


**Figure 2.11:** An example showing the differential pulse cathodic (A) and anodic (B) stripping voltammograms of arsenic. The cell solution was  $0.1 \text{ mol.L}^{-1} \text{ HCl}$  containing  $2 \times 10^{-3} \text{ mol.L}^{-1} \text{ Cu}^{2+}$  and  $10 \mu\text{g.L}^{-1} \text{ As}$ . Voltage scan rate  $100 \text{ mV.s}^{-1}$ ;  $E_{\text{acc}} = -0.55 \text{ V}$ ;  $t_{\text{acc}} = 1 \text{ min}$  [238].

The current peak height due to the electrolytic dissolution of the insoluble layer is proportional to the amount of anion accumulated on the electrode surface, which under constant accumulation and stripping conditions is in turn proportional to the concentration of the analyte in solution. The peak potential is determined mainly by the solubility product of the accumulated salts. The differences in solubilities between the Hg(I) halides and between Hg(I) chromate, molybdate, tungstate and vanadate are not very large so that the stripping peaks occur at similar potentials and the resolution of adjacent peaks is limited [238, 249].

### 2.15.3. Adsorptive Stripping Voltammetry

A wide range of organic molecules and metal chelate complexes are surface active and can be accumulated on the surface of a mercury electrode by adsorption processes rather than by a charge transfer (oxidation or reduction) process. When the adsorbed compounds can be oxidized or reduced, they may be estimated by stripping them from the electrode surface using linear sweep, staircase or differential pulse voltammetry [238]. Adsorptive stripping voltammetry (AdSV) is a powerful method for determining ultra-trace levels of a variety of metal ions (as their chelate complexes), organo-metallic, and organic compounds [238, 280, 251 – 254]. Example of this technique is shown in Figure 2.13.

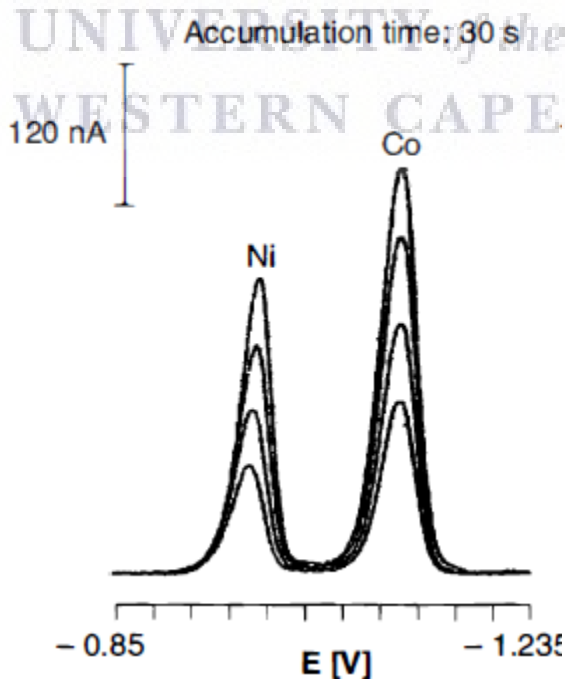


**Figure 2.12:** Adsorptive stripping voltammograms of cobalt and nickel using HMDE. Sample solution:  $20 \mu\text{g.L}^{-1}\text{Ni}$  and  $20 \mu\text{g.L}^{-1}\text{Co}$  in  $0.1 \text{ mol.L}^{-1}\text{NH}_3\text{-NH}_4\text{Cl}$  (pH 9.3) +  $5 \times 10^{-4}\text{mol.L}^{-1}$  dimethylglyoxime. Standard additions: each 200 ng Ni plus 200 ng Co [245].

It has greatly extended the applicability of stripping voltammetry to the analysis of any element or compound that can be adsorbed onto an electrode surface and which can be reduced or oxidized within the potential range available with the particular working electrode-supporting electrolyte and solvent combination used in the analysis. This technique is particularly important in environmental studies for the determination of trace and ultra-trace levels of metal ions that do not form amalgams with mercury or are not readily deposited as the element on a mercury electrode. Adsorptive accumulation has also been used with tensammetric stripping for the determination of some non-electroactive but surface active organic compounds [245].

Adsorptive stripping voltammetry is also a very sensitive method for the determination of ultra-trace levels of a range of organic molecules which contain electroactive functional groups. The determination limits are of the order of  $10^{-10} \text{ mol.L}^{-1}$  and lower. In practice, mercury electrodes are used for the accumulation and determination of organic compounds with reducible functional groups, while those with oxidizable functional groups are accumulated and determined using noble metal or carbon electrodes. Dyestuffs, insecticides, phytopharmaceuticals, pharmaceuticals, biological compounds, vitamins, hormones, nitro-compounds, benzodiazepines, and numerous other compounds may all be determined by AdSV [245].

## CHAPTER THREE:

### Materials and Methods

#### *3.1. Introduction*

The contents of this chapter focus on the experimental materials and methodology used in the development of the ERGO-MC-PGE sensors. Subsequent characterizations are also described with relevant techniques utilized, as well as insight into electrochemical stripping voltammetric analysis of PC at the electrode surface.

#### *3.2. Reagents and Chemicals*

All chemicals that were used for experiments were of analytical grade and solutions were prepared using ultrapure water. Graphite powder (<150  $\mu\text{m}$ , 99.99 % trace metals basis), sulphuric acid (95-97 %, Sigma-Aldrich), potassium permanganate was obtained from PAL Machinery and Chemicals, and hydrogen peroxide (Sigma-Aldrich). Metal stock solutions (1.000 mg.  $\text{L}^{-1}$ , atomic absorption standard solution) were all obtained from Sigma-Aldrich. Acetate buffer solution (ABS; 0.1 mol. $\text{L}^{-1}$ , pH 4.6) was prepared by mixing acetic acid and sodium acetate (Sigma-Aldrich), and phosphate buffer solution (0.1 mol. $\text{L}^{-1}$ , pH 7.02) was prepared from diluting sodium phosphate monobasic and sodium phosphate dibasic solutions (1 mol. $\text{L}^{-1}$ ), with both buffers diluted in ultrapure water. Paracetamol solution was prepared by dissolving the powder in 0.1 mol. $\text{L}^{-1}$  PBS (pH = 7.02) into a final concentration of 10 mmol. $\text{L}^{-1}$  solution. Hydrochloric acid (Sigma-Aldrich) was diluted to make up 1 mol. $\text{L}^{-1}$  and nitric acid (Sigma-Aldrich) to 3 mol. $\text{L}^{-1}$  solutions. Solutions were diluted as required with ultrapure water from the Millipore system.

#### *3.3. Instrumentation*

All voltammetric measurements (cyclic and differential pulse voltammetry) proceeded on a 797 VA Computrace (Metrohm, Switzerland) that was connected to a personal computer. The instrument was composed of a three-electrode electrochemical system which included; Ag/AgCl with 3 mol. $\text{L}^{-1}$  KCl solution as a reference electrode (RE), platinum wire as an auxiliary electrode (AE), and the ERGO-MC-PGEs (MC = Au or Sb nanocomposite) as a working

electrode (WE) as shown in Figure 3.1. All experiments were conducted in a 40 mL electrochemical cell.

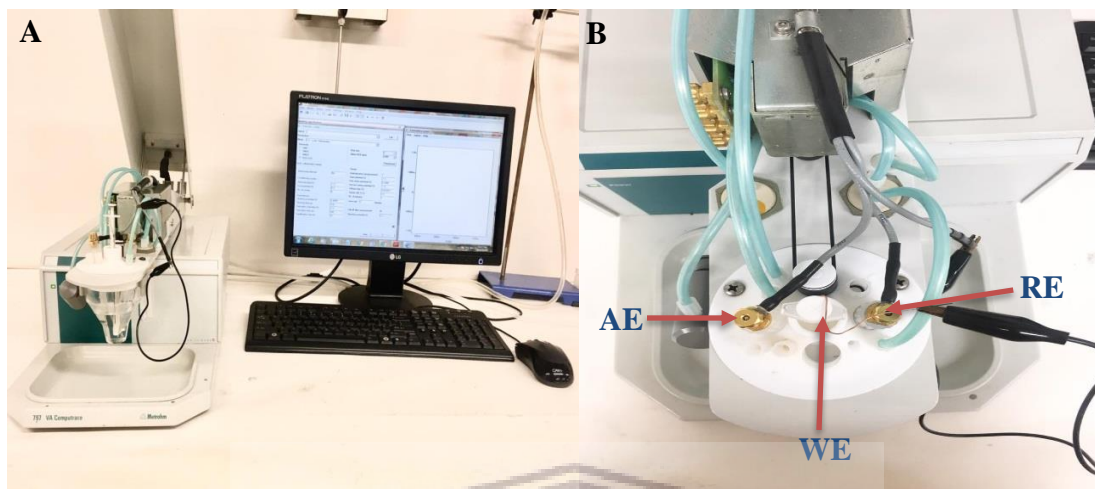


**Figure 3.1:** A 797 VA Computrace voltammetry instrument connected to a personal computer in (A), and the three-electrode system consisting of reference electrode (RE), platinum wire as an auxiliary electrode (AE), and the ERGO-MC-PGE (MC = Au or Sb nanocomposite) as a working electrode (WE) in (B).

### 3.4. Synthesis of GO

Graphene oxide was synthesized from graphite powder according to Hummers method with some modification [155]. The experiment proceeded with 2 g of graphite powder which was added into 50 mL  $\text{H}_2\text{SO}_4$  in a dry conical flask slowly. The reaction mixture was placed in an ice bath and cooled at all times, and then 7 g of  $\text{KMnO}_4$  was added slowly under constant stirring. After complete addition of  $\text{KMnO}_4$  the resultant mixture was left to warm at room temperature. The temperature was then raised by means of a warm water bath to 37 °C and allowed to stir for 2 hours.

The reaction mixture was placed back in an ice bath under constant stirring. Thereafter 100 mL of ultrapure water was added followed by 5 mL of  $\text{H}_2\text{O}_2$  in portions of 1000  $\mu\text{L}$  into the reaction mixture using a micropipette. Once effervescence seized, the reaction mixture was removed from the ice bath and allowed to reach room temperature.

The contents of the conical flask were filtered through vacuum in a Büchner funnel and were washed successively three times with 10 % HCl and ultrapure water. The resulting graphite oxide was collected in a beaker covered with a paper towel, and then undergone vacuum drying for 48 hours. Graphene oxide (GO) solution was prepared by dispersing 500 mg of the graphite oxide in 500 mL 0.1 mol.L<sup>-1</sup> ABS (pH 4.6) that made up 1.0 mg.mL<sup>-1</sup> GO solution. Ultrasonication of the solution was performed for 1.5 hours through which it was subjected to exfoliation to obtain GO solution.

### **3.5. Preparation of GO-Metal Salt Solutions**

The GO-metal salts solution was subsequently prepared from a 50 mL 1.0 mg.mL<sup>-1</sup> GO dispersion by adding 750 µL of metal standard solution (1000 µg.mL<sup>-1</sup>, atomic absorption standard; Sb or Au), into a final concentration of 15 ppm solution. The final solution was placed under ultrasonication for 1 hour.

### **3.6. Electrochemical Treatment and Preparation of Bare PGE, ERGO-PGE, and ERGO-MC-PGEs**

The pencil graphite rods (Pentel, 100HB of 0.5 mm in diameter and 6 cm in length) were purchased from the local book store. A plastic syringe served as a holder into which the pencil rod was inserted exposing 1 cm of the rod tip at one end of the syringe. In order to establish electrical connection with the potentiostat a copper wire was attached to the other end of the pencil rod and passed through the top of the syringe (Figure 3.2).

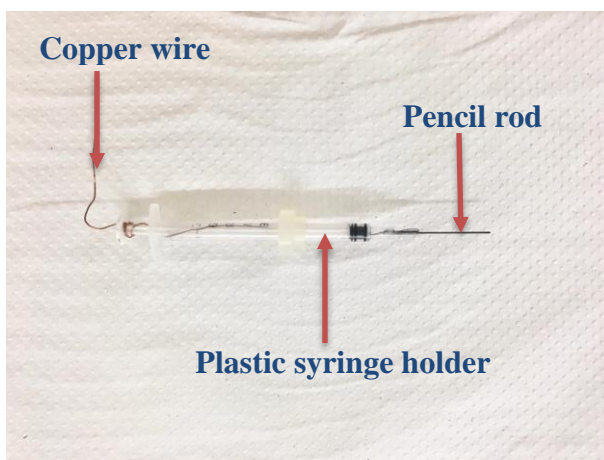


**Figure 3.2:** A plastic syringe holder with a connected copper wire and a pencil rod.

Pencil graphite electrode was cleaned by dipping it in the 3 mol.L<sup>-1</sup> HNO<sub>3</sub> solution and washed with ultrapure water. The PGE was electrochemically treated by immersing the 1 cm surface area in 20 mL 0.1 mol.L<sup>-1</sup> ABS contained in a 40 mL electrochemical cell. Thereafter the electrode was conditioned using cyclic voltammetry (stirrer = 1000 rpm; initial purge time = 30 s; conditioning cycles: start potential = -0.4999 V, end potential = 0.9 V, number of cycles = 0; pretreatment: cleaning potential = 0.3 V, cleaning time = 0 s, deposition potential = -0.6999 V, deposition time = 0 s, equilibration time = 10 s; sweep: start potential = -1.5 V, first vertex potential = 0.3 V, second vertex potential = -1.5 V, voltage step = 0.005035 V, sweep rate = 0.1 V.s<sup>-1</sup> (100 mV.s<sup>-1</sup>), number of cycles = 5). These CV conditions were also used for the reduction of GO and GO-metal salts onto electrode surface, which proceeded by immersing conditioned PGEs in 1.0 mg.L<sup>-1</sup> GO (ERGO-PGE) and 15 ppm GO-metal salt solutions (deposition potential = 120 s, number of cycles = 5 for ERGO-Sb-PGE or deposition potential = 240 s, number of cycles = 1 for ERGO-Au-PGE).

The modified electrodes were left to dry in the refrigerator (temperature at -4 °C) for 30 minutes. These electrodes including the bare PGE were then conditioned in 20 mL 0.1 mol.L<sup>-1</sup> PBS in a single run using the following DPV conditions (stirrer = 1000 rpm; initial purge time = 60 s; conditioning cycles: start potential = 0.3 V, end potential = 0.9 V, number of cycles = 0; pretreatment: cleaning potential = -0.1999 V, cleaning time = 0 s, deposition potential = -0.6998 V, deposition time = 0 s, equilibration time = 10 s; sweep: start potential = 0.0 V, end potential = 0.9998 V, pulse amplitude = 0.05005 V, voltage step = 0.005035 V, voltage step time = 0.4 s, sweep rate = 0.0126 V.s<sup>-1</sup> (12.6 mV.s<sup>-1</sup>).

### **3.7. Batch Preparation of ERGO-MC-PGEs**

An effective and a less time-consuming technique was established for the preparation of modified electrodes. The multi-electrode system shown in Figure 3.3 (A) – (C) consisted of 8 electrodes connected to an 8-hole cap and an electrochemical cell with complementary platinum wire as an auxiliary electrode and an Ag/AgCl (3 mol.L<sup>-1</sup> KCl) reference electrode similarly to Figure 3.1. The electrodes were cleaned and electrochemically treated the same way as for the single coating technique. Stirring was done manually with magnetic mantle switched on and off, and a magnetic stirrer placed in the cell. Cyclic voltammetry and DPV conditions as well as drying were used as previously described in Section 3.6.

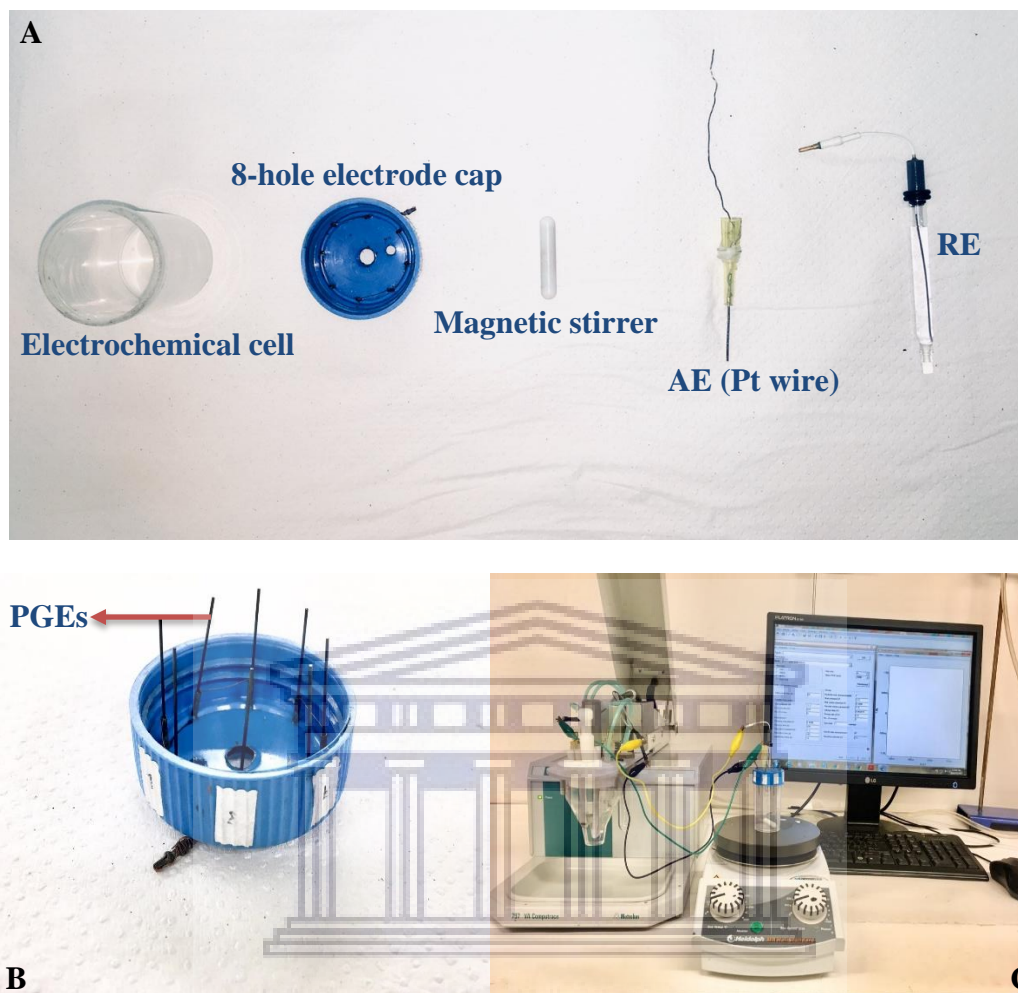


**Figure 3.3:** Batch preparation of ERGO-MC-PGEs; (A) the materials used for the experiment apparatus, an 8-hole cap consisting of 8 PGEs in (B), and the apparatus used for the experiment in (C).

### 3.8. Adsorptive Stripping Differential Pulse Voltammetric Analysis of PC at ERGO-MC-PGEs

All PGEs were cleaned, electrochemically treated, and modified prior to the usage for the PC analysis. The electrodes included bare PGE, electrochemically reduced graphene oxide modified electrode (ERGO-PGE), and electrochemically reduce graphene oxide-metal nanocomposite modified electrodes (ERGO-MC-PGEs; MC = Au or Sb nanocomposite). Electrochemical treatment and conditioning occurred according to CV and DPV parameters as described in section 3.6 of the current chapter.

The prepared electrodes; bare PGE, ERGO-PGE, and ERGO-MC-PGEs (MC = Au or Sb nanocomposite) were therefore immersed in 20 mL 10  $\mu\text{mol.L}^{-1}$  PC sample solution in 0.1 mol.L<sup>-1</sup> PBS contained in 40 mL electrochemical cell. Adsorptive stripping differential pulse voltammetry was used as a method of choice for analysis in which an oxidation potential was applied to the working electrode. Scanning occurred in a potential range from 0.0 to 1.0 V and the scan was reported as a function of current against potential. All electrochemical parameters were varied one at a time while others were kept constant. The purpose of this was to achieve optimum modification for the greatest sensitivity of PC on the electrode surface.

### ***3.9. Characterizations***

#### ***3.9.1. FTIR Spectroscopy***

Structural differentiation of graphene oxide from the oxidation of graphite was studied by FTIR analysis. The spectrum was used to investigate and confirm the presence of oxygen functional groups trapped between the GO sheets. The data was collected from a Nexus 670 FTIR spectrometer. Sample preparation was achieved using KBr wafer method in which 10 mg of graphite or GO were integrated with KBr using pestle and mortar, and the contents were transferred onto a sample holder for analysis.

#### ***3.9.2. Raman Spectroscopy***

The structural composition of graphite and GO were further investigated using Raman spectroscopy. Sample preparation of graphite or GO proceeded by dispersion of both in pure ethanol, and these samples were drop casted onto glass slides for analysis. The information was captured using a Dilor XY Raman spectrometer with a Coherent Innova 300 Argon laser composed of a 514.9 nm laser excitation.

#### ***3.9.3. X-ray Diffraction***

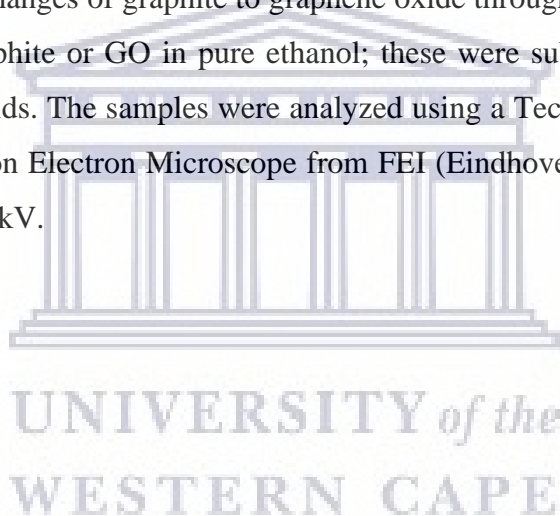
X-ray diffraction technique was additionally used for the confirmation of structural changes in the conversion of graphite to GO. A BRUKER AXS X-ray diffractometer with Cu-K $\alpha$  radiation was used for analysis according to instrumental parameters, with a radiation wavelength of  $\lambda = 1.54051$ .

#### **3.9.4. HRSEM**

The morphological and physical changes of graphene oxide as well as electro-reduction of GO-metal salts onto PGEs were studied through images from HRSEM. Sample preparation proceeded by electro-deposition of GO or GO-metal salts onto the PGE according to CV conditions earlier described. The HRSEM images were obtained using a LEO 1450 SEM 30 kV instrument equipped with Electronic Data System (EDS) and Windows Deployment Services (WDS).

#### **3.9.5. HRTEM**

High resolution transmission electron microscopy (HRTEM) was used to further follow the morphology and physical changes of graphite to graphene oxide through HRTEM. Samples were prepared by dispersing graphite or GO in pure ethanol; these were subjected to ultrasonication and drop casted onto Cu grids. The samples were analyzed using a Tecnai G2 F20X-Twin MAT Field Emission Transmission Electron Microscope from FEI (Eindhoven, Netherlands) under an acceleration voltage of 200 kV.



## CHAPTER FOUR:

### Structural and Morphological Characterizations

#### 4.1. Introduction

The structural and morphological features of graphite and graphene oxide, as well as the electrochemically reduced graphene oxide-metal nanocomposites are detailed. This chapter entails the chemical changes that occurred and further gives insight into the characterization techniques used along with variation patterns observed in each for the analyzed samples.

#### 4.2. FTIR Spectra

The chemical and structural compositions of graphene oxide synthesized from graphite were studied through FTIR spectra analysis. Fourier Transform Infrared Spectra technique has been used to study nanomaterials and provides vital information about newly developed materials. This is achieved through studying the structural composition and functional groups of the materials [73]. The characteristic absorption bands of graphite and GO were exhibited by FTIR spectra as shown in Figure 4.1.

In Figure 4.1, graphite (a) FTIR spectrum showed absence of significant peaks, which is attributed to the chemical inertness of bulk graphite [255]. However, the FTIR spectrum of GO (b) showed a variation of present oxygen functional groups. A strong distinct band was found at  $3381\text{ cm}^{-1}$ , which is due to the O-H stretching vibration validating the presence of OH group in the structure. It may also indicate the presence of COOH group within the structure.

The peak at  $1720\text{ cm}^{-1}$  corresponded to the carbonyl, C=O stretching vibration, and C=C stretching vibration exhibited by a peak at  $1630\text{ cm}^{-1}$  is characteristic of unoxidized graphitic domain [256]. The C-O stretching vibration was confirmed by peaks at  $1197\text{ cm}^{-1}$  and  $1055\text{ cm}^{-1}$ , which can be attributed to the epoxy and alkoxy groups, respectively. There is a strong peak at  $860\text{ cm}^{-1}$  attributed to the *para*-disubstituted benzene ring, and a peak at  $578\text{ cm}^{-1}$  corresponding to epoxide groups that are located at the edge of GO sheet. Therefore, the FTIR analysis validated the presence of the various oxygen functional groups namely, hydroxyl, carboxyl,

carbonyl, and epoxy within the structure of GO. The observation correlates with findings for analysis of FTIR spectra of GO in literature [256].

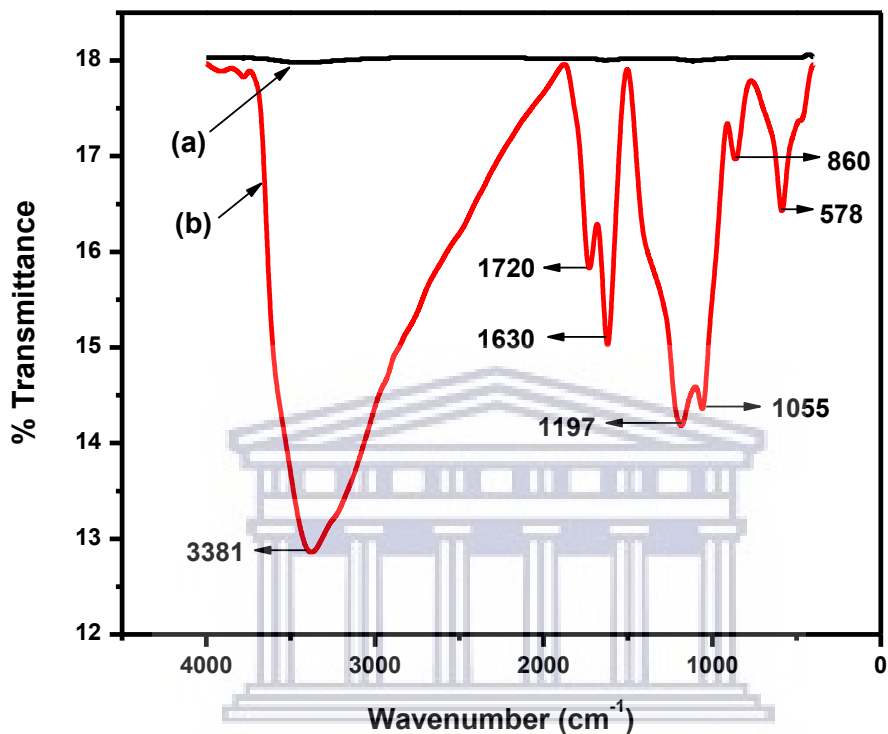


**Figure 4.1:** FTIR spectra of graphite (a) and GO (b).

### 4.3. Raman Spectra

Raman spectroscopy analysis was further used to confirm the conversion of graphite to GO and is commonly used to characterize carbon-based materials [73]. The spectra consider structural alteration that occurred through conjugated and carbon-carbon double bonds, which result in high intensity peaks [257]. Raman analysis of graphite and GO is interpreted in Figure 4.2.

In Figure 4.2, Raman spectrum of graphite (a) displayed a strong sharp peak at  $1557\text{ cm}^{-1}$  of the G band for first order scattering of  $E_{2g}$  phonon of  $sp^2$  C-atoms [73], and weak a peak at  $1339\text{ cm}^{-1}$  corresponding to the D band attributed to the disorder or defects in atomic arrangement [258]. A broad peak at  $2679\text{ cm}^{-1}$  of 2D band (G' band) was observed, which is an indication of the number of layers present in the structure [259].

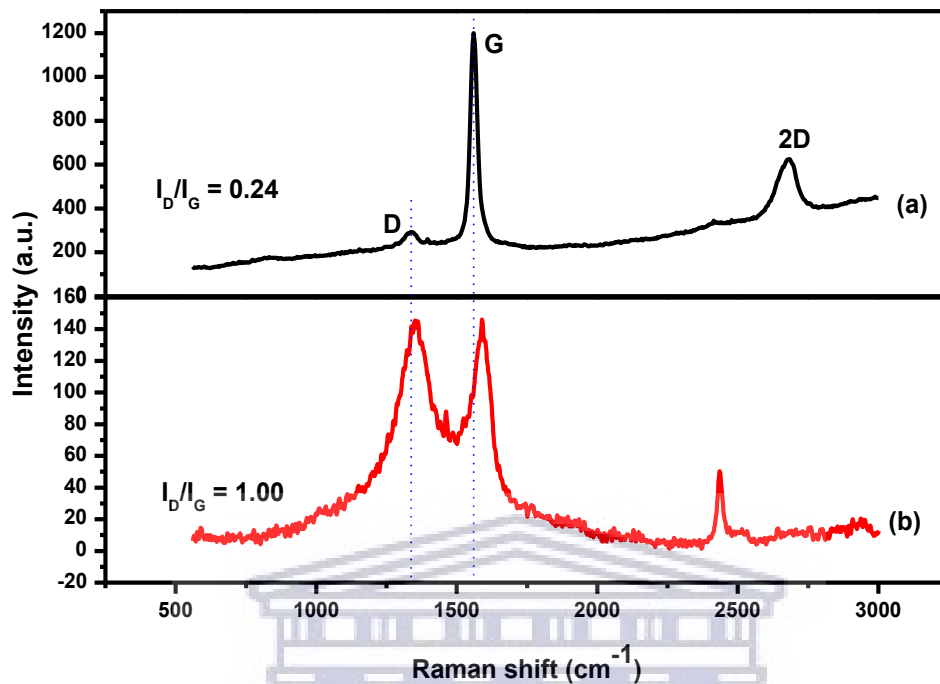


**Figure 4.2:** Raman spectra of graphite (a) and GO (b).

In comparison, Figure 4.2 shows that GO (b) had G and D bands that appear to have right-shifted. The spectrum was characterized by a G band at  $1590\text{ cm}^{-1}$  and a D band at  $1352\text{ cm}^{-1}$ . Furthermore, there was an observed peak for 2D band at  $2436\text{ cm}^{-1}$ . The 2D band present in GO may be an indication of a few layers in the structure. Shifting of the bands is justified by higher resonance frequency of the isolated double bonds in single layer of GO [260].

The ratio of peak intensities ( $I_D/I_G$ ) was determined for both graphite and GO. This can be used to investigate the level of disorder in graphite and GO [261, 262]. There was an increase observed for the determined ratio of  $I_D/I_G$  from graphite to the produced GO (0.24 to 1.00). The observation is an indication of decrease in size and crystallinity of graphitic material during chemical oxidation thereby implying a high defect density of the amorphous carbon structure ( $I_D/I_G = 0.24$  of graphite), whilst at the same time the increase in that of GO ( $I_D/I_G = 1.00$ ) corresponded to a low density regime [263]. Similar trends were observed in literature [256], which displays a successful conversion of graphite to GO.

#### 4.4. XRD Spectra

X-ray diffraction (XRD) analysis provided information regarding the chemical composition and changes of graphite into GO. The XRD spectra may be expected to entail information about lattice parameter, defects, strain, crystallite size of nanoparticles, and the type of molecular bond of crystalline phase [73]. Figure 4.3 depicts spectra of graphite and GO.

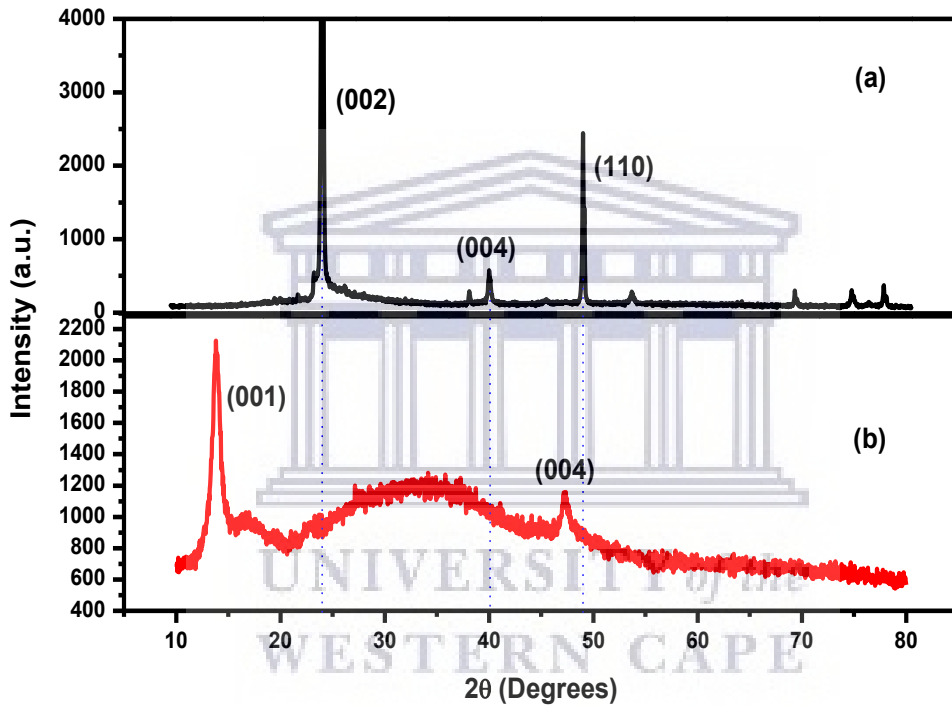


**Figure 4.3:** XRD spectra of (a) graphite and (b) GO.

The XRD pattern in Figure 4.3 (a) exhibited a typical peak at  $2\theta = 26.2^\circ$  that is characteristic of graphite, due to (002) reflection. Two further peaks were observed at  $2\theta = 44.3^\circ$  and  $2\theta = 54.4^\circ$  of the respective (004) and (110) reflection planes, which were attributed to high crystallinity of graphite. The corresponding d-spacing was found to be 0.38 nm. This was calculated using classical Debye-Scherrer equation [256]:

$$t = \frac{0.89\lambda}{\beta \cos\theta} \text{ and } n = \frac{t}{d} \quad (4.1)$$

where  $t$  = total thickness of layers,  $\beta$  = full width at half maxima,  $n$  = the number of layers,  $d$  = interlayer spacing or d-spacing,  $\theta$  = the diffraction angle, and  $\cos \theta$  is the value in radians. As graphite undergone oxidation, the peak at  $2\theta = 26.2^\circ$  resulted from (002) reflection plane disappeared with a new peak observed at  $2\theta = 8.85^\circ$  in Figure 4.3 (b) for GO. The newly emerged peak at  $2\theta = 8.85^\circ$  exhibited a shift in diffraction angle corresponding to (001) reflection plane. Furthermore, a slight shift of (004) reflection peak was observed at  $2\theta = 42.1^\circ$  for GO. There is a broad peak found between  $15.4^\circ$  and  $40.5^\circ$ , which indicated moisture contained in the GO powder and that it needed further drying prior to analysis. The d-spacing increased from 0.38 nm to 0.69 nm determined for the chemical conversion of graphite to GO. These observations were attributed to the presence of the oxygen containing functional groups such as hydroxyl, carboxyl, carbonyl, and epoxy contained in the GO structure [156, 264, 265]. Such patterns were validated by results found in literature [256].

#### ***4.5. High Resolution Scanning Electron Microscopy (HRSEM)***

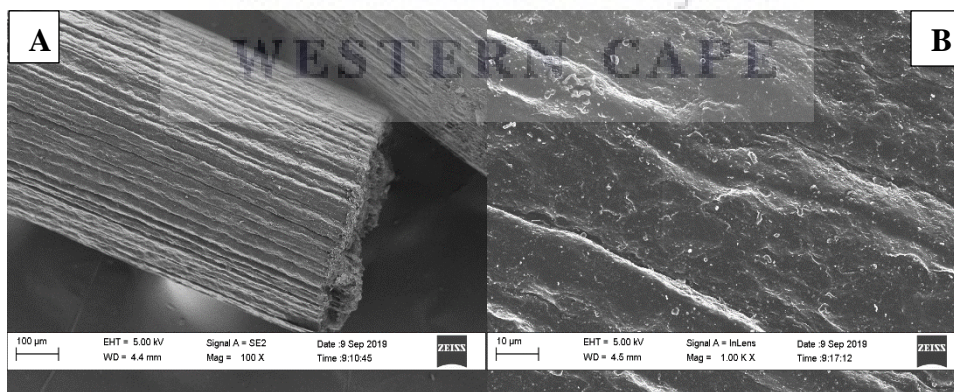
The electrochemical reduction of GO and GO-metal salts onto the electrode surface of PGE was examined using HRSEM. This was to study the morphology of the electrode before and after it had undergone modification through electro-deposition of the reduced materials. Figure 4.4 (I) shows HRSEM images of bare PGE [(A) – (B)], ERGO-PGE [(C) – (D)], ERGO-Sb-PGE [(E) – (F)], and ERGO-Au-PGE [(G) – (H)] at different magnifications.

The results show HRSEM images of bare PGE showed surface roughness with grooves in the direction of the machining [65], in Figure 4.4 (I) [(A)] at a lower magnification of 100 times. Upon close inspection, presence of impurities was displayed however still maintained “smoothness” observed at a higher magnification of 1000 times in Figure 4.4 (I) [(B)]. Electrochemical reduction of GO proceeded on the electrode, and Figure 4.4 (I) [(C) and (D)] show results at 100- and 1000-times magnifications, respectively. The electro-deposited contents along the grooves were observed with visible ruptures on the patterning. This was indicative of the electro-reduction of GO on the PGE.

Decoration of MNPs on the GO sheets and subsequent electro-reduction on the PGE followed, and Figure 4.4 (I) [(E) and (F)] show no apparent SbNPs. However, the energy dispersive x-ray spectrum (EDS) in Figure 4.4 (II) [(A)] obtained from HRSEM, with a close inspection in (C)

indicated presence of Sb element (0.14 %). The presence of SbNPs was further validated by electrochemical characterization in 0.5 mol.L<sup>-1</sup> HCl at a scan rate of 50 mV.s<sup>-1</sup>, and the CV in Figure 4.4 (III) [(A)] showed an oxidation peak potential at -0.44 V indicated by (I). This corresponds to the oxidation of Sb<sup>0</sup> to Sb<sup>3+</sup>; no apparent reduction peak was observed. Cesarino et al. [266] confirmed the presence RGO-SbNPs on GCE by SEM, for which the size of SbNPs varied between 5 and 40 nm. These findings were also confirmed by electrochemical characterization in which CV experiments proceeded in HCl solution at a scan rate of 50 mV.s<sup>-1</sup> (oxidation peak at -0.034 V) [266].

Morphology of ERGO-Au-PGE nanocomposite also showed no presence of AuNPs (0.00 %). Furthermore, the EDS in Figure 4.4 (II) [(B)] and a close up in (D) also confirmed this observation. This was not supposed to be the case when compared with recent studies using similar electro-deposition technique, in which SEM showed successful decoration of AuNPs on ERGO morphology [267, 268]. However, the CV in Figure 4.4 (III) [(B)] showed a broad oxidation peak at +0.88 V indicated by (II) for the oxidation of Au<sup>0</sup> to Au<sup>3+</sup>, and a reduction peak (III) at +0.51 V for the subsequent reduction back to metallic gold. Rhei and VytasReipa [269] recorded an oxidation peak potential of +0.85 V and reduction peak at +0.54 V for ITO electrode modified with AuNPs. Findings in the current study indicate that there need to be further analysis in future for precise and accurate results.



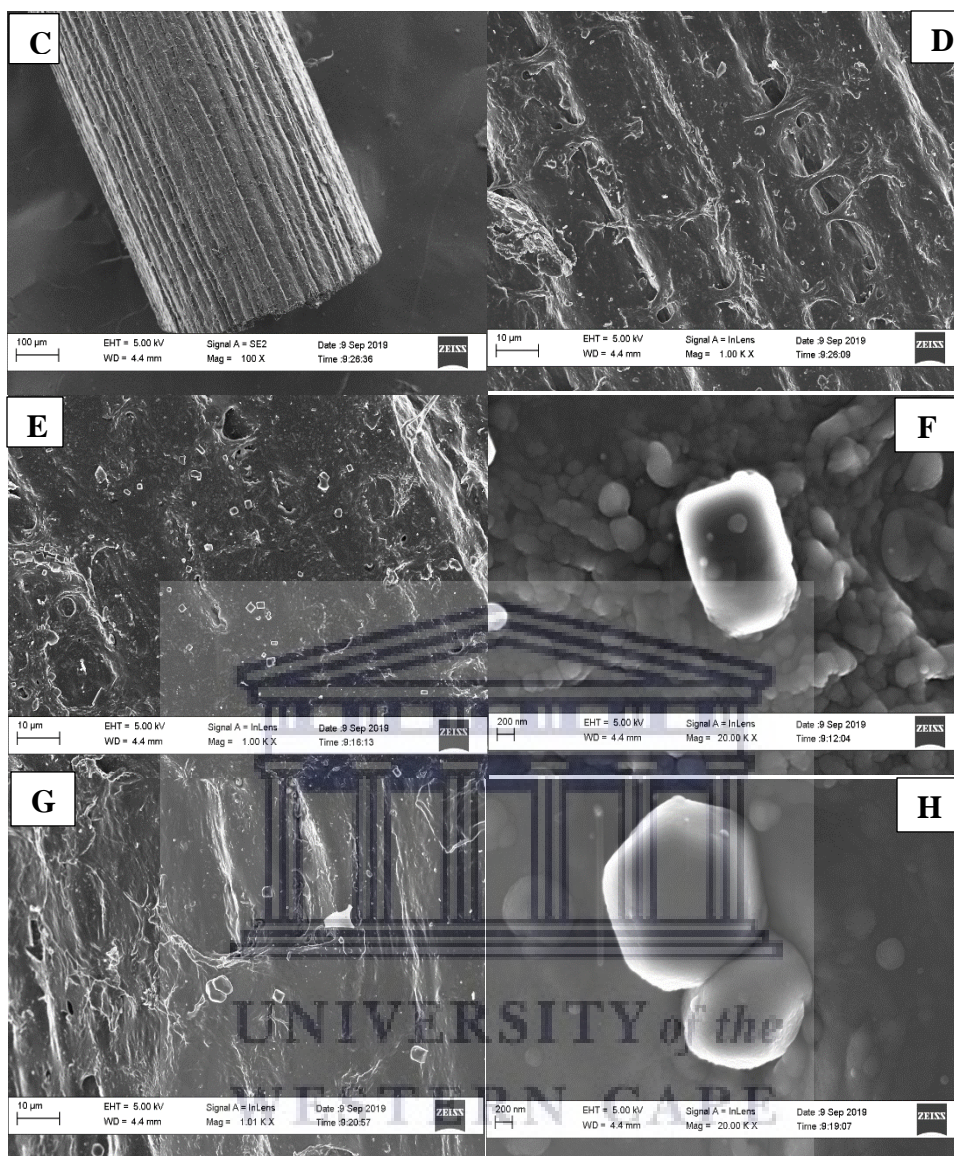


**Figure 4.4 (D):** HRSEM images of bare PGE [(A) – (B)] and ERGO-PGE [(C) – (D)] shown at 100 (left) and 1000 (right) times, and ERGO-Sb-PGE [(E) – (F)] and ERGO-Au-PGE [(G) – (H)] shown at 1000 K (left) and 20000 (right) times magnifications.

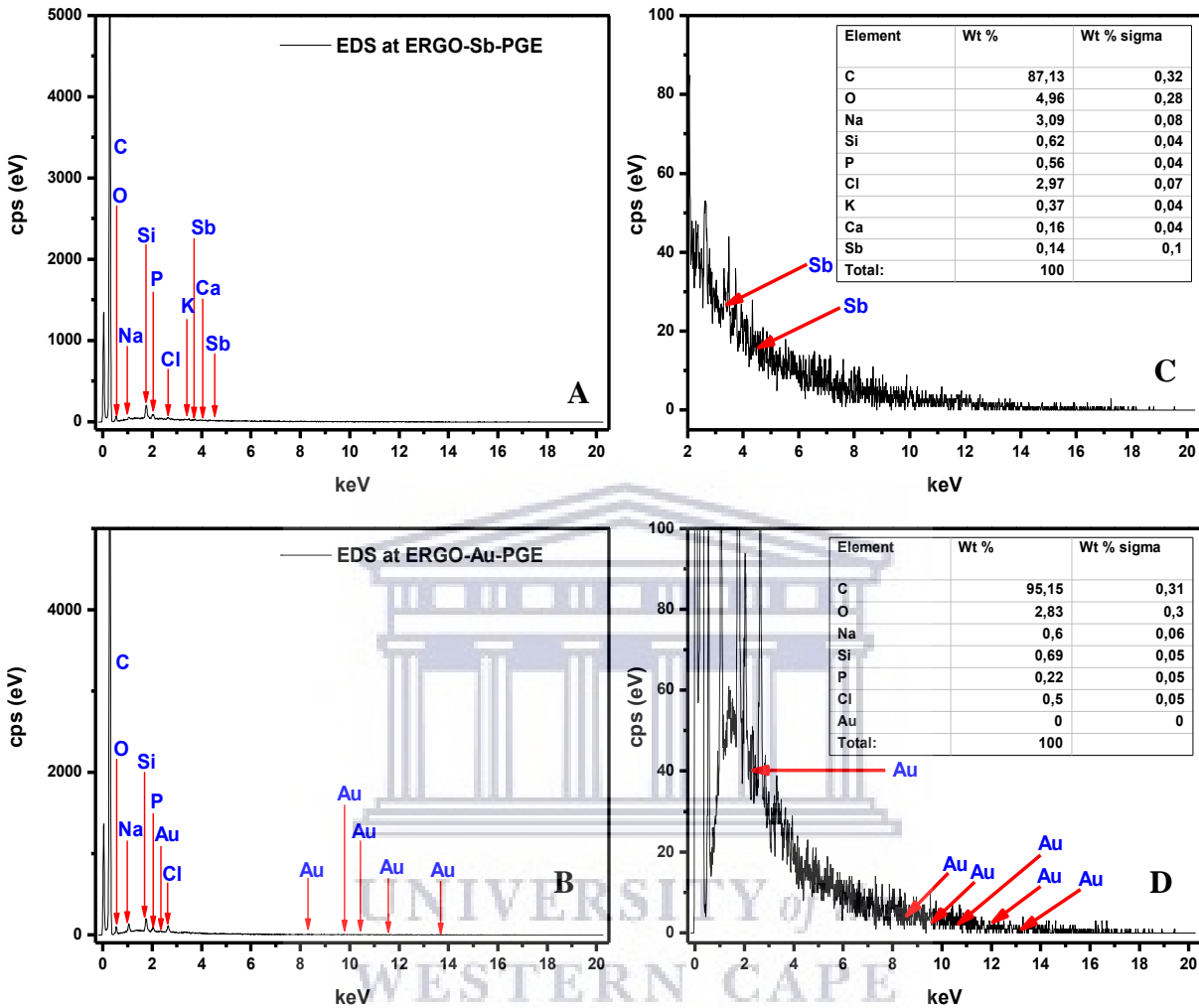


**Figure 4.4 (II):** EDS of ERGO-Sb-PGE (A) and ERGO-Au-PGE (B) followed by the amplified images in (C) and (D), respectively. Insert: Tables showing elemental composition of the reduced material.

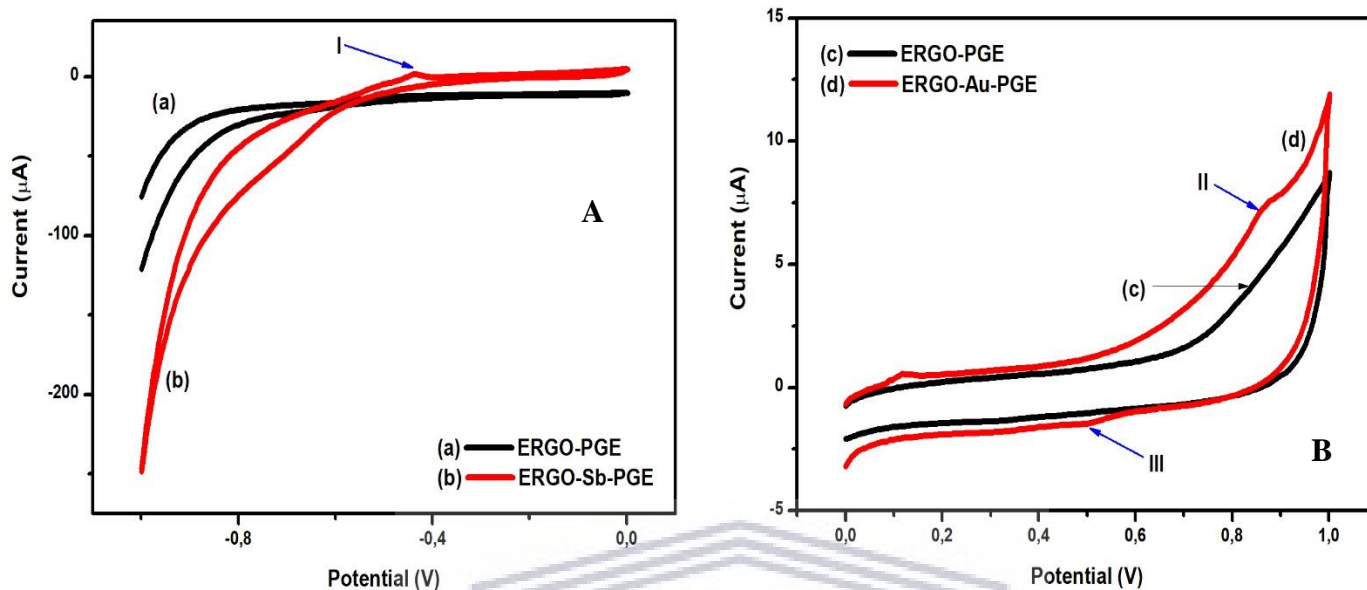


**Figure 4.4 (III):** Cyclic voltammery characterization in 0.5 mol.L<sup>-1</sup> HCl at a scan rate of 50 mV.s<sup>-1</sup> for the electrodes: ERGO-PGE (a) with ERGO-Sb-PGE (b) in (A), and ERGO-PGE (c) with ERGO-Au-PGE (d) in (B). oxidation of Sb<sup>0</sup> to Sb<sup>3+</sup> shown at I, and that of Au<sup>0</sup> to Au<sup>3+</sup> at II and the reduction of Au<sup>3+</sup> to Au<sup>0</sup> at III.

#### 4.6. High Resolution Transmission Electron Microscopy (HRTEM)

The morphological analysis of graphite and the prepared GO proceeded using transmission electron microscopy (TEM). Transmission electron microscopy (TEM) technique allows for accurate identification of the thickness of graphene sheets [199]. Preparation for graphite and GO samples proceeded as stipulated in section 3.9.5. Graphite and GO prepared solutions were drop-casted onto Cu grids for HRTEM analysis. Figure 4.5 shows HRTEM images, and the corresponding selected area electron diffraction (SAED) patterns of graphite and GO, respectively.

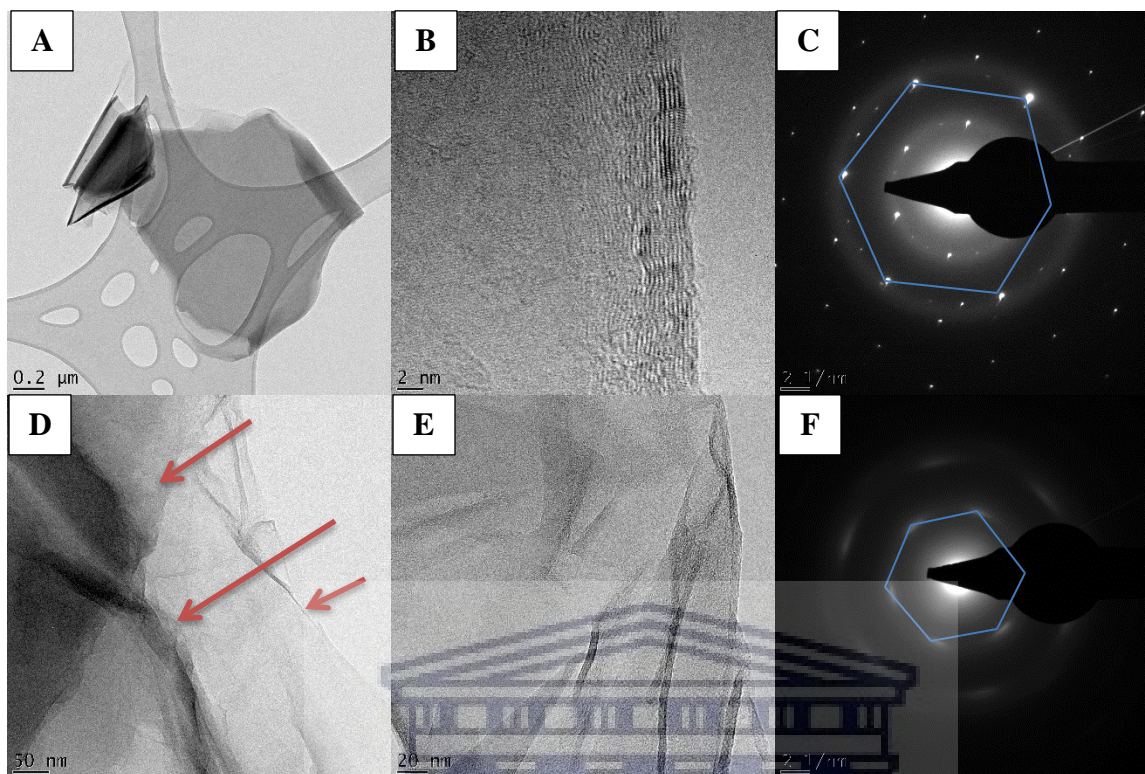


**Figure 4.5:** HRTEM images of graphite [(A) and (B)] and GO [(D) and (E)], and the corresponding SAED patterns in (C) and (F), respectively.

Graphite images displayed dark flakes with no distinct shape and straight edges as shown in Figure 4.5 (A); also shown at different scanned regions and higher magnification in (B) and the corresponding selected area electron diffraction (SAED) in (C) pattern. However, in Figure 4.5 (D) it can be observed that GO layers had been delaminated and separate sheets were apparent which can be attributed to chemical exfoliation [256]. There is some stacking as indicated by the arrows, and the morphology revealed some wrinkling or folding of the stacked layers at the edges. The edges were also characteristic of transparency in Figure 4.5 (E) due to low thickness and an indication of monolayer GO [138]. A selected area electron diffraction (SAED) was performed and the pattern shown in Figure 4.5 (F) had clear bright visible spots that validated the presence of crystallinity in the GO structure. These diffraction spots formed a hexagon and thus confirming the hexagonal lattice structure of GO [256]. These showed successful conversion of graphite to GO.

## CHAPTER FIVE:

# Electrochemical Oxidation of Paracetamol at Electrochemically Reduced Graphene Oxide-Antimony Nanocomposite Modified Pencil Graphite Electrode

### 5.1. Introduction

In this chapter, the electro-oxidation of PC at the electrochemically modified electrodes is discussed. The effect of modification of electrodes on the electrochemical determination of PC was demonstrated using adsorptive stripping voltammetric analysis.

### 5.2. Electrochemical Characterizations

#### 5.2.1. Electrochemical Properties

An electrochemical sensor was developed through electrochemical modification with graphene oxide-antimony salt to produce electrochemically reduced graphene oxide-antimony nanocomposite pencil graphite electrode (ERGO-Sb-PGE). The electrochemical characteristics of ERGO-Sb-PGE were studied to evaluate electrode surface, which thereafter it was to be used for subsequent experiments in the study. Electrochemical properties of the modified electrode surface were investigated by CV and electrochemical impedance spectroscopy (EIS) using  $K_3[Fe(CN)_6]$  as an electrochemical probe. Cyclic voltammetry is used to study electroactive species and to monitor the redox behavior of chemical species within a wide potential range [270]. Electrochemical impedance spectroscopy is known to be a powerful tool used to study interfacial processes at the electrode surface [271]. Generally,  $K_3[Fe(CN)_6]$  is used as an electrochemical probe to electrochemically characterize unmodified and modified electrode surfaces [272].

The response of the ERGO-Sb-PGE towards the redox reaction of  $[Fe(CN)_6]^{3-/4-}$  in solution was investigated using CV. The established potential range of -1.0 to +1.0 V vs. Ag/AgCl (3 mol.L<sup>-1</sup> KCl) in 5 mmol.L<sup>-1</sup>  $K_3[Fe(CN)_6]$  in 0.1 mol.L<sup>-1</sup> KCl solution at a scan rate of 50 mV.s<sup>-1</sup> was subsequently used for CV experiments. The comparison of the cyclic voltammograms of

$[\text{Fe}(\text{CN})_6]^{3-/4-}$  redox couple at bare PGE (a), ERGO-PGE (b), and ERGO-Sb-PGE (c) in 5 mmol.L<sup>-1</sup> K<sub>3</sub>[Fe(CN)<sub>6</sub>] in 0.1 mol.L<sup>-1</sup> KCl solution is displayed in Figure 5.1.

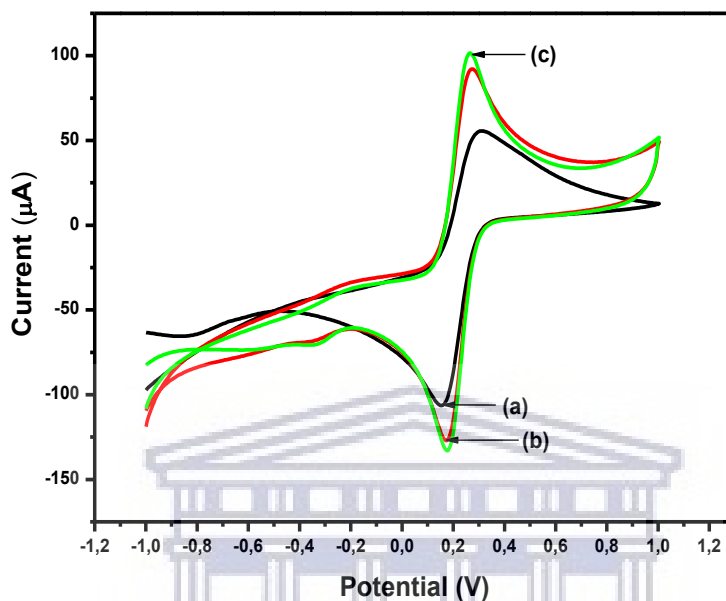


**Figure 5.1:** Cyclic voltammograms of  $[\text{Fe}(\text{CN})_6]^{3-/4-}$  (5 mmol.L<sup>-1</sup>) in 0.1 mol.L<sup>-1</sup> KCl solution at bare PGE (a), ERGO-PGE (b), and ERGO-Sb-PGE (c) at a scan rate of 50 mV.s<sup>-1</sup>.

The redox reaction of  $[\text{Fe}(\text{CN})_6]^{3-/4-}$  at bare PGE (a) yielded peak currents of  $I_{\text{pa}} = 5.40 \times 10^{-5}$  A and  $I_{\text{pc}} = -7.28 \times 10^{-5}$  A, which exhibited low current signal that may be attributed to the lack of electrocatalytic activity towards the redox couple. However, the redox peak current response improved with modification of the electrode; ERGO-PGE (b) with respective  $I_{\text{pa}} = 7.90 \times 10^{-5}$  A and  $I_{\text{pc}} = -9.48 \times 10^{-5}$  A, and ERGO-Sb-PGE (c) had  $I_{\text{pa}} = 9.17 \times 10^{-5}$  A and  $I_{\text{pc}} = -9.88 \times 10^{-5}$  A. The enhancement from ERGO-PGE to ERGO-Sb-PGE was by a factor of 1.2 and 1.04 for anodic ( $I_{\text{pa}}$ ) and cathodic peaks ( $I_{\text{pc}}$ ), respectively. The peak current ratio was determined for the electrodes in which bare PGE had  $I_{\text{pc}}/I_{\text{pa}} = 1.3$ , ERGO-PGE with  $I_{\text{pc}}/I_{\text{pa}} = 1.2$ , and ERGO-Sb-PGE had  $I_{\text{pc}}/I_{\text{pa}} = 1.08$ .

These values were required to be equal to 1 to determine the reversibility or quasi-reversibility, or otherwise irreversibility ( $I_{\text{pc}}/I_{\text{pa}} < 1$ ) of the system. However, the  $\Delta E_p$  values observed were greater than  $0.059/n$  V, which corresponded to a quasi-reversible electrochemical process. The

peak separation ( $\Delta E_p$ ) for a reversible system is approximately  $0.059/n$  V at 298 K and it is independent of scan rate, and for irreversibility  $\Delta E_p$  shifts with scan rate [273]. Peak separations ( $\Delta E_p$ ) were decreased with improved modification in the following order;  $155 \text{ mV} > 104 \text{ mV} > 90 \text{ mV}$  for the respective bare PGE, ERGO-PGE, and ERGO-Sb-PGE, and their redox peak currents increased in this order, thus inducing a faster electron transfer of  $[\text{Fe}(\text{CN})_6]^{3-/4-}$  redox couple at the electrode surface which can be attributed to the larger surface area due to GO and electrocatalytic activity of the synergistic effect of ERGO and modification with the expected SbNPs [266].

### 5.2.2. Electrochemical Impedance Spectroscopic Analysis

The electrodes were further electrochemically characterized using EIS in  $5 \text{ mmol.L}^{-1} [\text{Fe}(\text{CN})_6]^{3-/4-}$  in  $0.1 \text{ mol.L}^{-1}$  KCl solution. The Nyquist plots of bare PGE (a), ERGO-PGE (b), and ERGO-Sb-PGE (c) are shown in Figure 5.2. Each plot is composed of a semi-circle which corresponded to the charge transfer resistance ( $R_{ct}$ ) which controls the charge transfer kinetics at the solution-electrode interface. Charge transfer resistance is represented by the endpoint of diameter of the semi-circle in the higher values of  $Z'$ -axis [274].

Bare PGE presented a well-defined semi-circle that corresponded to a higher  $R_{ct}$  value of  $1368 \Omega$ . Modification of electrode with ERGO showed decreased  $R_{ct}$  and further so for ERGO-Sb-PGE with values of  $362.8 \Omega$  and  $236.9 \Omega$ , respectively. The inclined line at higher region of  $Z'$ -axis was attributed to the Warburg impedance due to the diffusion of  $[\text{Fe}(\text{CN})_6]^{3-/4-}$  to and from electrode surface, suggesting that the kinetics of the electrode process were diffusion-controlled at higher region of  $Z'$ -axis and controlled by charge transfer at lower region of  $Z'$ -axis [274]. The diffusion process occurs by movement of  $[\text{Fe}(\text{CN})_6]^{3-/4-}$  from solution to the electrode surface which consist of active reaction sites. The  $[\text{Fe}(\text{CN})_6]^{3-/4-}$  move from a high concentrated region to a lower concentrated one between the electrolyte and surface. The interface created between solution and electrode surface corresponds to the double layer capacitance ( $C_{dl}$ ), which is due to the surface roughness, and it is represented by the midpoint of the semi-circle in the Nyquist plot [274]. The  $R_{ct}$  values for the impedimetric analysis were obtained by fitting from an equivalent electrical circuit (insert in Figure 5.2). Based on observed values from the bare PGE to the ERGO-Sb-PGE, these indicate that charge transfer becomes faster with less resistance. Therefore the purpose of modification of the PGE was validated in the experiments.

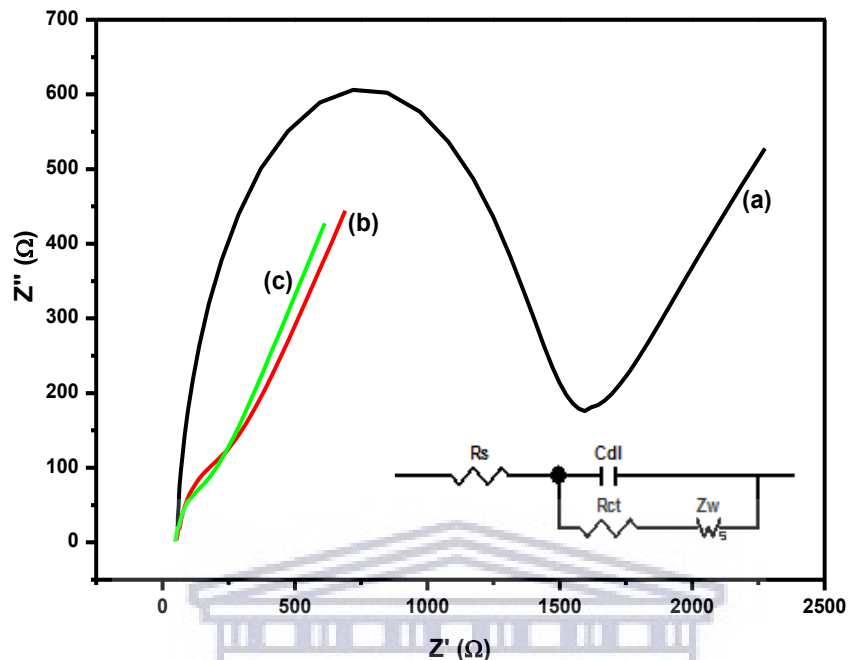


**Figure 5.2:** Nyquist plot of  $[\text{Fe}(\text{CN})_6]^{3-/4-}$  ( $5 \text{ mmol.L}^{-1}$ ) in  $0.1 \text{ mol.L}^{-1}$  KCl solution at bare PGE (a), ERGO-PGE (b), and ERGO-Sb-PGE (c). Insert: Equivalent circuit fitting.

### 5.2.3. Effect of Scan Rate on $[\text{Fe}(\text{CN})_6]^{3-/4-}$ Redox Couple

Cyclic voltammetry was used to electrochemically characterize the electrode surface. It was further used to study the effect of varying scan rate of the  $[\text{Fe}(\text{CN})_6]^{3-/4-}$  redox couple at bare PGE, ERGO-PGE, and ERGO-Sb-PGE. The process proceeded in  $5 \text{ mmol.L}^{-1}$   $\text{K}_3\text{Fe}(\text{CN})_6$  in  $0.1 \text{ mol.L}^{-1}$  KCl solution over a scan rate range of  $10 - 100 \text{ mV.s}^{-1}$ . Subsequent voltammograms and their corresponding linear plots are shown in Figure 5.3 (I) – (III) [(A) – (D)] in each case.

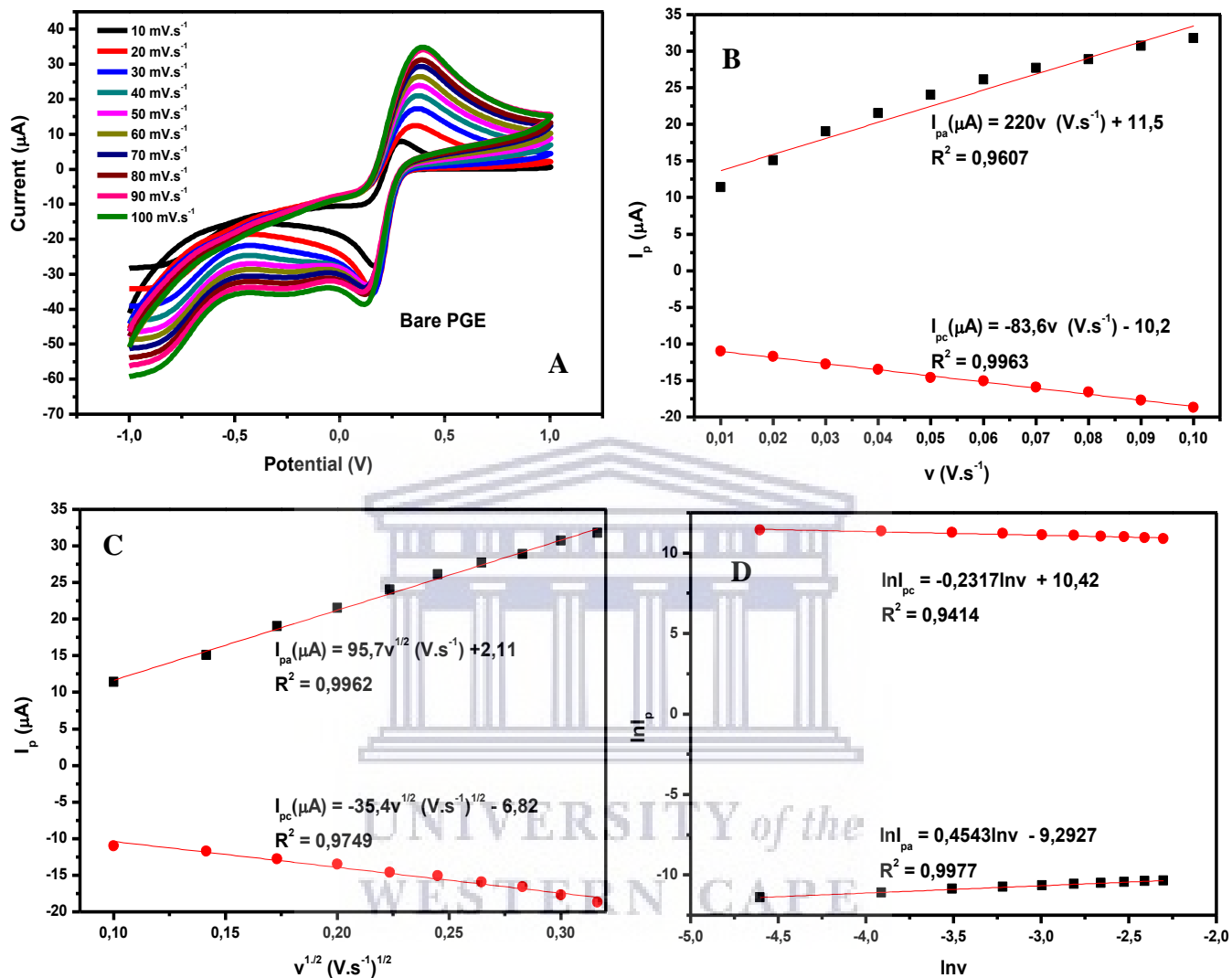


**Figure 5.3 (I):** Cyclic voltammograms of bare PGE in 5 mmol.L<sup>-1</sup> [Fe(CN)<sub>6</sub>]<sup>3-/4-</sup> in 0.1 mol.L<sup>-1</sup> KCl solution over a scan rate range of 10 – 100 mV.s<sup>-1</sup> (A). Accompanying linear plots of scan rate and square root of scan rate with peak currents (B) and (C), respectively. The plot of lnI<sub>p</sub> and lnv is shown in (D).

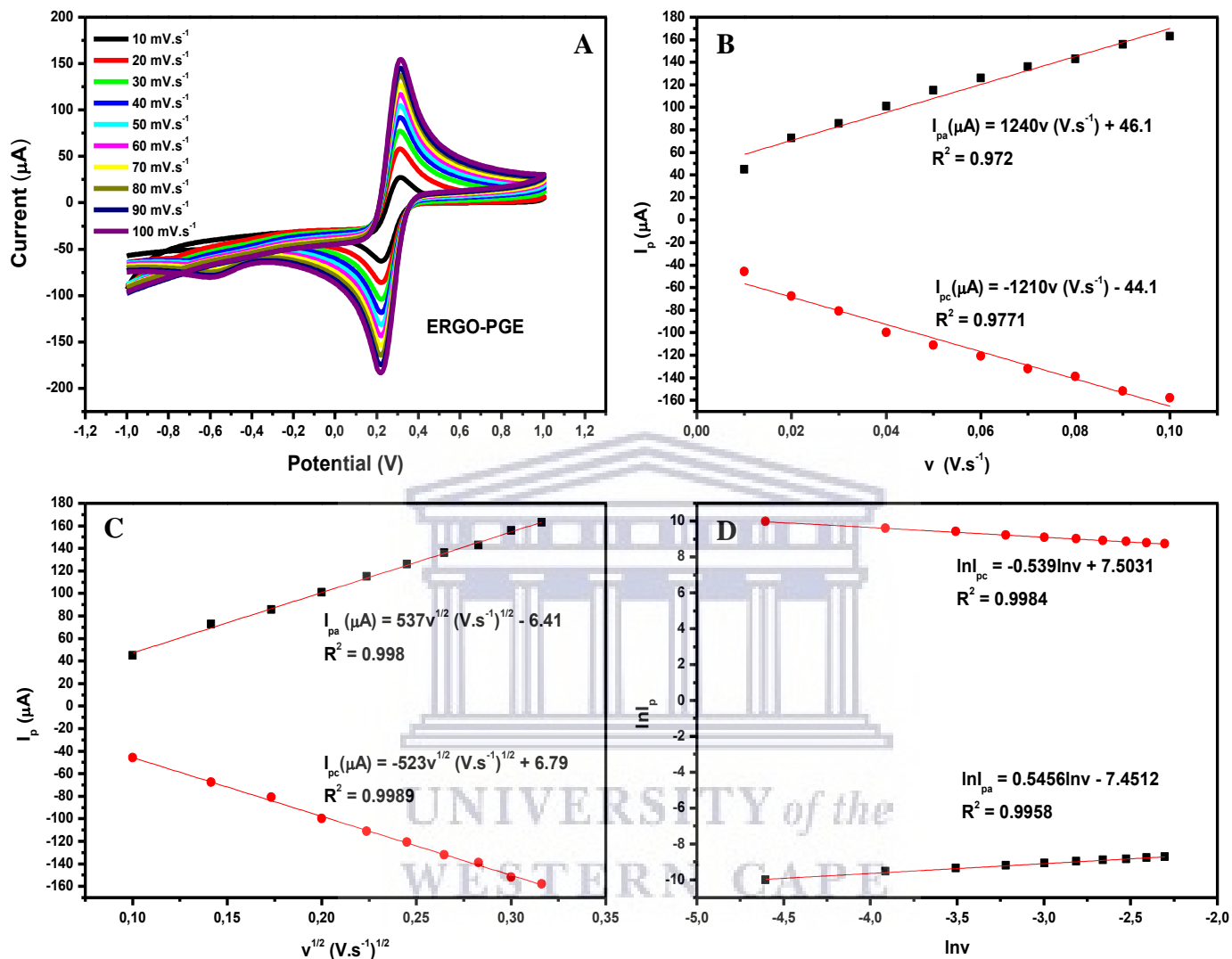


**Figure 5.3 (II):** Cyclic voltammograms of ERGO-PGE in  $5 \text{ mmol}\cdot\text{L}^{-1} [\text{Fe}(\text{CN})_6]^{3-/4-}$  in  $0.1 \text{ mol}\cdot\text{L}^{-1}$  KCl solution over a scan rate range of  $10 - 100 \text{ mV}\cdot\text{s}^{-1}$  (A). Accompanying linear plots of scan rate and square root of scan rate with peak currents (B) and (C), respectively. The plot of  $\ln I_p$  and  $\ln v$  is shown in (D).

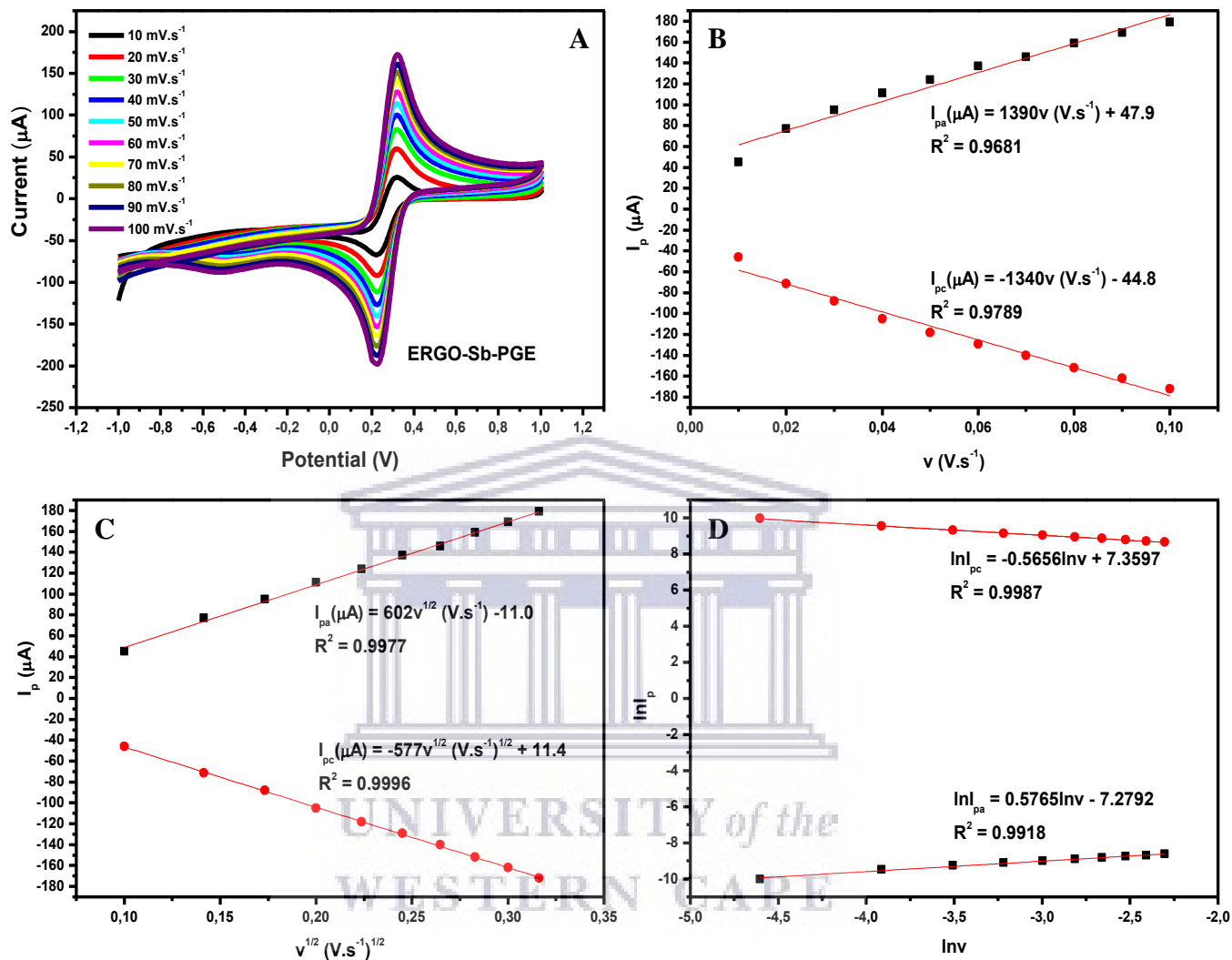


**Figure 5.3 (III):** Cyclic voltammograms of ERGO-Sb-PGE in 5 mmol.L<sup>-1</sup> [Fe(CN)<sub>6</sub>]<sup>3-/4-</sup> in 0.1 mol.L<sup>-1</sup> KCl solution over a scan rate range of 10 – 100 mV.s<sup>-1</sup> (A). Accompanying linear plots of scan rate and square root of scan rate with peak currents (B) and (C), respectively. The plot of lnI<sub>p</sub> and lnv is shown in (D).

Figure 5.3 [(I) – (III)] (A) shows increasing oxidation and reduction peak currents with increasing scan rate for the [Fe(CN)<sub>6</sub>]<sup>3-/4-</sup> redox couple from the first to the last scan, and (B) in

each case shows the linear plots for peak current against scan rate corresponding to the electrodes under investigation with their regression equations given as follows;

Bare PGE:

$$I_{pa} \text{ (A)} = 2.36 \times 10^{-4} \nu \text{ (V.s}^{-1}\text{)} + 1.20 \times 10^{-5} \text{ (R}^2 = 0.9437\text{)}$$

$$I_{pc} \text{ (A)} = -5.44 \times 10^{-5} \nu \text{ (V.s}^{-1}\text{)} - 1.24 \times 10^{-5} \text{ (R}^2 = 0.8992\text{)}$$

ERGO-PGE:

$$I_{pa} \text{ (A)} = 1.24 \times 10^{-3} \nu \text{ (V.s}^{-1}\text{)} + 4.61 \times 10^{-5} \text{ (R}^2 = 0.972\text{)}$$

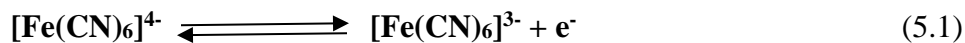
$$I_{pc} \text{ (A)} = -1.21 \times 10^{-3} \nu \text{ (V.s}^{-1}\text{)} - 4.41 \times 10^{-5} \text{ (R}^2 = 0.9771\text{)}$$

ERGO-Sb-PGE:

$$I_{pa} \text{ (A)} = 1.39 \times 10^{-3} \nu \text{ (V.s}^{-1}\text{)} + 4.79 \times 10^{-5} \text{ (R}^2 = 0.9681\text{)}$$

$$I_{pc} \text{ (A)} = -1.34 \times 10^{-3} \nu \text{ (V.s}^{-1}\text{)} - 4.48 \times 10^{-5} \text{ (R}^2 = 0.9789\text{)},$$

where  $I_{pa}$  and  $I_{pc}$  correspond to the oxidation and reduction peak currents, respectively. These are the responses of  $[\text{Fe}(\text{CN})_6]^{3-/4-}$  obtained at the electrode surface in each statement. As the electrode is immersed in solution rich in  $[\text{Fe}(\text{CN})_6]^{3-/4-}$  species, these are pre-concentrated around the electrode. When the voltage is applied, the  $[\text{Fe}(\text{CN})_6]^{3-/4-}$  redox occurs at the electrode surface, with the species being transferred back and forth between the solution and electrode surface. In the two species involved;  $[\text{Fe}(\text{CN})_6]^{4-}$  is oxidized to  $[\text{Fe}(\text{CN})_6]^{3-}$  in the forward scan in which one electron is lost, and the reverse allows for reduction of  $[\text{Fe}(\text{CN})_6]^{3-}$  back to  $[\text{Fe}(\text{CN})_6]^{4-}$  with the electron gained (Eq. 5.1). The responses are obtained in the form of current as function of potential. Thus, this occurrence was attributed to the heterogeneous kinetics and the IR effect [271].



From the slope values deduced from the plot of  $I_p$  vs  $\nu$  in Figure 5.3 [(I) – (III)] (B), electrode surface coverage capacity for bare PGE ( $I_p/\nu = 2.36 \times 10^{-4} \text{ A/V.s}^{-1}$ ), ERGO-PGE ( $I_p/\nu = 1.24 \times 10^{-3} \text{ A/V.s}^{-1}$ ), and ERGO-Sb-PGE ( $I_p/\nu = 1.39 \times 10^{-3} \text{ A/V.s}^{-1}$ ) was calculated using the following formula:

$$I_p = \frac{n^2 F^2 \Gamma A v}{4RT} \quad (5.2)$$

where  $n = 1$  is the number of electrons involved,  $A = 0.16 \text{ cm}^2$  is the surface area,  $F$  is the Faraday constant ( $F = 96485 \text{ C.mol}^{-1}$ ),  $\Gamma$  the surface coverage of the adsorbed species,  $R$  the molar gas constant ( $R = 8.314 \text{ J.K}^{-1}.\text{mol}^{-1}$ ), and  $T$  is the temperature ( $T = 298 \text{ K}$ ). The electrode coverage capacity was determined to be  $1.57 \times 10^{-9} \text{ mol.cm}^{-2}$ ,  $8.25 \times 10^{-9} \text{ mol.cm}^{-2}$ , and  $9.25 \times 10^{-9} \text{ mol.cm}^{-2}$  for the respective bare PGE, ERGO-PGE, and ERGO-Sb-PGE. These displayed an increase in surface coverage from the unmodified to the modified electrodes for the adsorption of the active species to the surface, which is the indication of the ease of electrocatalytic activity of the electrode in the ascending order.

As it can be observed from the correlation coefficient ( $R^2$ ) values obtained in the plot of  $I_p$  vs  $v$  for each electrode where they are slightly further from 1, there is no clear linearity indicated. The linearity and/or non-linearity of the plot provides an indication as to whether the electrochemical process under investigation is diffusion- and/or adsorption-controlled. Therefore, further investigation is required and so the plot of square root of scan rate with peak current was studied.

In (C) of Figure 5.3 (I) – (III), the plots showed that peak current increased linearly with the square root of scan rate. In the stated regression equations,  $R^2$  closer to the value of 1 indicated linearity and thus the electrochemical process was driven by diffusion at the electrode surface. The peak current response of the reduction process at bare PGE had no apparent linearity with  $R^2 = 0.9385$ , which may be once again be due to difficulty attributed to lack of electrocatalytic activity at the electrode surface. The regression equations for the electrodes under investigation are given below;

Bare PGE:

$$I_{pa} \text{ (A)} = 1.03 \times 10^{-4} v^{1/2} (\text{V.s}^{-1})^{1/2} - 1.81 \times 10^{-6} \quad (R^2 = 0.9902)$$

$$I_{pc} \text{ (A)} = -2.59 \times 10^{-5} v^{1/2} (\text{V.s}^{-1})^{1/2} + 9.47 \times 10^{-6} \quad (R^2 = 0.9385)$$

ERGO-PGE:

$$I_{pa} \text{ (A)} = 5.37 \times 10^{-4} v^{1/2} (\text{V.s}^{-1})^{1/2} - 6.41 \times 10^{-6} \text{ (R}^2 = 0.9975)$$

$$I_{pc} \text{ (A)} = -5.23 \times 10^{-4} v^{1/2} (\text{V.s}^{-1})^{1/2} + 8.56 \times 10^{-6} \text{ (R}^2 = 0.9982)$$

ERGO-Sb-PGE:

$$I_{pa} \text{ (A)} = 6.02 \times 10^{-4} v^{1/2} (\text{V.s}^{-1})^{1/2} - 1.10 \times 10^{-5} \text{ (R}^2 = 0.9977)$$

$$I_{pc} \text{ (A)} = -5.77 \times 10^{-4} v^{1/2} (\text{V.s}^{-1})^{1/2} - 1.14 \times 10^{-5} \text{ (R}^2 = 0.9996)$$

Diffusion coefficients of  $[\text{Fe}(\text{CN})_6]^{3-/4-}$  ions in solution were calculated using Randles-Sevcik equation (Eq. 5.3) at room temperature, where  $n$  and  $A$  were previously described,  $D$  the diffusion coefficient, and  $C = 5 \times 10^{-6} \text{ mol.cm}^{-3}$  is the concentration of  $[\text{Fe}(\text{CN})_6]^{3-/4-}$  ions in solution. The slope ( $I_p/v^{1/2}$ ) values were obtained from the plots for each electrode as follows; bare PGE ( $I_{pa}/v^{1/2} = 1.03 \times 10^{-4} \text{ A}/(\text{V.s}^{-1})^{1/2}$ ;  $I_{pc}/v^{1/2} = -2.59 \times 10^{-5} \text{ A}/(\text{V.s}^{-1})^{1/2}$ ), ERGO-PGE ( $I_{pa}/v^{1/2} = 5.37 \times 10^{-4} \text{ A}/(\text{V.s}^{-1})^{1/2}$ ;  $I_{pc}/v^{1/2} = -5.23 \times 10^{-4} \text{ A}/(\text{V.s}^{-1})^{1/2}$ ), and ERGO-Sb-PGE ( $I_{pa}/v^{1/2} = 6.02 \times 10^{-4} \text{ A}/(\text{V.s}^{-1})^{1/2}$ ;  $I_{pc}/v^{1/2} = -5.77 \times 10^{-4} \text{ A}/(\text{V.s}^{-1})^{1/2}$ ).

$$I_p = (2.69 \times 10^5) n^2 D^{1/2} A C v^{1/2} \quad (5.3)$$

The  $D$  values were estimated to be  $2.29 \times 10^{-7} \text{ cm}^2.\text{s}^{-1}$  for anodic peak and  $1.45 \times 10^{-8} \text{ cm}^2.\text{s}^{-1}$  for cathodic peak for bare PGE,  $6.23 \times 10^{-6} \text{ cm}^2.\text{s}^{-1}$  for anodic peak and for cathodic peak it was  $5.91 \times 10^{-6} \text{ cm}^2.\text{s}^{-1}$  for ERGO-PGE, and for ERGO-Sb-PGE these were  $7.83 \times 10^{-6} \text{ cm}^2.\text{s}^{-1}$  for anodic peak and  $7.18 \times 10^{-6} \text{ cm}^2.\text{s}^{-1}$  was cathodic peak response. The active electrode surface areas were estimated using the precise well-known diffusion coefficient value of ferrocyanide ( $6.20 \times 10^{-6} \text{ cm}^2.\text{s}^{-1}$ ) [275]. These were determined to be  $0.0312 \text{ cm}^2$ ,  $0.162 \text{ cm}^2$ , and  $0.182 \text{ cm}^2$  attributed to bare PGE, ERGO-PGE, and ERGO-Sb-PGE. There was an increase observed in an ascending order from bare PGE to ERGO-Sb-PGE owing to the electrocatalytic sites increased by modification of electrode.

The diffusion capability of  $[\text{Fe}(\text{CN})_6]^{3-/4-}$  species at the electrode surface was further investigated by studying the plot of  $\ln I_p$  vs  $\ln v$ . It is one of the two approaches, with the other being the analysis of  $I_p$  on  $v^{1/2}$ , used to determine whether the reaction rate is controlled by adsorption or

diffusion [268]. Therefore,  $\ln I_p$  is plotted with  $\ln v$  in (D) of Figure 5.3 (I) – (III) for each electrode under investigation and their regression equations were obtained as follows;

Bare PGE:

$$\ln I_{pa} = 0.4747 \ln v - 9.1765 \quad (R^2 = 0.994)$$

$$\ln I_{pc} = -0.1622 \ln v + 10.587 \quad (R^2 = 0.9836)$$

ERGO-PGE:

$$\ln I_{pa} = 0.5456 \ln v - 7.4512 \quad (R^2 = 0.9958)$$

$$\ln I_{pc} = -0.539 \ln v + 7.5031 \quad (R^2 = 0.9984)$$

ERGO-Sb-PGE:

$$\ln I_{pa} = 0.5765 \ln v - 7.2792 \quad (R^2 = 0.9918)$$

$$\ln I_{pc} = -0.5656 \ln v + 7.3597 \quad (R^2 = 0.9987)$$

As can be observed, the slopes obtained from these equations were close to the theoretical slope of 0.5 and they correspond to a process driven by diffusion [271]. The exception was with the cathodic process of the bare PGE, in which the slope was found to be -0.1622. This showed the complexity of electrochemical process at this particular electrode, which is an indication of difficulty of diffusion and/or adsorption of ions due to lack of modification of the surface.

### **5.3. Electro-oxidation of PC at ERGO-Sb-PGE**

The ERGO-Sb-PGE developed and electrochemically characterized was used for the electrochemical oxidation of PC. The experiments were conducted on three different electrodes namely, bare PGE (a), ERGO-PGE (b), and ERGO-Sb-PGE (c). The DPV experiments were carried out in the potential range 0.0 to +1.0 V vs. Ag/AgCl (3 mol.L<sup>-1</sup>KCl) in 0.1 mol.L<sup>-1</sup> PBS at pH 7.0 containing 10 μmol.L<sup>-1</sup> PC solution. The comparison of the peak currents is shown in Figure 5.4.

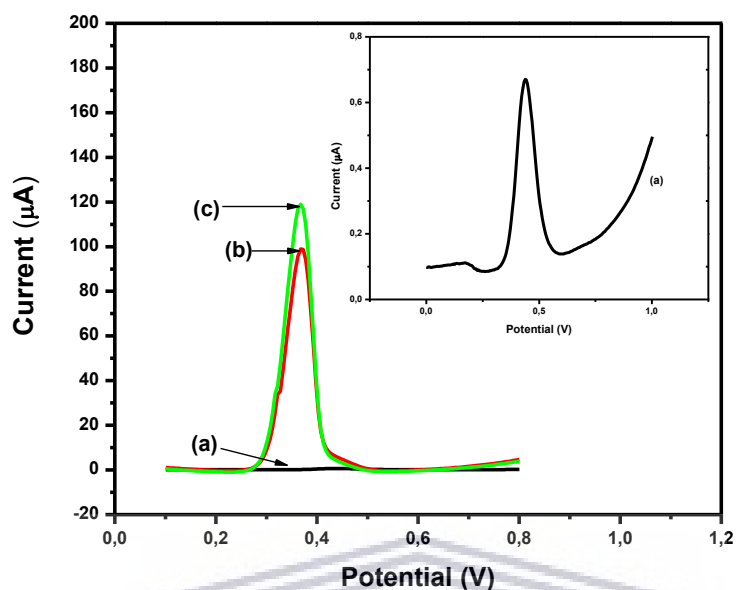


**Figure 5.4:** Differential pulse voltammograms of bare PGE (a), ERGO-PGE (b), and ERGO-Sb-PGE (c) in  $0.1 \text{ mol.L}^{-1}$  PBS at pH 7.0 containing  $10 \text{ } \mu\text{mol.L}^{-1}$  PC solution.

The peaks showed a shift in potential from 0.438 V for the bare PGE to 0.368 V for the modified electrodes, ERGO-PGE and ERGO-Sb-PGE. The shift in peak potential was noticeable with modification of the PGE, which was an indication of ease of electro-oxidation at modified PGE for PC. In Figure 5.4 (c), ERGO-Sb-PGE showed the greatest enhancement by a factor of 1.2 in peak current compared to that of ERGO-PGE in (b). The enhancement is attributed to the synergistic incorporation of graphene oxide and antimony nanoparticles, which facilitated the electro-oxidation of PC at ERGO-Sb-PGE.

#### **5.4. Effect of Deposition Time**

The optimum deposition time for which PGE can be modified with electrochemically graphene oxide-metal nanocomposite was investigated. Subsequently, the optimum deposition time for modification of PGE was to be used to investigate the greatest enhanced response that can be obtained for PC electro-oxidation. The optimization was achieved by varying the deposition time from 60 to 300 s, while the remaining instrumental parameters were kept constant according to

the CV conditions described earlier in the study. Figure 5.5 illustrates different deposition times along with the corresponding peak currents.

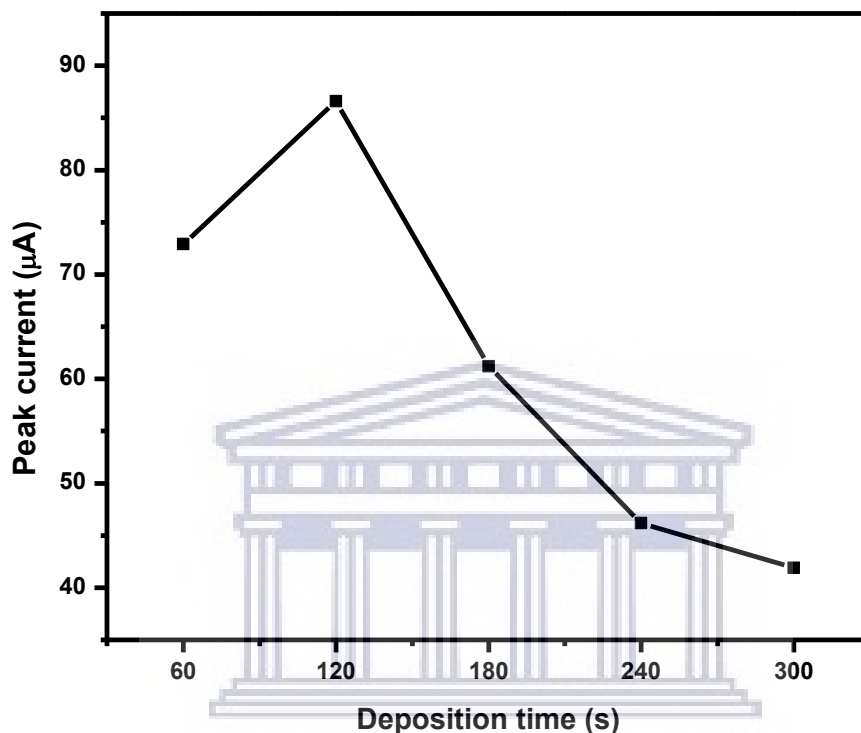


**Figure 5.5:** Influence of the deposition time on the surface modification of electrode for the electro-oxidation of PC at ERGO-Sb-PGE.

In Figure 5.5, PGE was modified with electrochemically reduced graphene oxide-antimony nanocomposite at an optimum deposition time of 120 s for which the greatest enhancement of the peak current response for PC electro-oxidation was only observed. At 60 s, this was the lowest deposition time for which the electrode may not have had sufficient material coverage resulting in poor current transferred on the electrode, hence the response obtained. The highest deposition time was 300 s, which showed the worst peak current response for the electro-oxidation of PC. This may be corresponding to the thick layer of material on the electrode surface, which may have been blocking the signal flowing through the electrode during electro-oxidation.

### 5.5. Effect of Cycles

The various coating cycles for the optimum modification of PGE with electrochemically reduced graphene oxide-antimony nanocomposite, with the remaining parameters kept constant was also investigated. This proceeded by investigating 1, 3, 5, 7, and 9 cycles with established deposition time of 120 s for improved enhancement of PC electro-oxidation. Figure 5.6 shows a depiction of plots at different number of cycles for modification at the electrode surface.

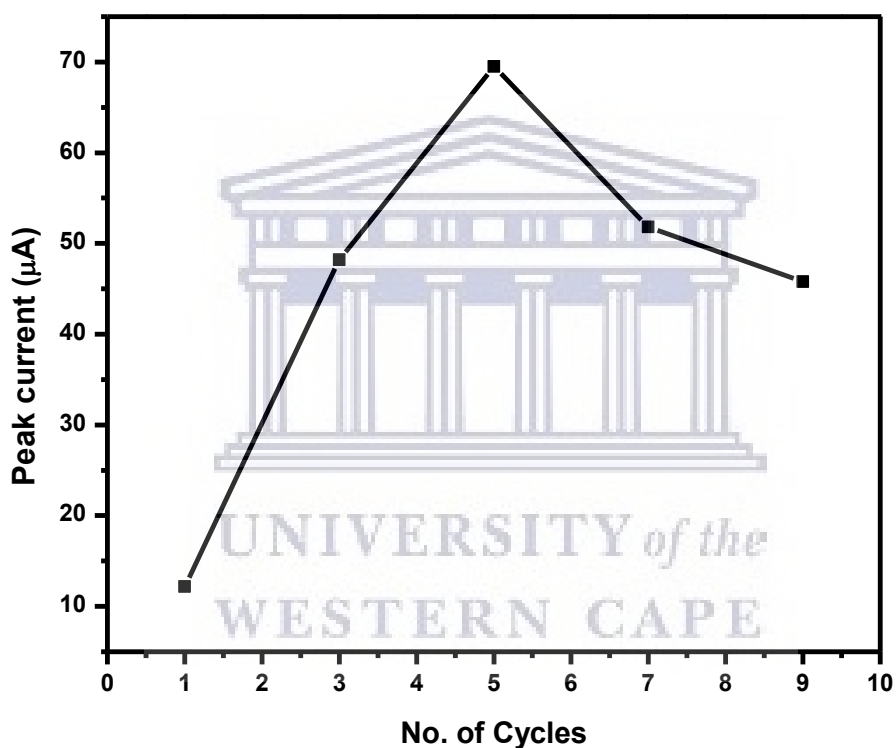


**Figure 5.6:** Influence of the number of cycles on the surface modification of electrode for the electro-oxidation of PC at ERGO-Sb-PGE.

The greatest enhancement for the electro-oxidation of PC at ERGO-Sb-PGE was observed at optimum of 5 cycles. At lower cycles the enhancement was not observed and as the number of cycles increased to greater than 5 cycles the enhancement subsided. This can be due to insufficient amount of graphene oxide-antimony material reduced on the electrode at lower cycles and the stretched deposition time used at higher number of cycles, and therefore the

reduction of the material on the electrode formed a thick film. Hence the current signal became blocked.

### 5.6. Effect of pH

The electro-oxidation of PC was studied in PBS as electrolyte at various solution pH values. The pH of the solution is an important parameter because it influences the variation in the acid-base dissociation of PC. In this way, it changes the electrochemical detection of PC by shifting the redox peak potential towards more positive or negative directions and also alters the redox peak currents [277]. Therefore, electro-oxidation of PC was investigated at various pH values in 0.1 mol.L<sup>-1</sup> PBS containing 10 μmol.L<sup>-1</sup> PC solutions. The pH values were varied from 5.0 to 9.0, which is where the oxidation product NAPQI shows stability and DPV scans are shown in Figure 5.7 (A) and the linear plots in (B).

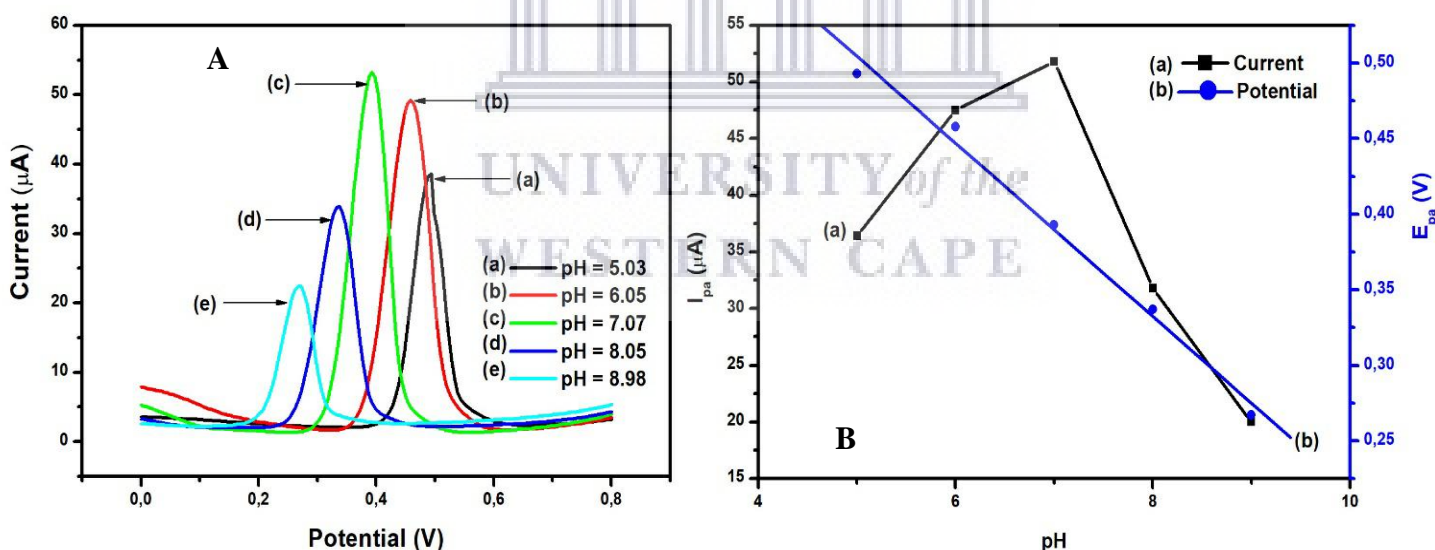
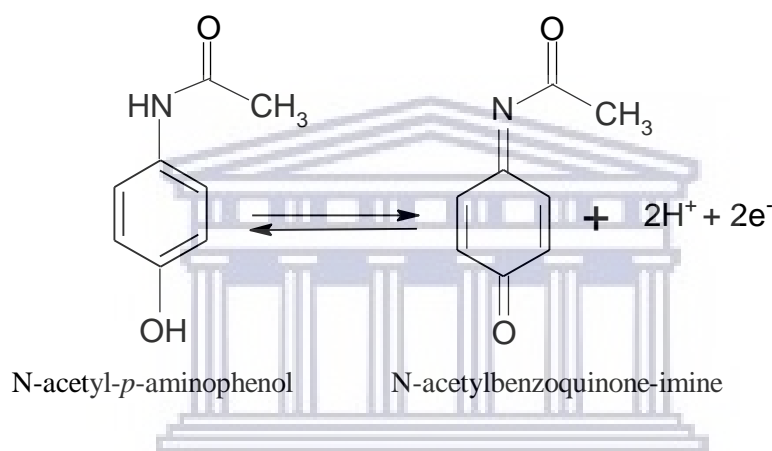


**Figure 5.7:** Effect of pH on the electro-oxidation of PC at ERGO-Sb-PGE; DPV responses (A) and linear plots of current and potential as a function of pH (B) in 0.1 mol.L<sup>-1</sup> PBS containing 10 μmol.L<sup>-1</sup> PC solution at various pH values.

In Figure 5.7 (B),  $E_{pa}$  (b) shifted negatively with increasing pH. The linear relationship between peak potentials and pH was given by regression equation;

$$E_{pa} \text{ (V)} = -0.0578 \text{ pH} + 0.7961 \text{ (R}^2 = 0.9861\text{)}$$

The slope of  $-0.0578 \text{ V/pH}$  obtained was found to be very close to the Nernstian slope of  $-0.059 \text{ V/pH}$  for the same number of electrons and protons involved in the process [277]. This was proven in the proposed oxidation mechanism of PC (Scheme 5.1) in which two electrons and two protons participated in the reaction;



**Scheme 5.1:** The proposed oxidation mechanism for PC (N-acetyl-*p*-aminophenol).

Peak currents changed with increasing pH as shown in (a) of Figure 5.7 (B). For the investigated pH range of 5.0 to 9.0, the slightly acidic end (5 and 6) produced lower oxidation peak currents. This is due to the hydrolysis of PC in which the participation of protons ( $\text{H}^+$ ) with the unstable oxidation product NAPQI leads to *p*-aminophenol being formed [35]. In the more alkaline pH region (8 and 9), the involvement of hydroxide ions ( $\text{OH}^-$ ) in the reaction results in the instability of NAPQI which in turn also yields lower peak currents [278]. The optimum pH at which PC undergone electro-oxidation was  $\text{pH} = 7$ , which is where the electrochemical behavior of PC is highly active [277] and this pH is very close to physiological conditions. Therefore,  $\text{pH} = 7$  was used for the rest of the experiments involved in the study.

### 5.7. Repeatability, Reproducibility, and Stability

A series of experiments were performed to investigate the repeatability, reproducibility, and stability of ERGO-Sb-PGE as a sensing platform for PC detection. The reproducibility of the voltammetric determinations on solid electrodes is highly dependent on the reproducibility of the electrode active surface, usually ensured by cleaning polishing/pretreatment of the surface before each recording. These are time-consuming steps which also may destroy the crystalline structure of the graphite. These drawbacks can be eliminated by using disposable graphite pencil leads which can be easily and rapidly replaced, shortening thus the analysis time. However, due to different interactions between an analyte and the common components of a graphite pencil lead, it is possible that electroactive species exhibit different voltammetric behavior on graphite pencil leads of the same hardness but are produced by various manufacturers [235].

Therefore, measurements proceeded on the same and multiple electrodes even though the PGEs were from the same manufacturer, over a period of 7 days. The 7-day period included experiments which were performed on the same day (intra-day), and the rest on different days separated by two days in between (inter-day). All electrodes used for these experiments were prepared on the first day of measurements. Five experiments were performed on the same electrode and also on five individual electrodes in  $10 \mu\text{mol.L}^{-1}$  PC in  $0.1 \text{ mol.L}^{-1}$  PBS (pH 7.03) over a potential range of 0.0 to 1.0 V vs. Ag/AgCl ( $3 \text{ mol.L}^{-1}$  KCl) for DPV conditions. The results are shown in [(A) - (D)] of Figure 5.8 (I) for experiments on the same ERGO-Sb-PGE and individual ones in (II).

A relative standard deviation (RSD) of 0.803 % for five measurements performed on the same ERGO-Sb-PGE on Day 1 was obtained from peak currents of DPVs in (A) to (C) of Figure 5.8 (I). Day 4 and Day 7 had RSDs of 0.98 % and 0.95 % for  $10 \mu\text{mol.L}^{-1}$  PC solution on the same ERGO-Sb-PGE, respectively. This confirmed good repeatability and reproducibility of ERGO-Sb-PGE for PC detection. However, the bar graph in (D) of Figure 5.8 (I) shows that the peak currents decreased by 44.01 % on Day 4 and further so by 63.13 % on Day 7.

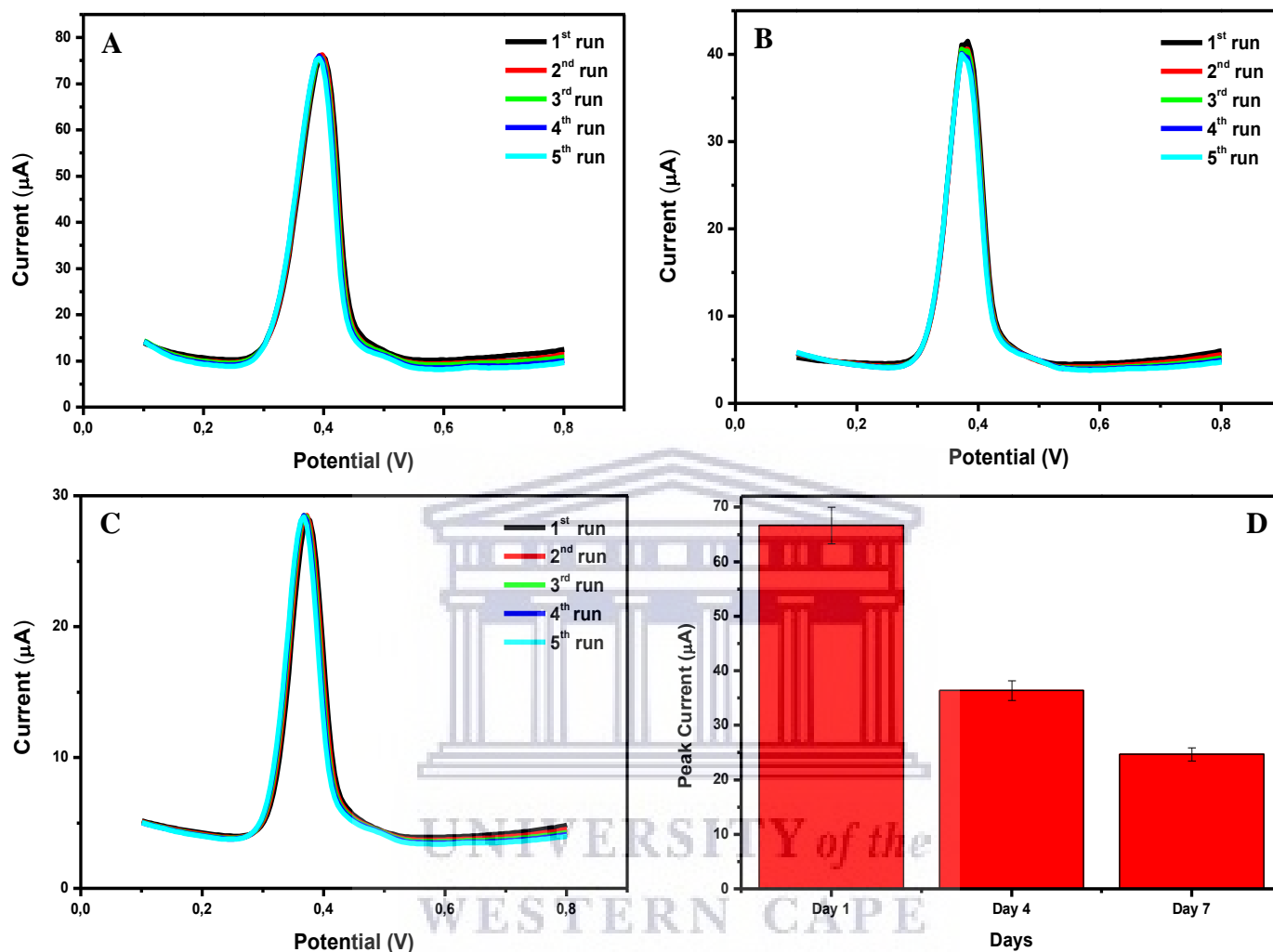


**Figure 5.8 (I):** DPV measurements obtained on the same ERGO-Sb-PGE in 10  $\mu\text{mol.L}^{-1}$  PC solution in 0.1  $\text{mol.L}^{-1}$  PBS for repeatability, reproducibility, and stability (A to C), and the accompanying bar graph showing peak currents over Day 1, Day 4, and Day 7 (D).

In Figure 5.8 (II) [(A to C)], the experiments performed on multiple ERGO-Sb-PGE showed RSD of 2.003 %, 2.93 %, and 4.19 % for 10  $\mu\text{mol.L}^{-1}$  PC solution on Day 1, 4, and 7 respectively. These were relatively comparable with data obtained for PC at other similar electrodes [35, 278], which also indicated good repeatability and reproducibility. Similarly, for

same-ERGO-Sb-PGE experiments, the stabilities for Day 4 and Day 7 decreased by 77.14 % and 79.62 %, respectively as shown by the peak currents in (D). These indicated that the stability could be improved. The electrodes may have been affected by the storage conditions as well as the duration of being stored.

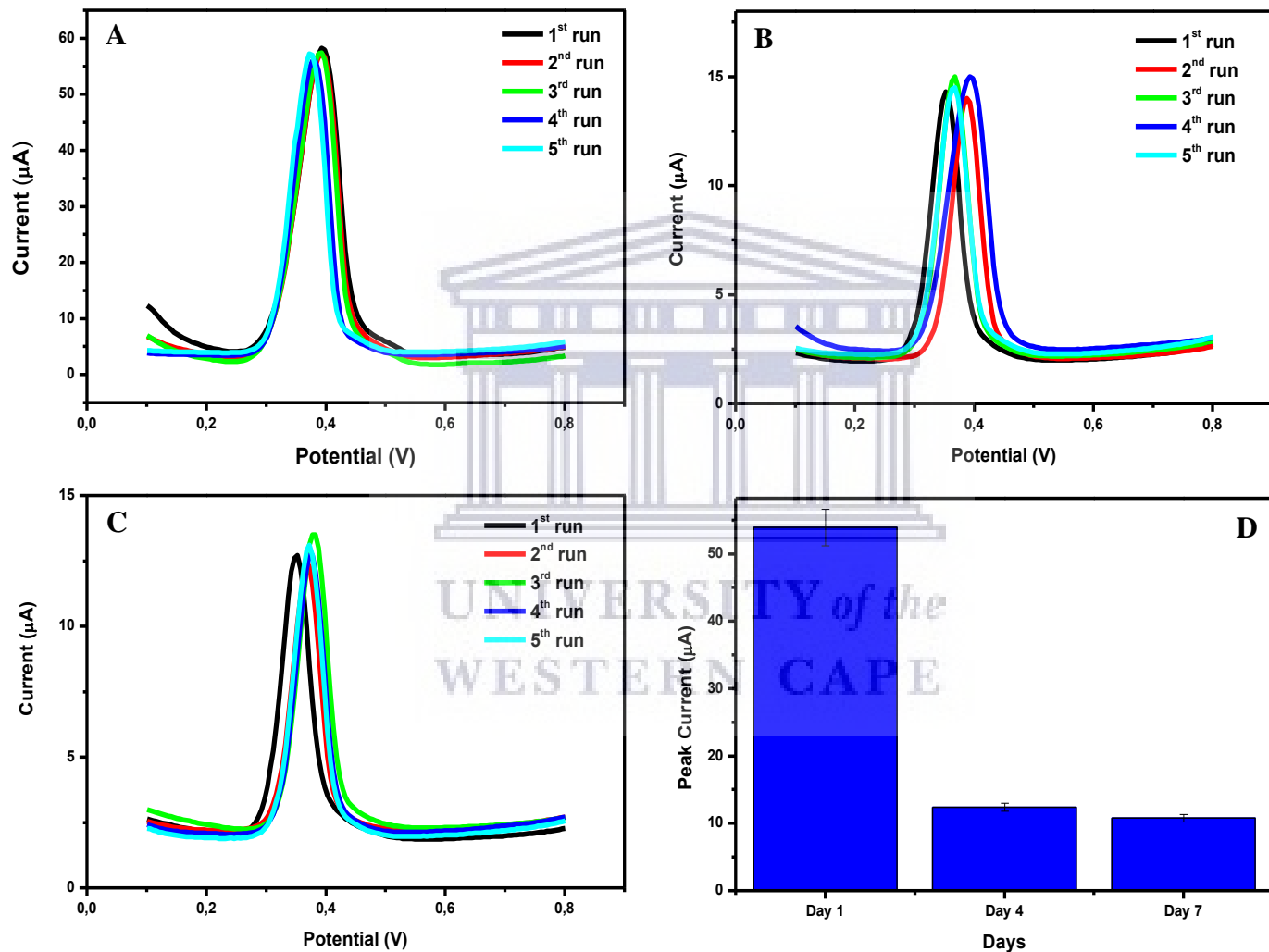


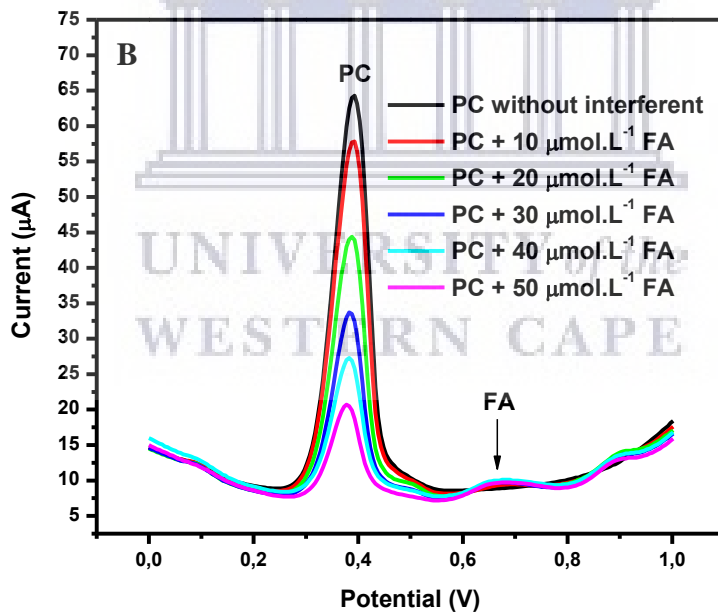
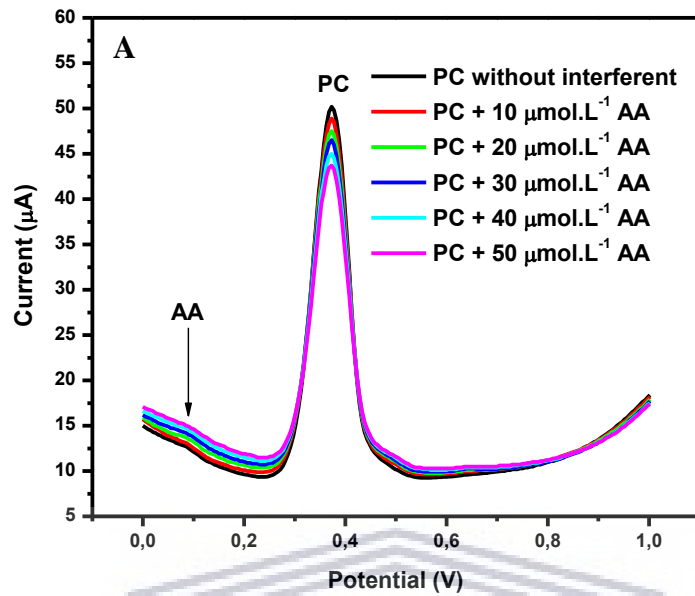
**Figure 5.8 (II):** DPV measurements obtained on multiple ERGO-Sb-PGEs in 10  $\mu\text{mol.L}^{-1}$  PC solution in 0.1  $\text{mol.L}^{-1}$  PBS for repeatability, reproducibility, and stability (A to C), and the accompanying bar graph showing peak current over Day 1, Day 4, and Day 7 (D).

### 5.8. Interference Studies

The selectivity of ERGO-Sb-PGE towards PC was investigated in the presence of ascorbic acid (AA), folic acid (FA), and caffeine (CAFF). It has been reported that in therapeutic use, PC has often been found to be in association with AA and/or other pharmacologically and biologically active compounds [279]. Caffeine also has been found to be associated with PC in many commercial formulations because CAFF increases the analgesic strength of PC [280]. Paracetamol along with other non-steroidal anti-inflammatory drugs such as ibuprofen and aspirin are able to inhibit the FA taken up by the human body, and also increase the necessity for FA [281].

Therefore, DPV measurements proceeded in solution containing  $10 \mu\text{mol.L}^{-1}$  PC with varying concentrations of interferent ( $10 - 50 \mu\text{mol.L}^{-1}$ ) in the potential range 0.0 to 1.0 V and the results are shown in Figure 5.9 (A) to (C). For PC and AA in solution [Figure 5.9 (A)], the oxidation peak potentials were found at 0.383 V and 0.0906 V respectively. The oxidation peak current for PC in the presence of AA was considerable as indicated by the RSD which was found to be 6.08 % ( $n = 3$ ; measurements of peak currents) as displayed in Table 5.1. Therefore, due to this consideration of Section 5.7, this indicated there was slight involvement of interference between the two compounds.

However, the PC oxidation peak current was greatly affected by the presence of the remaining compounds in their respective solutions; FA and CAFF as depicted in Figure 5.9 (B) and (C). In Figure 5.9 (B), oxidation peak potentials were 0.387 V for PC and 0.665 V attributed to FA, and (C) shows only that of PC at 0.378 V as the peak potential for CAFF lies at 1.30 V outside the investigated potential range. Relative standard deviation (RSD) for FA and CAFF were at 29.3 % and 26.1 %, respectively. Such occurrence may be due to electrode complexity and that FA and CAFF or their respective oxidation products may be interacting with the electrode surface.



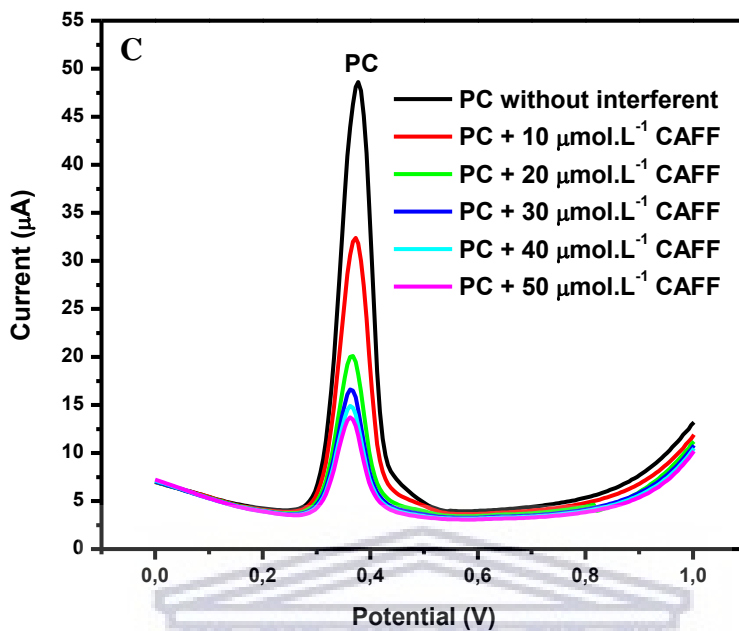


**Figure 5.9:** DPV results showing electro-oxidation of  $10 \mu\text{mol.L}^{-1}$  PC in  $0.1 \text{ mol.L}^{-1}$  PBS (pH = 7.03) at ERGO-Sb-PGE in the presence of interferences; (A) AA, FA (B), and CAFF (C) at different concentrations (10, 20, 30, 40, and  $50 \mu\text{mol.L}^{-1}$  of interferent).

**Table 5.1:** The results below depict the effect of interferences namely; AA, FA, and CAFF on the oxidation peak current of PC at different concentrations, and their RSDs (%).

Interferent	$C_i$ ( $\mu\text{mol.L}^{-1}$ )	PC peak current (A)	RSD (%)
AA	10 - 50	$4.06 \times 10^{-5} \pm 2.47 \times 10^{-6}$	6.08
FA	10 - 50	$5.02 \times 10^{-5} \pm 1.47 \times 10^{-5}$	29.3
CAFF	10 - 50	$2.9 \times 10^{-5} \pm 7.56 \times 10^{-6}$	26.1

$C_i$ : Concentration of interferent

Average  $\pm$  STDEV

RSD% of peak currents (n = 3)

### 5.9. Limit of Detection

The analytical performance of ERGO-Sb-PGE was investigated to establish a linear concentration range and a limit of detection. These were studied under optimized parameters for which oxidation peak current is proportional to the concentration of PC in a range 0.1 - 10  $\mu\text{mol.L}^{-1}$ . Figure 5.10 (A) shows the resulting calibration curve and the accompanying calibration linear plot in (B).

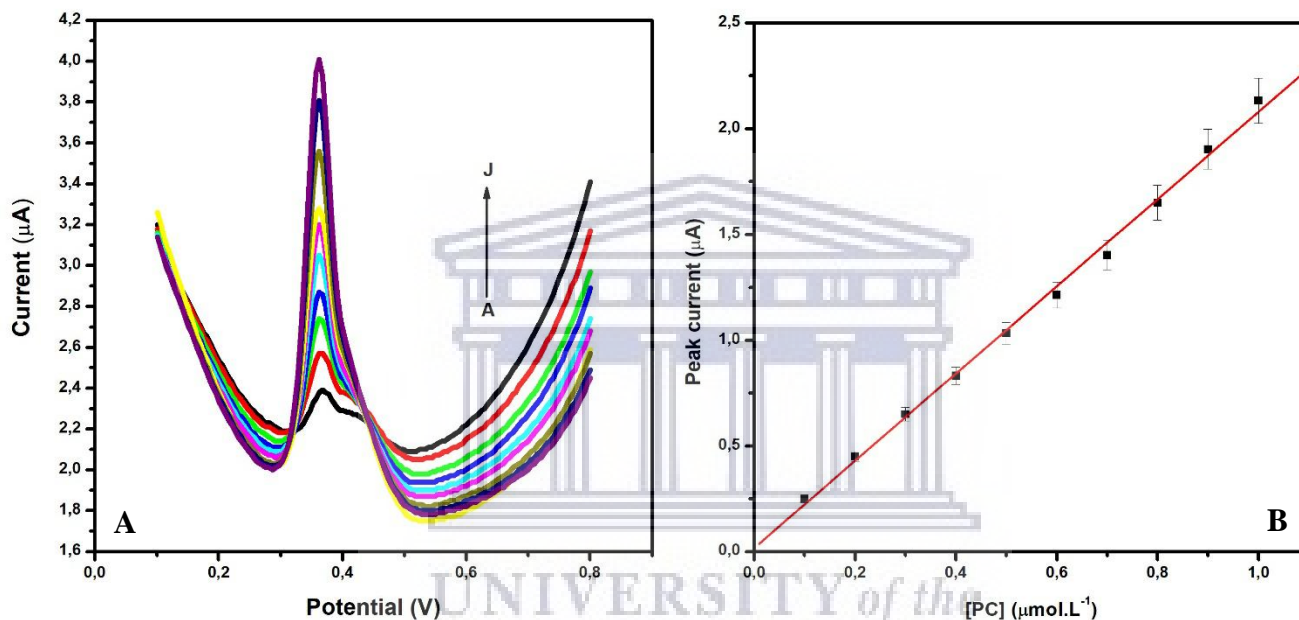


**Figure 5.10:** DPVs obtained at ERGO-Sb-PGE in 0.1  $\text{mol.L}^{-1}$  PBS (pH 7.01) containing concentrations of PC (A - J: 0.1, 0.2, 0.3, 0.4, 0.5, 0.6, 0.7, 0.8, 0.9, and 1.0  $\mu\text{mol.L}^{-1}$ ) in (A) and the corresponding calibration plots in (B).

The calibration curve shown in Figure 5.10 (A) was constructed from average values of data collected from three experiments conducted for each developed ERGO-Sb-PGE. Figure 5.10 (B) shows a calibration linear plot of peak current vs. concentration of PC at ERGO-Sb-PGE for different PC concentrations, the linear dynamic range was observed in the region 0.1 – 1.0  $\mu\text{mol.L}^{-1}$  PC solution. The linear regression equation for the established region at ERGO-Sb-PGE was as follows;

$$I_{pa} (\text{A}) = 2.08 \times 10^{-6} [\text{PC}] (\mu\text{mol.L}^{-1}) + 1.56 \times 10^{-8} (R^2 = 0.998)$$

The limit of detection for PC at ERGO-Sb-PGE was determined using the slope from the linear plot in the following equation;

$$\text{Detection limit} = \frac{3\sigma}{m} \quad (5.4)$$

where  $\sigma$  is the standard deviation obtained from 10 blanks and  $m$  is the slope from the calibration linear plot. The average detection limit was determined to be 0.57 nmol.L<sup>-1</sup> for PC at ERGO-Sb-PGE. The data collected from experiments conducted is summarized in Table 5.2.

**Table 5.2:** Calibration data from the experiments conducted for analytical performance of PC at ERGO-Sb-PGE.

Experiment no.	Linear range (μmol.L <sup>-1</sup> )	Correlation coefficient (R <sup>2</sup> )	LOD (μmol.L <sup>-1</sup> )
1	0.1 – 1.0	0.9963	0.00058
2	0.1 – 1.0	0.9933	0.00054
3	0.1 – 1.0	0.997	0.00059
Average	0.1 – 1.0	0.998	0.00057

Similarly, a modified glassy carbon electrode was developed based on the synergistic combination of RGO and SbNPs, which was used for determination of estriol in environmental samples. The LOD found for this nanocomposite was 0.5 nmol.L<sup>-1</sup> estriol in the linear range of 0.2 to 1.4 μmol.L<sup>-1</sup> [265]. This shows that ERGO-Sb-PGE was comparable with other carbon electrodes with similar modification for similar electroactive compounds. Other comparable results from various previous literatures for the detection of PC at similar electrode surface are also summarized in Table 5.3 with appropriate references.

**Table 5.3:** Comparable results of calculated detection limits summarized from previous studies for PC at similarly modified electrodes.

Modified electrode	Detection method	pH	Linear range ( $\mu\text{mol.L}^{-1}$ )	LOD ( $\text{mol.L}^{-1}$ )	References
BF/PGE	DPV	7.4	0.05-100	$2.4 \times 10^{-9}$	[35]
Graphene/chitosan/GCE	DPV	6.3	0.2-550	$5.7 \times 10^{-8}$	[35, 282]
Graphene/GCE	CV	9.3	0.1-20	$3.2 \times 10^{-8}$	[35, 283]
BDDE	DPV	4.3	0.83-50	$4.9 \times 10^{-7}$	[35, 284]
MWCNTc/BPPGE	ATSDPV	7.5	0.01 – 2.0	$1.0 \times 10^{-8}$	[35, 285]
PANI/MWCNT/GCE	SWV	5.5	1 – 100	$2.5 \times 10^{-7}$	[35, 286]
ETPG	ATSDPV	6.0	0.05 – 2.5	$2.5 \times 10^{-9}$	[272, 287]
ERGO-Sb-PGE	AdsDPV	7.01	0.1-1.0	$5.7 \times 10^{-10}$	This work
ERGO-Au-PGE	AdsDPV	7.01	0.5 – 5.0	$1.10 \times 10^{-8}$	This work

#### 5.10. Analytical Application of ERGO-Sb-PGE for PC

Quantification of PC in a commercial tablet was investigated at ERGO-Sb-PGE using DPV. The developed ERGO-Sb-PGE was applied in a real sample for analytical performance. Paracetamol samples were prepared by dissolving a tablet containing 500 mg PC in  $0.1 \text{ mol.L}^{-1}$  PBS (pH = 7.01) and the recovery experiments were conducted according to DPV conditions previously described as well. Experiments were performed in quintet and the sample was recovered by use of standard addition and calibration curve methods. The resultant DPV measurements are shown in Figure 5.11 (A), and the corresponding standard addition plots in (B).

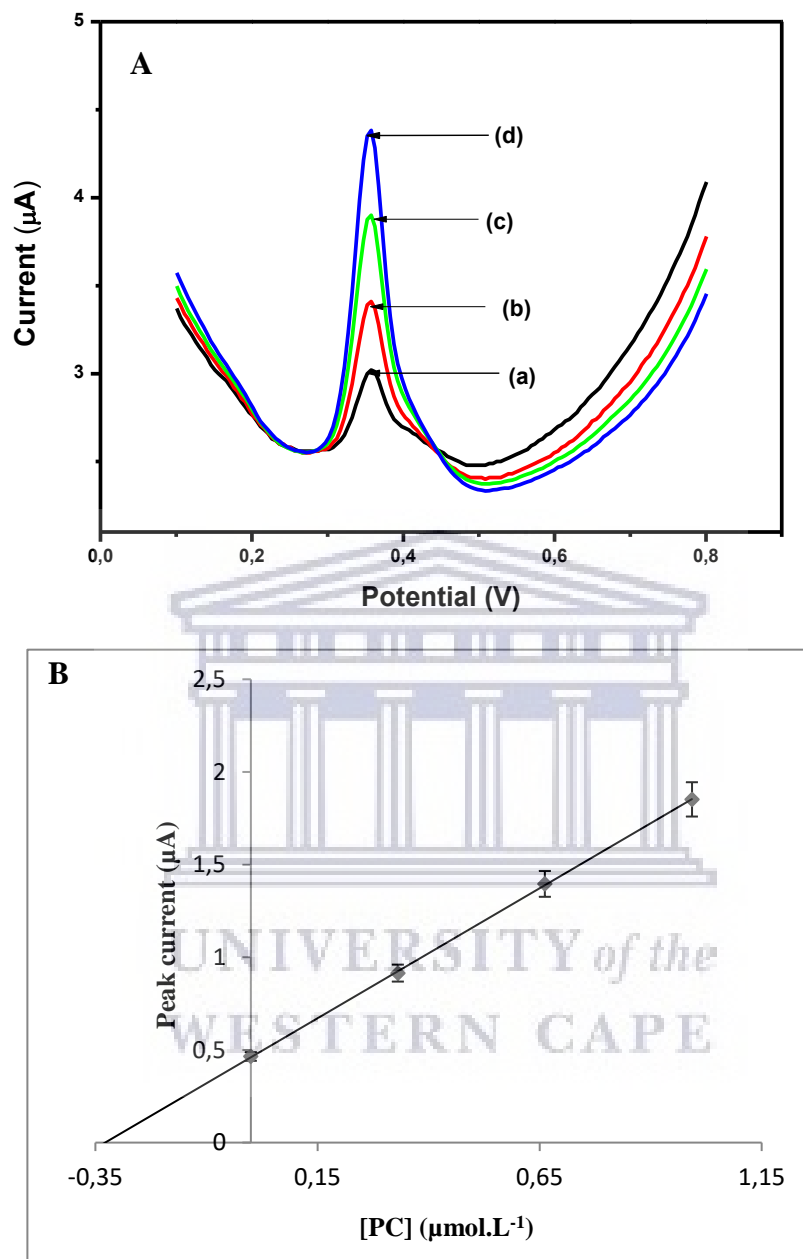


**Figure 5.11:** DPV measurements for the recovery of PC at ERGO-Sb-PGE with standard additions at different concentrations of sample (a); sample +  $0.331 \mu\text{mol.L}^{-1}$  (b), sample +  $0.662 \mu\text{mol.L}^{-1}$  (c), and sample +  $0.993 \mu\text{mol.L}^{-1}$  (d) PC solution in (A), and linear plot of the average standards added in (B).

In the five determinations performed, Figure 5.11 (B) shows a linear plot with average standard additions and the corresponding results in Table 5.4 showed recovery of average  $\pm$  standard

deviation of  $0.332 \pm 0.0033 \mu\text{mol.L}^{-1}$  PC at ERGO-Sb-PGE. For standards added of 0.331, 0.662, and  $0.993 \mu\text{mol.L}^{-1}$  PC, the recoveries were between 98.9 % and 100.9 % PC in a commercial tablet which were accepted values for the considered electrode. Additionally, the calibration curve in Figure 5.10 (B) was used to recover PC concentrations in solution. The PC solution was diluted to  $0.1 \mu\text{mol.L}^{-1}$ , which was the most consistent concentration across all the calibration curves considered. The recoveries were between 98.3 % and 101.6 % for average  $\pm$  standard deviation of  $0.09969 \pm 0.0013 \mu\text{mol.L}^{-1}$  PC at ERGO-Sb-PGE.

**Table 5.4:** Results of the recovered PC from a commercial tablet containing 500 mg PC at ERGO-Sb-PGE using standard addition and calibration curve methods.

Method	Recovered [PC] ( $\mu\text{mol.L}^{-1}$ )	Recovery (%)
Standard addition (0.331 $\mu\text{mol.L}^{-1}$ PC)	0.3336	100.9
	0.3344	100.9
	0.3338	100.9
	0.329	99.3
	0.327	98.9
Average $\pm$ STDEV	$0.332 \pm 0.0033$	
Calibration curve (0.1 $\mu\text{mol.L}^{-1}$ PC)	0.1016	101.6
	0.1001	100.1
	0.09971	99.7
	0.09875	98.8
	0.09827	98.3
Average $\pm$ STDEV	$0.09969 \pm 0.0013$	

### 5.11. Conclusion

Incorporation of GO and intended SbNPs was implemented onto the PGE by electrodeposition to accomplish ERGO-Sb-PGE sensor. The sensor was characterized electrochemically and thereafter used for electrochemical determination of PC by use of adsorptive stripping differential pulse voltammetry. The electrochemical response was optimized to obtain maximum

enhancement of PC. Limit of detection was found to be  $0.57 \text{ nmol.L}^{-1}$  and this was comparable with previous similar electrodes. Standard addition and calibration curve methods were used in quantification of PC in pharmaceutical commercial tablet, the recovery was between 98.3 % and 101.6 % ( $n = 5$ ). These results were found to be satisfactory for the study.



## CHAPTER SIX:

### Electrochemical Oxidation of Paracetamol at Electrochemically Reduced Graphene Oxide-Gold Nanocomposite Modified Pencil Graphite Electrode

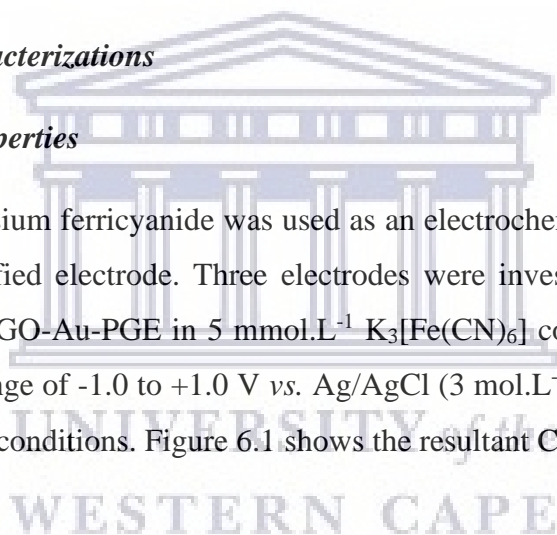
#### 6.1. Introduction

The current chapter is dedicated to the description of the electro-oxidation of PC at ERGO-Au-PGE and experimental results that accompanied the investigation thereof. The results include the electrochemical characterization of electrode and subsequently the electro-oxidation of PC at the surface. The electrochemical response obtained was used towards application in a pharmaceutical tablet containing PC.

#### 6.2. Electrochemical Characterizations

##### 6.2.1. Electrochemical Properties

As previously stated, potassium ferricyanide was used as an electrochemical probe to investigate the properties of the modified electrode. Three electrodes were investigated namely; the bare PGE, ERGO-PGE, and ERGO-Au-PGE in  $5 \text{ mmol.L}^{-1} \text{ K}_3[\text{Fe}(\text{CN})_6]$  containing  $0.1 \text{ mol.L}^{-1} \text{ KCl}$  solution, in the potential range of  $-1.0$  to  $+1.0 \text{ V vs. Ag/AgCl}$  ( $3 \text{ mol.L}^{-1} \text{ KCl}$ ) using a scan rate of  $50 \text{ mV.s}^{-1}$  according to CV conditions. Figure 6.1 shows the resultant CV scans of experiments.



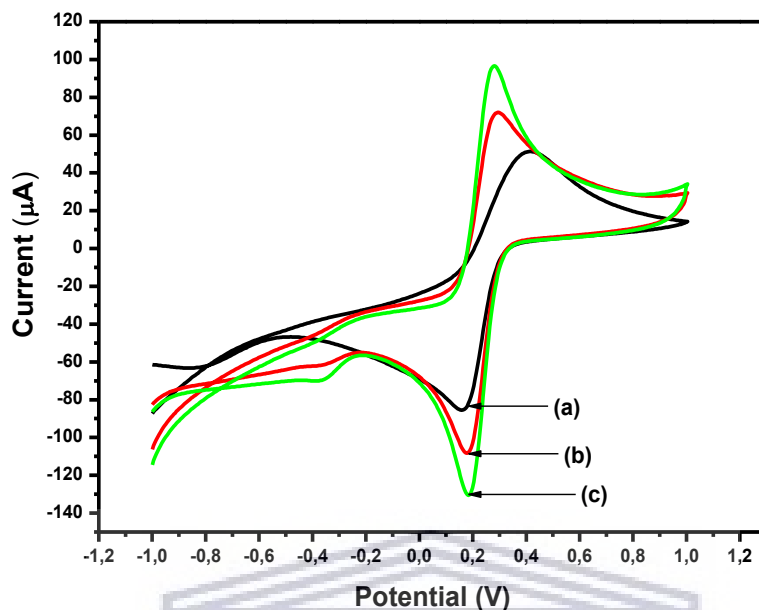


**Figure 6.1:** Cyclic voltammograms of  $5 \text{ mmol.L}^{-1} [\text{Fe}(\text{CN})_6]^{3-/4-}$  containing  $0.1 \text{ mol.L}^{-1} \text{ KCl}$  solution at (a) bare PGE, (b) ERGO-PGE, and ERGO-Au-PGE (c) at a scan rate of  $50 \text{ mV.s}^{-1}$ .

In the CVs shown in Figure 6.1, the bare PGE has  $\Delta E_p = 258 \text{ mV}$ , ERGO-PGE has  $\Delta E_p = 116 \text{ mV}$ , and for ERGO-Au-PGE it was found to be  $\Delta E_p = 97 \text{ mV}$ , which indicated reversibility for the electron transfer redox process. The oxidation peak current ( $I_{pa}$ ) was observed at  $7.20 \times 10^{-5} \text{ A}$  for ERGO-PGE and ERGO-Au-PGE had an assigned value of  $9.44 \times 10^{-5} \text{ A}$ , and hence an enhancement by a factor of 1.3. An enhancement factor of 1.2 was observed for the reduction peak current ( $I_{pc}$ ) which corresponded to  $-1.07 \times 10^{-4} \text{ A}$  and  $-1.30 \times 10^{-4} \text{ A}$  of ERGO-PGE and ERGO-Au-PGE respectively (ERGO-PGE;  $I_{pc}/I_{pa} = 1.5$  and ERGO-Au-PGE;  $I_{pc}/I_{pa} = 1.3$ ). The value found for the  $\Delta E_p$  of ERGO-Au-PGE indicate the ability of the electrode to increase the electron transfer of  $[\text{Fe}(\text{CN})_6]^{3-/4-}$ , which was expected to be facilitated by the electrocatalytic effect of AuNPs that was also responsible for the enhanced current response at the modified electrode surface, and the increased surface area due to ERGO.

### 6.2.2. Electrochemical Impedance Spectroscopy

Electrochemical impedimetric analysis was studied for bare PGE, ERGO-PGE, and ERGO-Au-PGE in 5 mmol.L<sup>-1</sup> in [Fe(CN)<sub>6</sub>]<sup>3-/4-</sup> in 0.1 mol.L<sup>-1</sup> KCl solution. Figure 6.2 demonstrates the Nyquist plots of the mentioned electrodes. As per expectation, the plots display well-defined semi-circle for bare PGE, and the modified electrodes show adequate semi-circles.

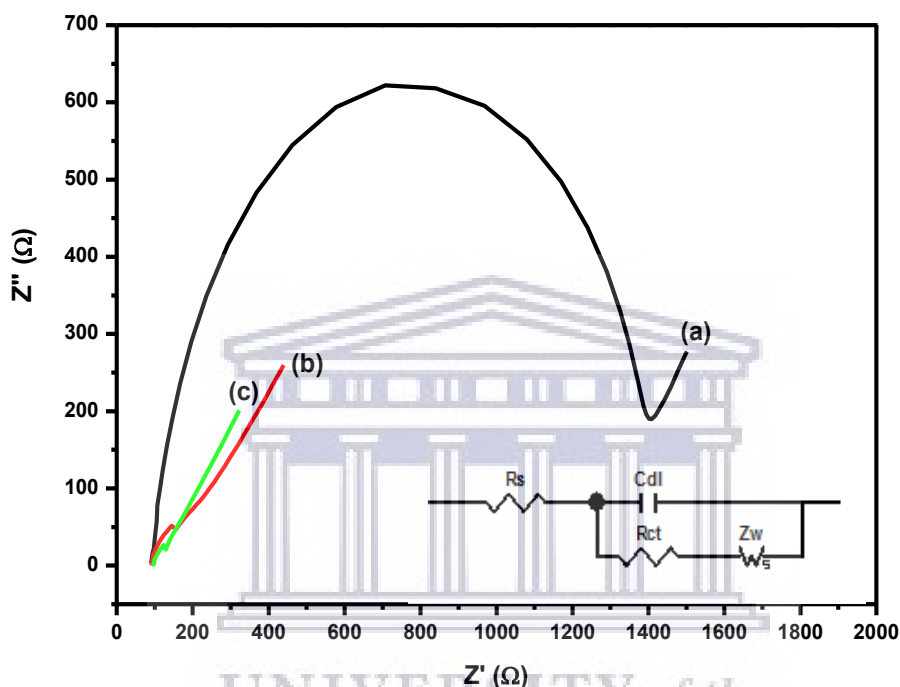


**Figure 6.2:** Nyquist plot of [Fe(CN)<sub>6</sub>]<sup>3-/4-</sup> (5 mmol.L<sup>-1</sup>) containing 0.1 mol.L<sup>-1</sup> KCl at bare PGE (a), ERGO-PGE (b), and ERGO-Au-PGE (c). Insert: Equivalent circuit fitting.

The fitting from the equivalent circuit allowed for extraction of parameters for the obtained Nyquist plots in Figure 6.2 (insert). Bare PGE (a) had  $R_{ct} = 1412 \Omega$ , for which there was an observed decrease as modification improved. A charge transfer resistance of 200.6 Ω corresponded to ERGO-PGE (b), and 126.6 Ω was observed for ERGO-Au-PGE (c). Therefore, it can be deduced from the observations that the electron transfer of the active species were most improved at the most conductive electrode for which in this instance was ERGO-Au-PGE. These results were consistent with electrochemical characterizations performed in Section 5.2.1.

### 6.2.3. Effect of Scan Rate on [Fe(CN)<sub>6</sub>]<sup>3-/4-</sup> Redox Couple at ERGO-Au-PGE

The demonstration of various scan rates of cyclic voltammograms and their effect using bare PGE, ERGO-PGE, and ERGO-Au-PGE were investigated in 5 mmol.L<sup>-1</sup> K<sub>3</sub>[Fe(CN)<sub>6</sub>] in 0.1 mol.L<sup>-1</sup> KCl solution over scan rate range of 10 – 100 mV.s<sup>-1</sup>. Figure 6.3 (I) – (III) [(A) – (D)] displays the effect of scan rate as indicated by the cyclic voltammograms of each of the selected electrodes.

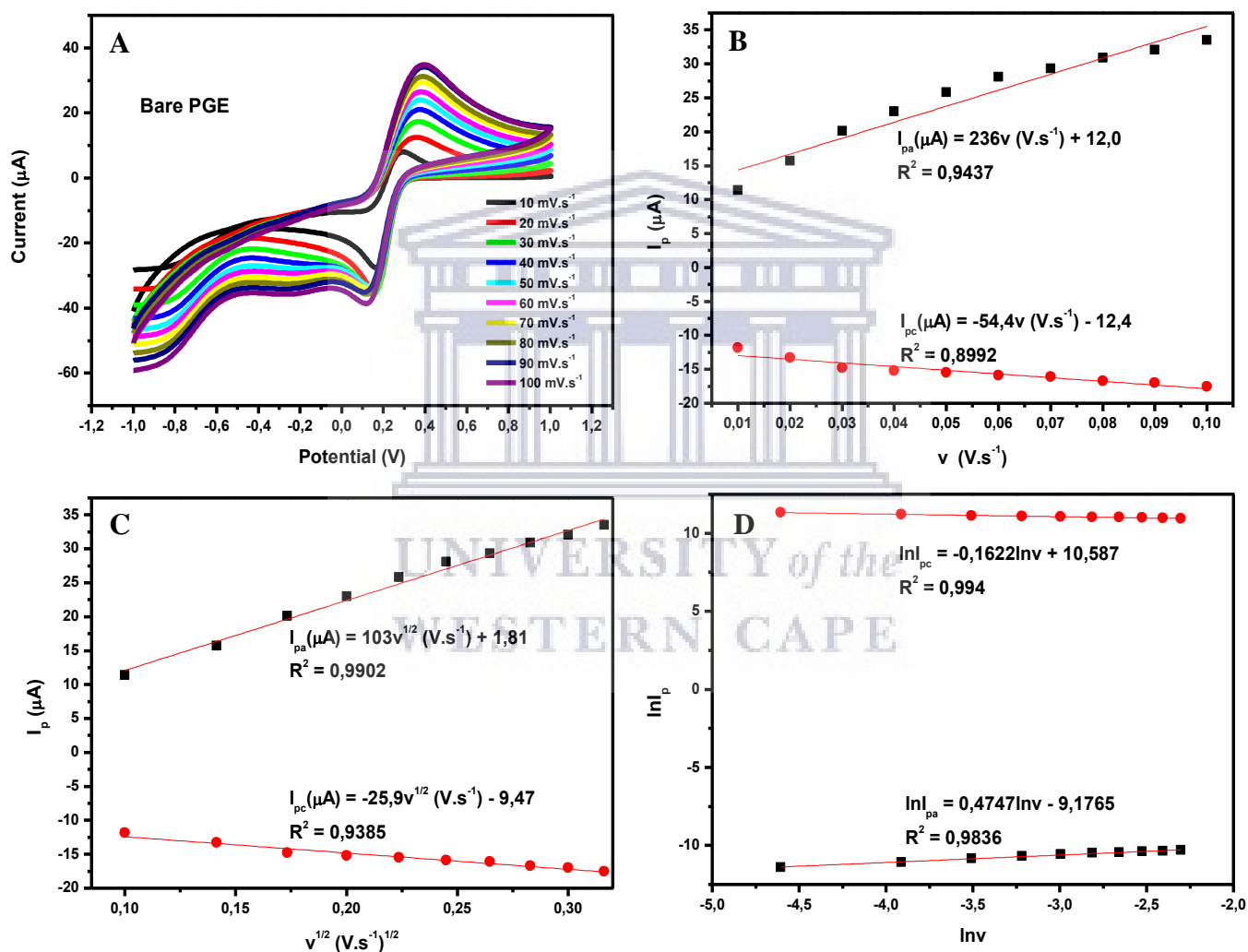


**Figure 6.3 (I):** Cyclic voltammograms of bare PGE in 5 mmol.L<sup>-1</sup> [Fe(CN)<sub>6</sub>]<sup>3-/4-</sup> in 0.1 mol.L<sup>-1</sup> KCl solution over a scan rate range of 10 – 100 mV.s<sup>-1</sup> (A). Accompanying linear plots of scan

rate and square root of scan rate with peak currents displayed in (B) and (C), respectively. The plot of  $\ln I_p$  and  $\ln v$  is shown in (D).

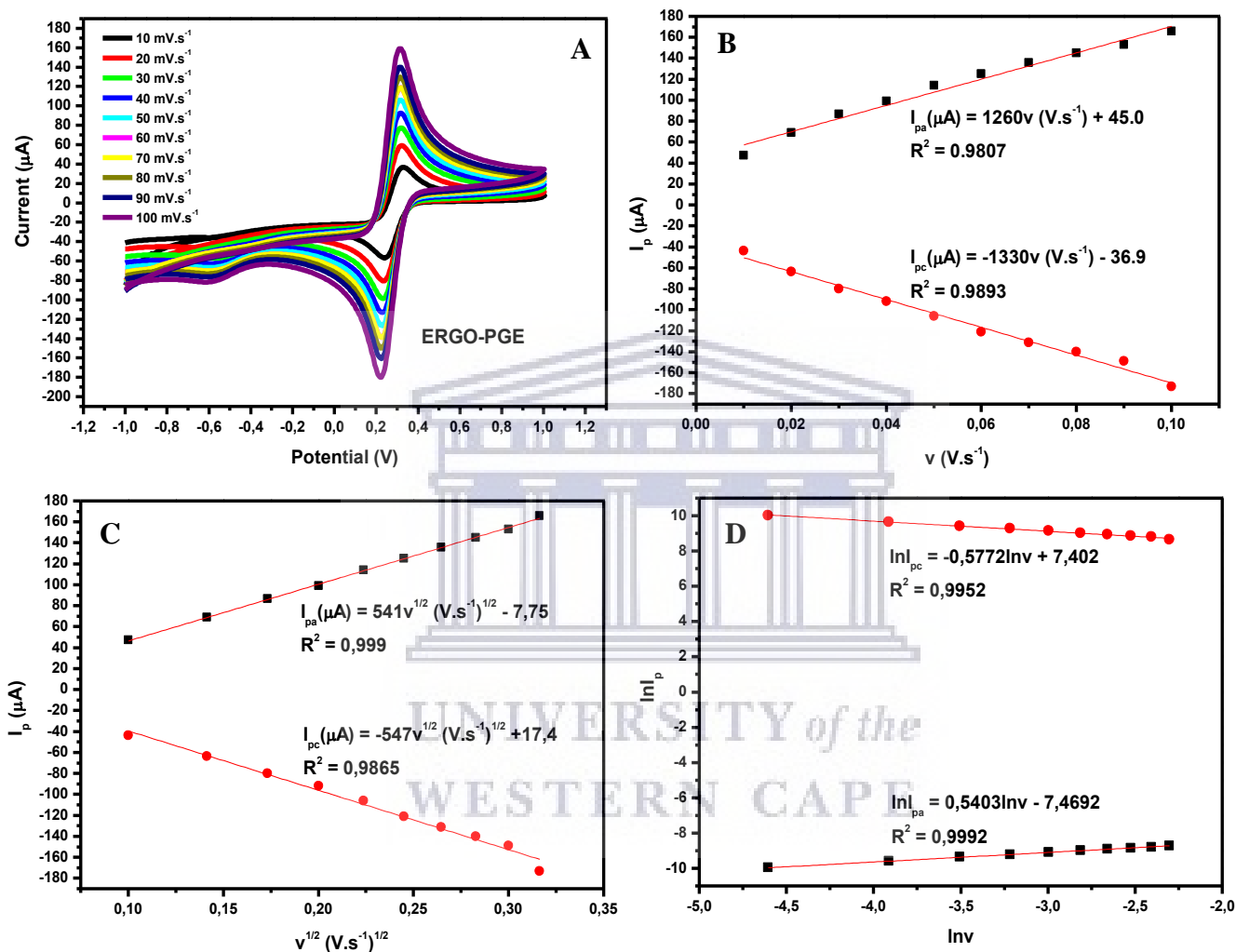


**Figure 6.3 (II):** Cyclic voltammograms of ERGO-PGE in 5 mmol.L<sup>-1</sup> [Fe(CN)<sub>6</sub>]<sup>3-/4-</sup> in 0.1 mol.L<sup>-1</sup> KCl solution over a scan rate range of 10 – 100 mV.s<sup>-1</sup> (A). Accompanying linear plots of scan rate and square root of scan rate with peak currents displayed in (B) and (C), respectively. The plot of  $\ln I_p$  and  $\ln v$  is shown in (D).

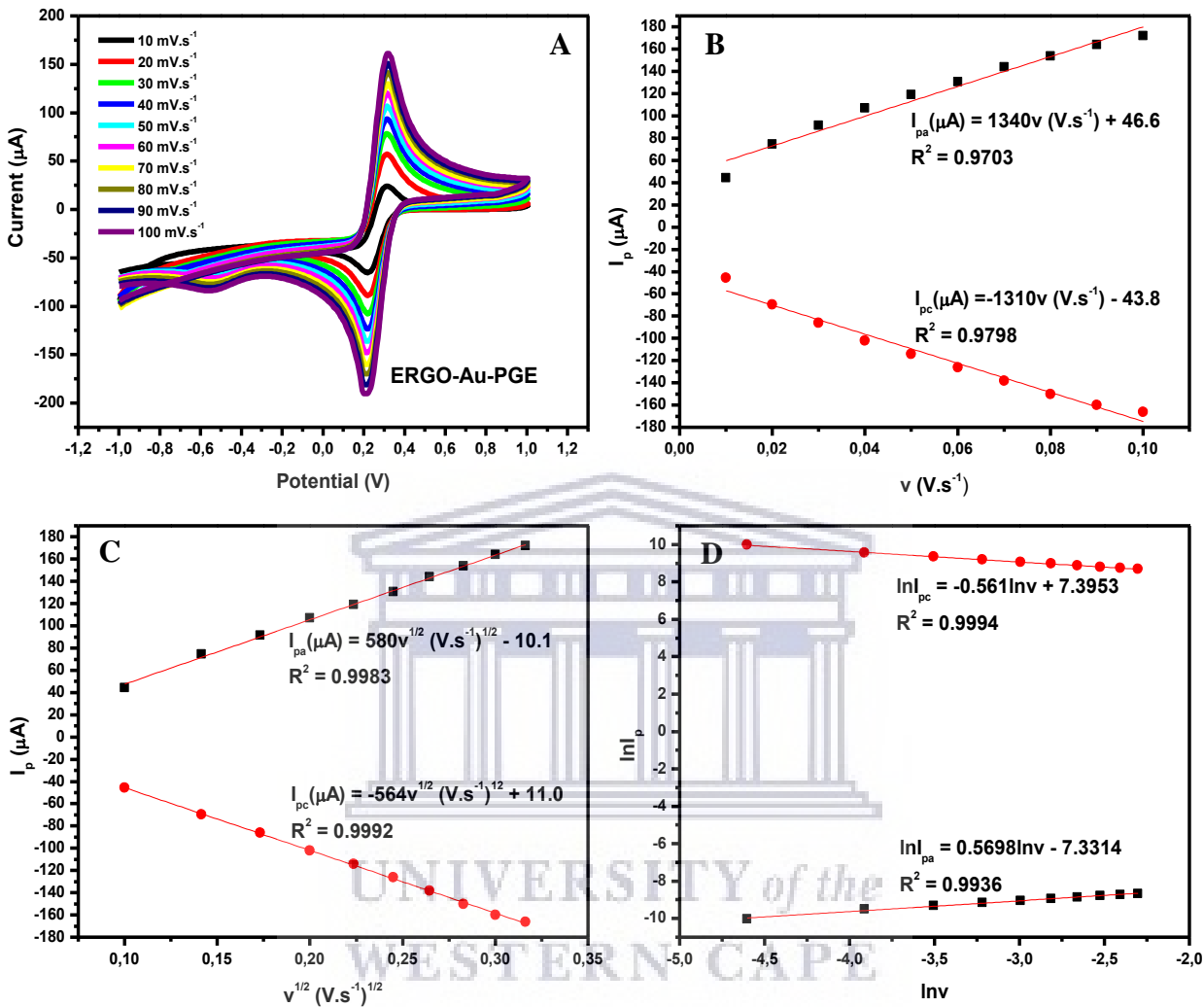


**Figure 6.3 (III):** Cyclic voltammograms of ERGO-Au-PGE in  $5 \text{ mmol.L}^{-1} [\text{Fe}(\text{CN})_6]^{3-/4-}$  in  $0.1 \text{ mol.L}^{-1} \text{ KCl}$  solution over a scan rate range of  $10 - 100 \text{ mV.s}^{-1}$  (A). Accompanying linear plots of scan rate and square root of scan rate with peak currents displayed in (B) and (C), respectively. The plot of  $\ln I_p$  and  $\ln v$  is shown in (D).

Similar trends found in Figure 5.3 (I) – (III) [(A) – (D)] were also observed for bare PGE, ERGO-PGE, and ERGO-Au-PGE in Figure 6.3 (I) – (III) [(A) – (D)]. In Figure 6.3 [(I) – (III)] (A), the cyclic voltammograms showed increasing oxidation and reduction peak currents with

increasing scan rates. The linear plots of scan rate and peak currents are shown in Figure 6.3 [(I) – (III)] (B) and regression equations are as follows;

Bare PGE:

$$I_{pa} \text{ (A)} = 2.20 \times 10^{-4} \nu \text{ (V.s}^{-1}\text{)} + 1.15 \times 10^{-5} \text{ (R}^2 = 0.9607\text{)}$$

$$I_{pc} \text{ (A)} = -8.36 \times 10^{-5} \nu \text{ (V.s}^{-1}\text{)} - 1.02 \times 10^{-5} \text{ (R}^2 = 0.9963\text{)}$$

ERGO-PGE:

$$I_{pa} \text{ (A)} = 1.26 \times 10^{-3} \nu \text{ (V.s}^{-1}\text{)} + 4.5 \times 10^{-5} \text{ (R}^2 = 0.9807\text{)}$$

$$I_{pc} \text{ (A)} = -1.33 \times 10^{-3} \nu \text{ (V.s}^{-1}\text{)} - 3.69 \times 10^{-5} \text{ (R}^2 = 0.9893\text{)}$$

ERGO-Au-PGE:

$$I_{pa} \text{ (A)} = 1.34 \times 10^{-3} \nu \text{ (V.s}^{-1}\text{)} + 4.66 \times 10^{-5} \text{ (R}^2 = 0.9703\text{)}$$

$$I_{pc} \text{ (A)} = -1.31 \times 10^{-3} \nu \text{ (V.s}^{-1}\text{)} - 4.38 \times 10^{-5} \text{ (R}^2 = 0.9798\text{)}$$

The description of  $I_{pa}$  and  $I_{pc}$  was given in Section 5.2.3 and these were the responses of  $[\text{Fe}(\text{CN})_6]^{3-/4-}$  redox species obtained at the selected electrodes. The reaction of  $[\text{Fe}(\text{CN})_6]^{3-/4-}$  is given in Eq. 5.1 and as it was indicated previously, it is due to the heterogeneous kinetics and IR effect. The slopes (bare PGE;  $I_p/\nu = 2.20 \times 10^{-4} \text{ A/V.s}^{-1}$ , ERGO-PGE;  $I_p/\nu = 1.26 \times 10^{-3} \text{ A/V.s}^{-1}$ , and ERGO-Au-PGE;  $I_p/\nu = 1.34 \times 10^{-3} \text{ A/V.s}^{-1}$ ) found in the above equations from the plot of scan rate vs peak current were used to determine surface coverage capacity at each electrode using Eq. 5.2. The coverage capacities were found to be; bare PGE =  $1.46 \times 10^{-9} \text{ mol.cm}^{-2}$ , ERGO-PGE =  $8.38 \text{ mol.cm}^{-2}$ , and ERGO-Au-PGE =  $8.91 \text{ mol.cm}^{-2}$ . The presence of ERGO and intended AuNPs prove ease electrochemical reactions occurring at the electrode surface.

The plots of  $I_p$  vs  $\nu$  in Figure 6.3 [(I) – (III)] (B) indicated deviation from linearity and this was observed in the  $R^2$  values obtained for the electrodes. Therefore, from this observation, the electrochemical system was not diffusion-controlled. And so, further investigations proceeded with the plot of  $I_p$  vs  $\nu^{1/2}$  shown in Figure 6.3 [(I) – (III)] (C) for the selected electrodes. The regression equations for each are given below;

Bare PGE:

$$I_{pa} (\mu A) = 9.57 \times 10^{-5} v^{1/2} (V.s^{-1}) + 2.11 \times 10^{-6} (R^2 = 0.9962)$$

$$I_{pc} (\mu A) = -3.54 \times 10^{-5} v^{1/2} (V.s^{-1}) - 6.82 \times 10^{-6} (R^2 = 0.9749)$$

ERGO-PGE:

$$I_{pa} (\mu A) = 5.41 \times 10^{-4} v^{1/2} (V.s^{-1}) - 7.57 \times 10^{-6} (R^2 = 0.999)$$

$$I_{pc} (\mu A) = -5.67 \times 10^{-4} v^{1/2} (V.s^{-1}) + 1.74 \times 10^{-5} (R^2 = 0.9865)$$

ERGO-Au-PGE:

$$I_{pa} (\mu A) = 5.80 \times 10^{-4} v^{1/2} (V.s^{-1}) - 1.01 \times 10^{-5} (R^2 = 0.9983)$$

$$I_{pc} (\mu A) = -5.64 \times 10^{-4} v^{1/2} (V.s^{-1})^{1/2} + 1.10 \times 10^{-5} (R^2 = 0.9992)$$

The values of  $R^2$  improved and the plots obtained showed linearity, which was an indication of a diffusion-controlled reaction. The slopes (bare PGE;  $I_{pa}/v^{1/2} = 9.57 \times 10^{-5} A/(V.s^{-1})^{1/2}$ ;  $I_{pc}/v^{1/2} = -3.54 \times 10^{-5} A/(V.s^{-1})^{1/2}$ ), ERGO-PGE; ( $I_{pa}/v^{1/2} = 5.41 \times 10^{-4} A/(V.s^{-1})^{1/2}$ ;  $I_{pc}/v^{1/2} = -5.67 \times 10^{-4} A/(V.s^{-1})^{1/2}$ ), and ERGO-Au-PGE; ( $I_{pa}/v^{1/2} = 5.80 \times 10^{-4} A/(V.s^{-1})^{1/2}$ ;  $I_{pc}/v^{1/2} = -5.64 \times 10^{-4} A/(V.s^{-1})^{1/2}$ ) were used to determine diffusion coefficients of  $[Fe(CN)_6]^{3-/4-}$  ions in the Randles-Sevcik equation (Eq. 5.3). Diffusion coefficient values for bare PGE were  $1.98 \times 10^{-7} cm^2.s^{-1}$  ( $I_{pa}$ ) and  $2.71 \times 10^{-8} cm^2.s^{-1}$  ( $I_{pc}$ ), ERGO-PGE were  $6.31 \times 10^{-6} cm^2.s^{-1}$  ( $I_{pa}$ ) and  $6.94 \times 10^{-6} cm^2.s^{-1}$  ( $I_{pc}$ ), and ERGO-Au-PGE had values of  $7.26 \times 10^{-6} cm^2.s^{-1}$  ( $I_{pa}$ ) and  $6.87 \times 10^{-6} cm^2.s^{-1}$  ( $I_{pc}$ ). The active electrode surfaces were determined to be  $0.0286 cm^2$ ,  $0.162 cm^2$ , and  $0.173 cm^2$  for bare PGE, ERGO-PGE, and ERGO-Au-PGE, respectively. The increase in the ascending order is owing to the modification of the PGE.

The plot of  $\ln I_p$  vs  $\ln v$  was also studied to further validate that the electrochemical reactions occurring at the electrode were driven by diffusion. Thus, (D) of Figure 6.3 (I) – (III) shows the results for bare PGE, ERGO-PGE, and ERGO-Au-PGE, and the regression equations are given as such below;

Bare PGE:

$$\ln I_{pa} = 0.4543 \ln v - 9.2927 \quad (R^2 = 0.9977)$$

$$\ln I_{pc} = -0.2317 \ln v + 10.42 \quad (R^2 = 0.9414)$$

ERGO-PGE:

$$\ln I_{pa} = 0.5403 \ln v - 7.4692 \quad (R^2 = 0.9995)$$

$$\ln I_{pc} = -0.5772 \ln v + 7.402 \quad (R^2 = 0.9952)$$

ERGO-Au-PGE:

$$\ln I_{pa} = 0.5698 \ln v - 7.3314 \quad (R^2 = 0.9936)$$

$$\ln I_{pc} = -0.561 \ln v + 7.3953 \quad (R^2 = 0.9994)$$

The slopes in these equations also were close to the theoretical slope of 0.5 as it was the case with ERGO-Sb-PGE, which is an indication of a diffusion-controlled system. Once more, bare PGE had a slope of -0.2317 for the cathodic peak and so indicates complexities of the electrode with the lack of modification.

### **6.3. Electro-oxidation of PC at ERGO-Au-PGE**

The DPV experiments were carried out in the potential range 0.0 to +1.0 V vs. Ag/AgCl (3 mol.L<sup>-1</sup> KCl) in 0.1 mol.L<sup>-1</sup> PBS at pH 7.0 containing 10 μmol.L<sup>-1</sup> PC at the electrochemically characterized electrodes. Figure 6.4 shows voltammograms of bare PGE (a), ERGO-PGE (b), and ERGO-Au-PGE (c). The observed peaks showed potential shift from 0.423 V of the bare PGE, to that of the modified electrodes; ERGO-PGE and ERGO-Au-PGE, at 0.358 V.

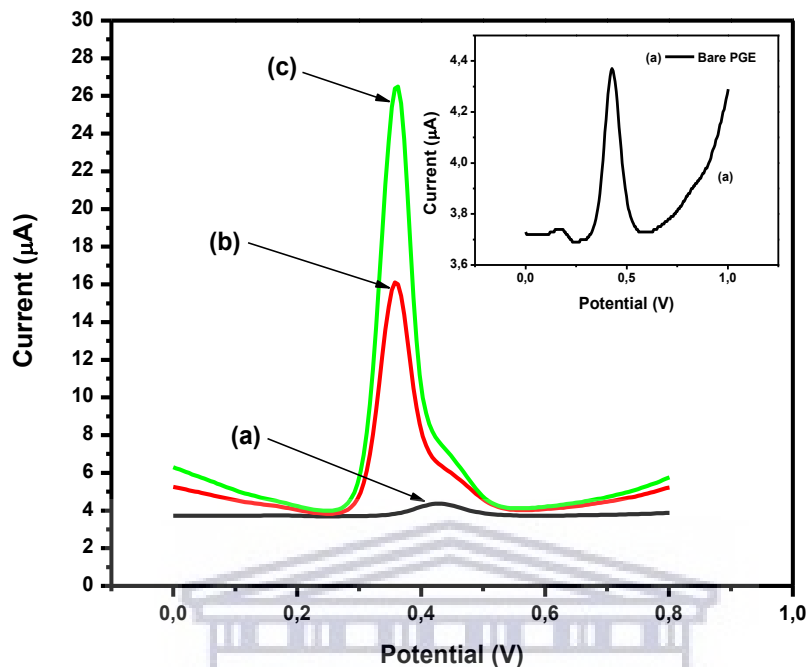


**Figure 6.4:** Differential pulse voltammograms of bare PGE (a), ERGO-PGE (b), and ERGO-Au-PGE (c) in 0.1 mol.L<sup>-1</sup> PBS at pH 7.0 containing 10 µmol.L<sup>-1</sup> PC solution.

The enhanced peak current response was by a factor of 1.9 for ERGO-Au-PGE from that of ERGO-PGE. The greatest peak current enhancement was also observed as established by the peak current difference between bare PGE and ERGO-PGE, by 14 times which could be attributed to the increased surface area due to the electrode modification by GO. Enhancement by ERGO-Au-PGE indicated good electrocatalytic activity of the modified electrode towards the electro-oxidation of PC due to the expected presence AuNPs [288].

#### 6.4. Effect of Deposition Time

The optimum deposition time was investigated for modification of PGE with graphene oxide-gold material which was subsequently used in the electro-oxidation of PC. The deposition times were varied from 60 to 300 s, while the remaining parameters were kept constant according to the CV conditions previously described. Figure 6.5 demonstrates different deposition times along with the corresponding peak currents.

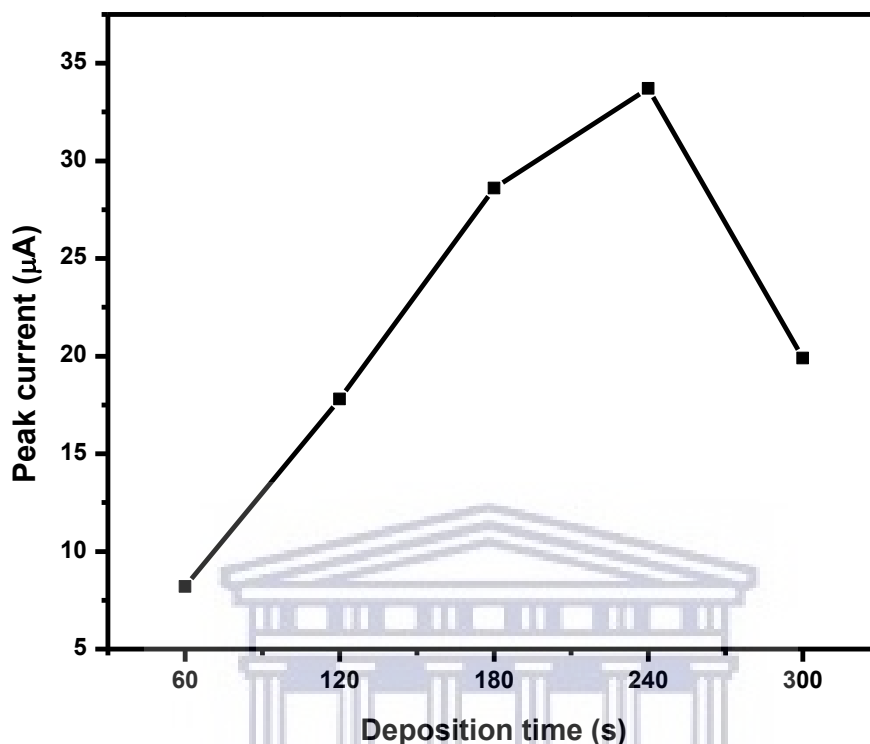


**Figure 6.5:** Influence of the deposition time on the surface modification of electrode for the electro-oxidation of PC at ERGO-Au-PGE.

For the investigated deposition times; 60, 120, 180, 240, 300 s in Figure 6.5, a deposition time of 60 s was the lowest for which PGE could be modified, and as such gave the worst results. There was improvement as the deposition time increase, and so 240 s showed the greatest enhancement with an increase of about 2 times. This is the optimum surface modification before it reaches saturation where signal transmitted through the modified ERGO-Au-PGE is impeded.

### 6.5. Effect of Cycles

The various coating cycles for the modification of graphene oxide-gold material, which were 1, 3, 5, 7, and 9 with the remaining parameters kept constant was also investigated. A depiction of the plot of ERGO-Au-PGE at different number of cycles for reduction of GO-Au salt at the electrode surface is shown in Figure 6.6.

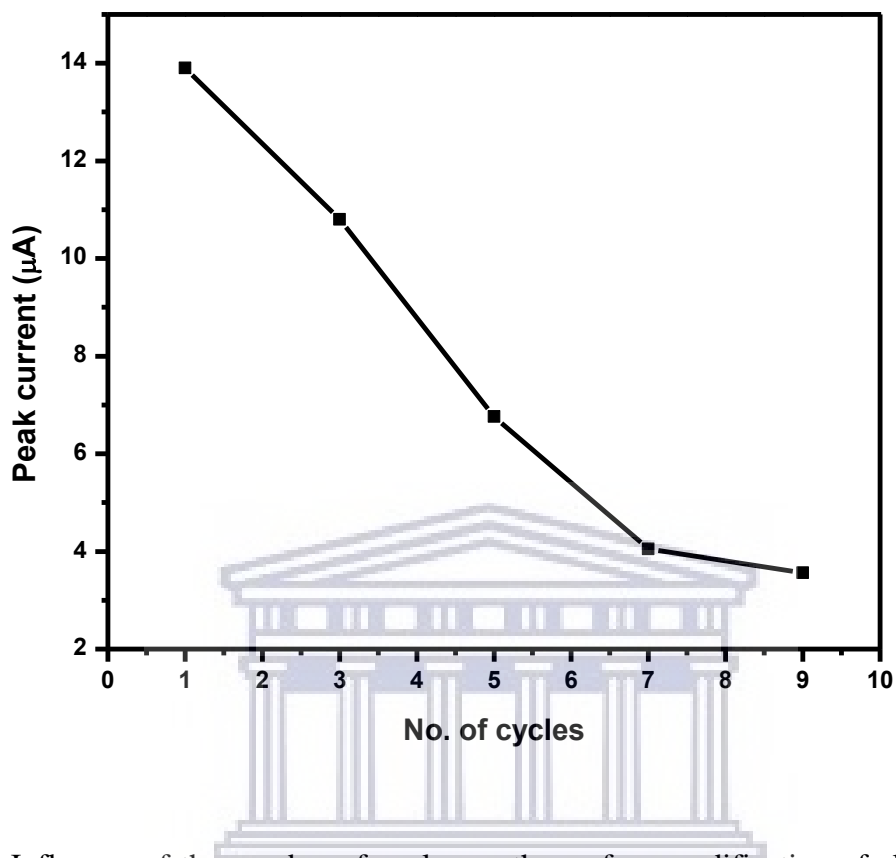


**Figure 6.6:** Influence of the number of cycles on the surface modification of electrode for the electro-oxidation of PC at ERGO-Au-PGE.

The greatest enhancement was observed at optimum of 1 cycle. As the number of cycles increased the enhancement disappeared. This can be due to the stretched deposition time used and therefore the reduction of the GO-metal salt on the electrode is more than required, with the modification material forming a thick film at the electrode surface. Hence the current signal sent through the electrode by the platinum wire (auxiliary electrode) became blocked.

### 6.6. Effect of pH

The effect of pH on the electro-oxidation of PC at ERGO-Au-PGE surface was studied in 0.1 mol.L<sup>-1</sup> PBS containing 10 µmol.L<sup>-1</sup> PC solutions with varying pH values from 5.0 to 9.0. The DPV responses of pH (a) 5.0, (b) 6.0, (c) 7.0, (d) 8.0, and (e) 9.0 are shown in Figure 6.7 (A) and in (B) the linear plot of (a) potential with accompanying (b) current plots as function of pH is depicted.

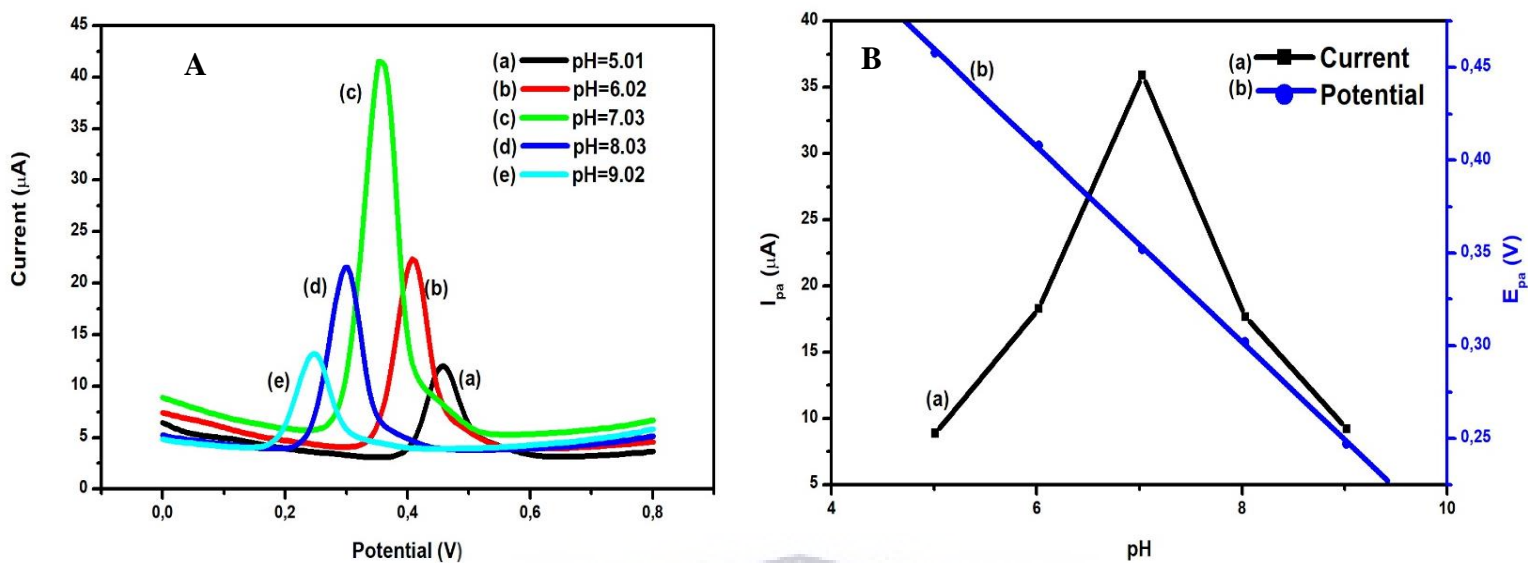


**Figure 6.7:** Effect of pH on the electro-oxidation of PC at ERGO-Au-PGE; DPV responses (A) and linear plots of current and potential as a function of pH (B) in 0.1 mol.L<sup>-1</sup> PBS containing 10 µmol.L<sup>-1</sup> PC solution at various pH values.

The linear plot of potential with pH shown in Figure 6.7 (B) showed responses of anodic peak potentials shifting towards negative values with an increase in pH. The accompanying regression equation was given by;

$$E_{pa} \text{ (V)} = -0.0526 \text{ pH} + 0.723 \text{ (R}^2 = 0.9996\text{)}$$

The slope obtained from the plot was found to be -0.052.6 V/pH, which was in agreement with the Nernst slope of -0.059 V/pH for the same number of electrons and protons involved in the reaction as proposed by the mechanism for electro-oxidation of PC in Scheme 5.1. The results found with ERGO-Au-PGE were similar to those in Section 5.6 of Chapter 5, which showed that electro-oxidation of PC in PBS was optimum in physiological conditions.

### 6.7. Repeatability, Reproducibility, and Stability

The reproducibility and stability of ERGO-Au-PGE was established in conditions performed for ERGO-Sb-PGE. Experiments were repeated during the 7-day period and the results are shown in Figure 6.8 (I) – (II) [(A) – (D)].

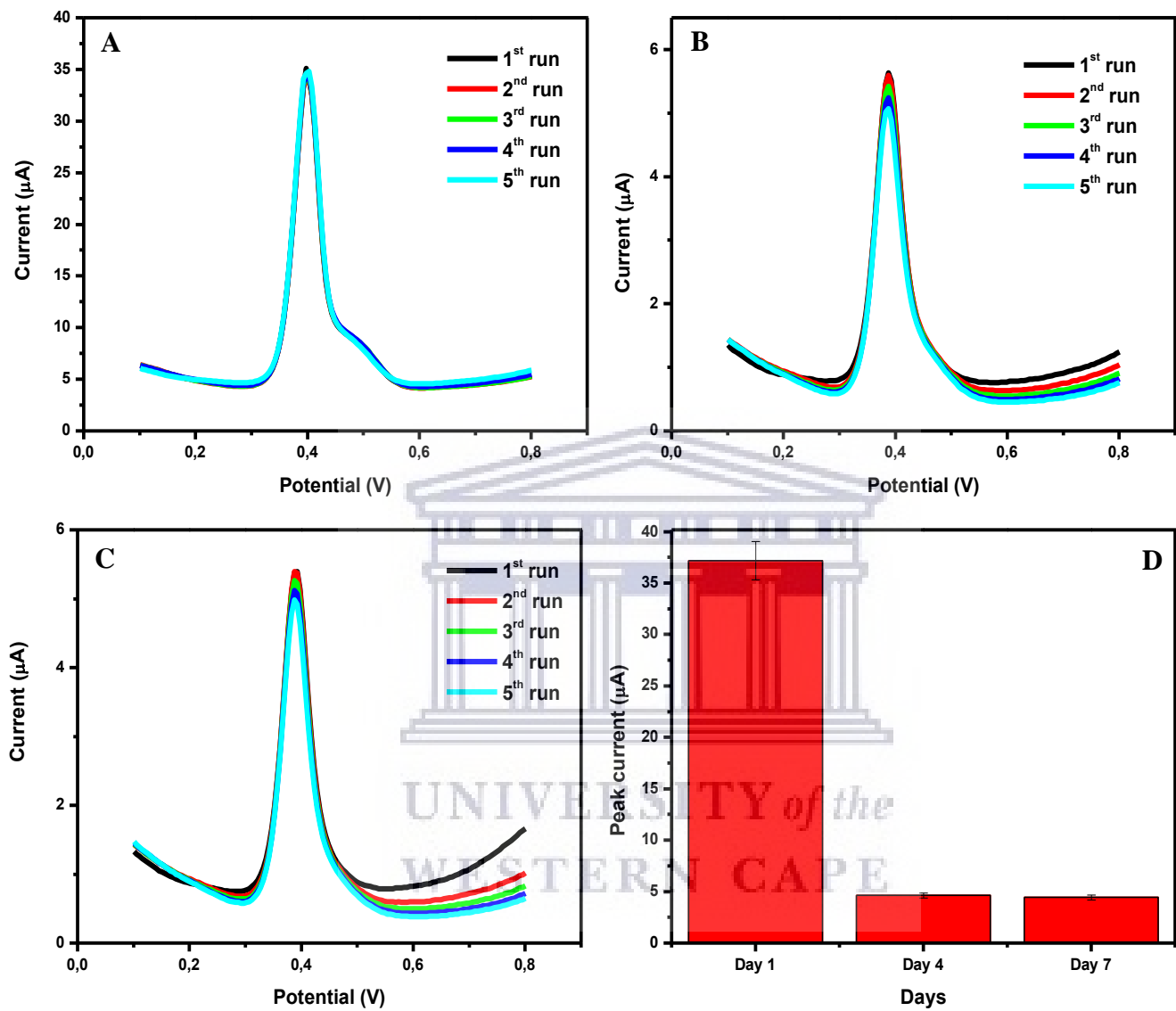


**Figure 6.8 (I):** DPV measurements obtained on the same ERGO-Au-PGE in 10  $\mu\text{mol.L}^{-1}$  PC solution in 0.1  $\text{mol.L}^{-1}$  PBS for repeatability, reproducibility, and stability (A to C), and the accompanying bar graph showing peak current over Day 1, Day 4, and Day 7 (D).

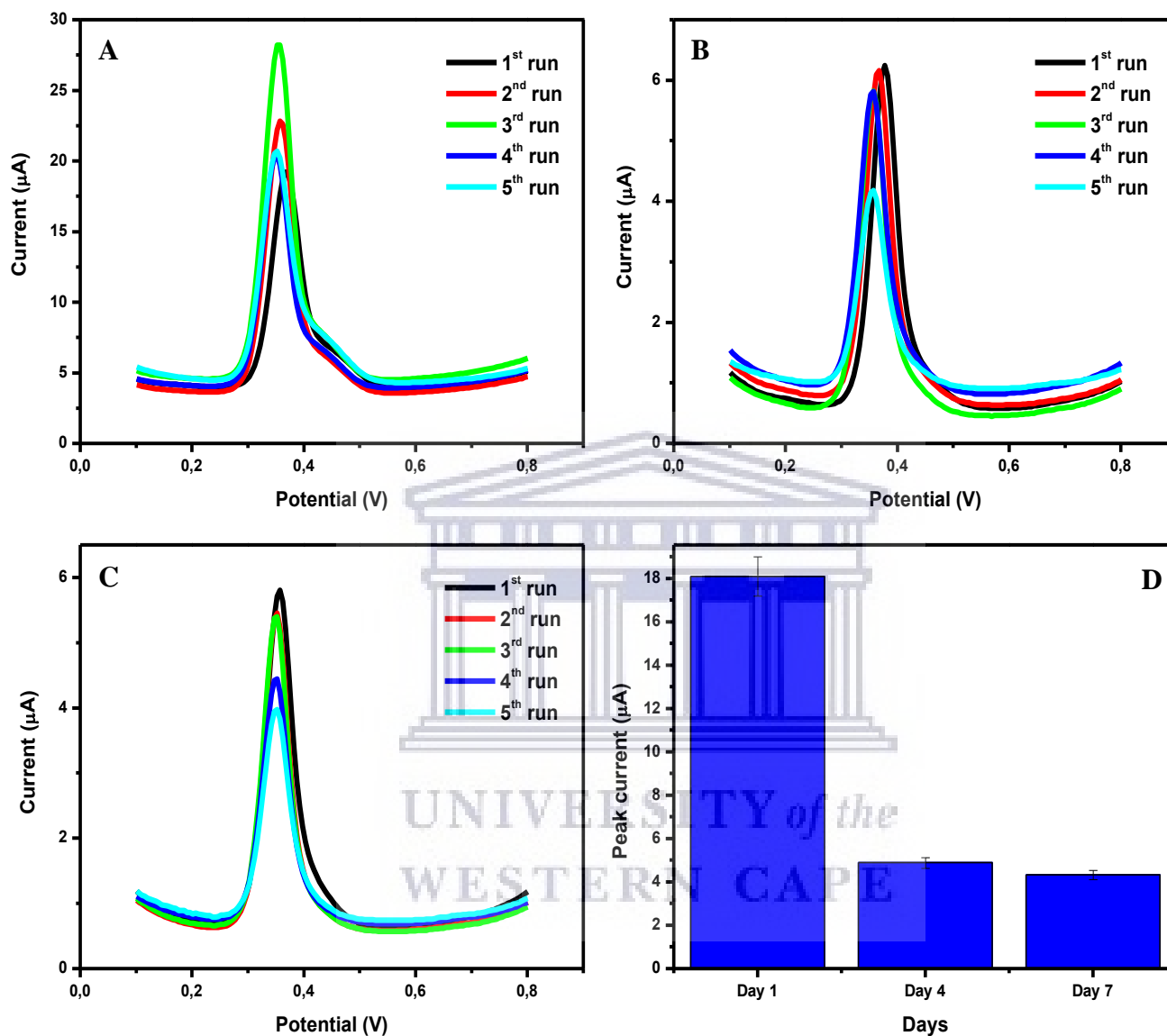


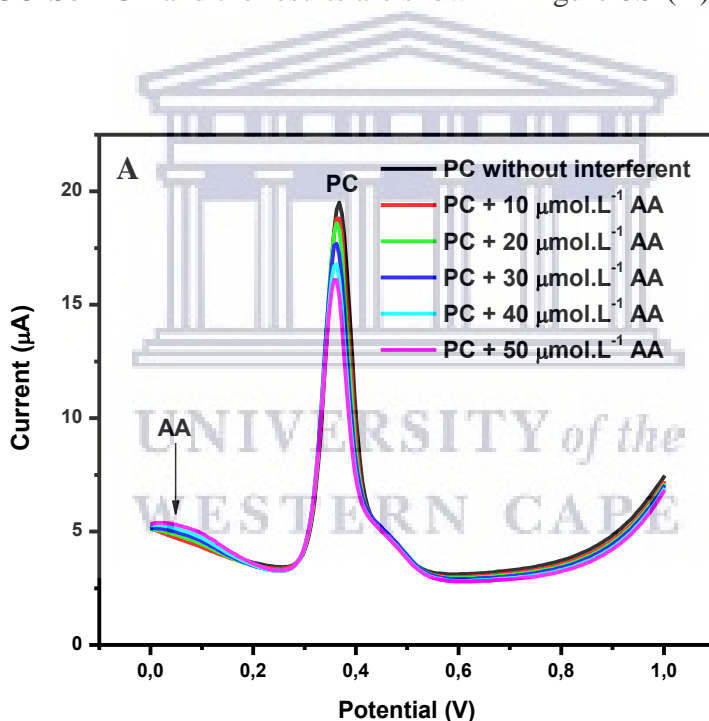
**Figure 6.8 (II):** DPV measurements obtained on multiple ERGO-Au-PGEs in 10  $\mu\text{mol.L}^{-1}$  PC solution in 0.1  $\text{mol.L}^{-1}$  PBS for repeatability, reproducibility, and stability (A to C), and the accompanying bar graph showing peak current over Day 1, Day 4, and Day 7 (D).

Similarly, in the previous chapter, experiments performed on the same electrode showed better analysis than on the individual tests. In Figure 6.8 (A) to (C), the tests on the same ERGO-Au-

PGE for Days 1, 4, and 7 are depicted. Here, the comparison of these experiments on the same ERGO-Au-PGE showed RSDs of 3.07 %, 3.29 %, and 2.08 % for the respective indicated Days. For experiments performed on individual ERGO-Au-PGEs, RSDs were 19.08 %, 20.06 %, and 19.21 % for Days 1, 4, and 7, respectively. As expected, intra-day (Day 1) determinations showed better peak current stability and also same-electrode tests had better reproducibility when compared to inter-day experiments (Days 4 and 7) as shown by Figure 6.8 [(I) – (II)] (D).

### 6.8. Interference Studies

The ERGO-Au-PGE was tested for selectivity towards PC in the presence of AA, FA, and CAFF as interferents. Differential pulse voltammetric measurements proceeded as previously performed for ERGO-Sb-PGE and the results are shown in Figure 6.9 (A) to (C).



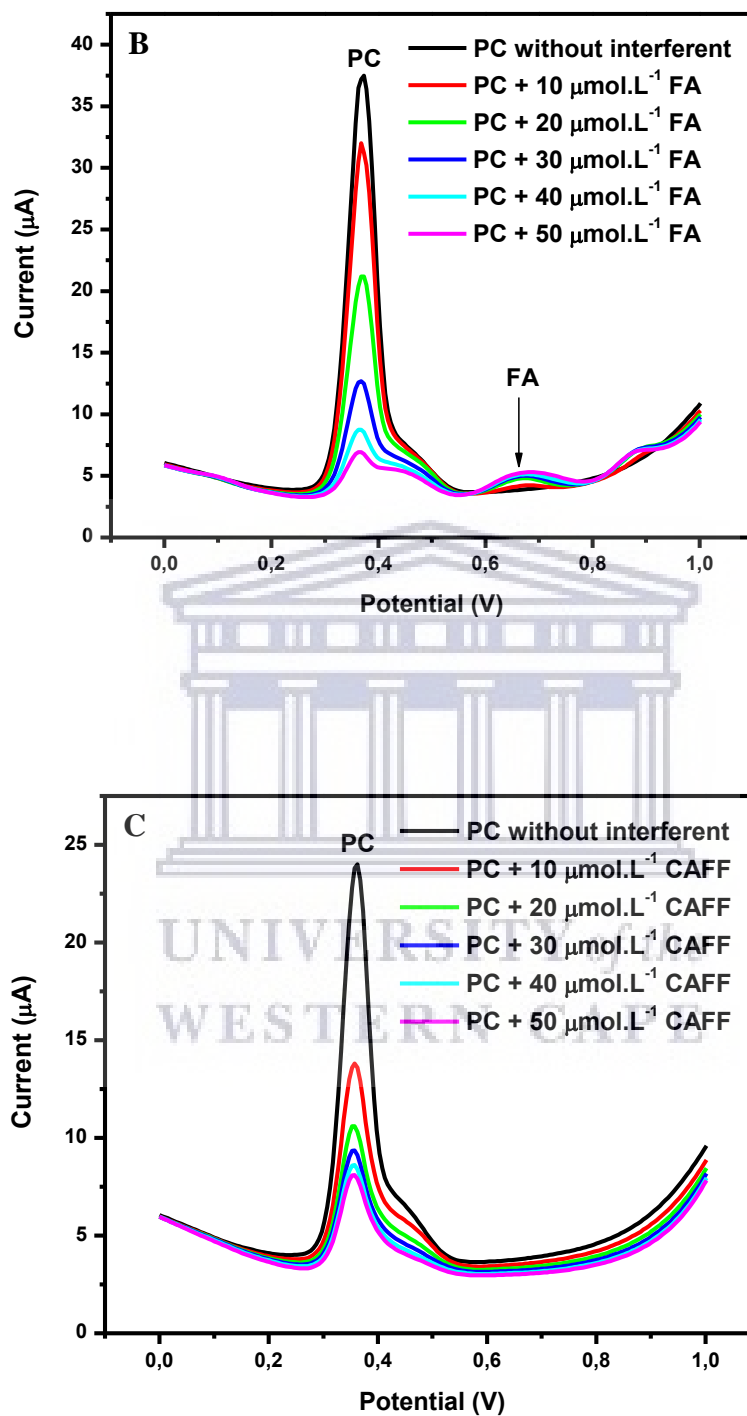


**Figure 6.9:** DPV results showing electro-oxidation of 10  $\mu\text{mol.L}^{-1}$  PC in 0.1  $\text{mol.L}^{-1}$  PBS (pH = 7.03) at ERGO-Au-PGE in the presence of interferents; (A) AA, FA (B), and CAFF (C) at different concentrations (10, 20, 30, 40, and 50  $\mu\text{mol.L}^{-1}$  of interferent).

**Table 6.1:** The results below depict the effect of interferences namely; AA, FA, and CAFF on the oxidation peak current of PC at different concentrations, and their relative standard deviations (%).

Interferent	C <sub>i</sub> (μmol.L <sup>-1</sup> )	PC peak current (A)	RSD (%)
AA	10 - 50	$1.47 \times 10^{-5} \pm 1.27 \times 10^{-6}$	8.64
FA	10 - 50	$1.29 \times 10^{-5} \pm 1.02 \times 10^{-5}$	79.06
CAFF	10 - 50	$6.71 \times 10^{-6} \pm 2.13 \times 10^{-6}$	31.8

C<sub>i</sub>: Concentration of interferent

Peak current: average ± STDEV

RSD % of peak currents (n = 3)

In Figure 6.9 (A), PC and AA exist in solution and the oxidation peak potentials were at 0.378 V and 0.0806 V, respectively. The PC oxidation peak current ( $1.47 \times 10^{-5} \pm 1.27 \times 10^{-6}$ ) had an RSD of 8.64 % as shown in Table 6.2 in the presence of AA. Considering the RSD found for PC only in solution in Section 6.7, this indicated presence of interference although slight. Relative standard deviation considered for PC and FA ( $1.29 \times 10^{-5} \pm 1.02 \times 10^{-5}$ ) was at 79.06 %, with peak potentials at 0.368 V for PC and 0.675 V for FA.

This was an indication of FA interfering with the oxidation of PC. Furthermore, there was an observed residual peak at 0.881 V and this also continued to appear even in repeat experiments. Considering there was only PC and FA in solution, this peak may be due to the interaction of the two mentioned analytes. This may be an opportunity to investigate further in future study. In the presence of CAFF, PC peak current ( $6.71 \times 10^{-6} \pm 2.13 \times 10^{-6}$ ) had an RSD of 31.7 % and this was an observation of interference.

### 6.9. Limit of Detection

The analytical performance of ERGO-Au-PGE was investigated to establish a linear concentration range and a limit of detection of PC in 0.1 mol.L<sup>-1</sup> PBS (pH 7.01) containing

different PC concentrations. Figure 6.10 (A) shows DPV results for the concentrations of PC used in the range 0.5 – 10  $\mu\text{mol.L}^{-1}$  PC and in (B) the linear calibration curve.

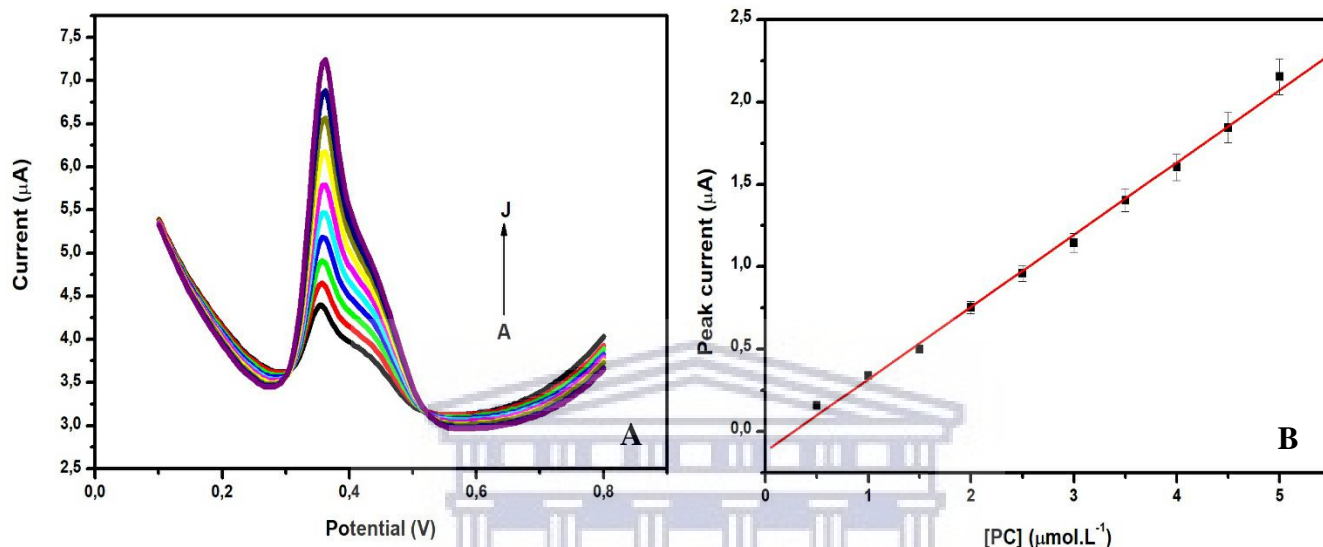


**Figure 6.10:** DPVs obtained at ERGO-Au-PGE in 0.1  $\text{mol.L}^{-1}$  PBS (pH 7.01) containing concentrations of PC (A - J: 0.1, 0.2, 0.3, 0.4, 0.5, 0.6, 0.7, 0.8, 0.9, and 1.0  $\mu\text{mol.L}^{-1}$ ) in (A) and the corresponding calibration plots in (B).

The construction of these was based on the results from the average values of data collected from three experiments conducted. The linear calibration plot produced a regression equation:

$$I_{pa} (A) = 4.39 \times 10^{-7} [PC] (\mu\text{mol.L}^{-1}) - 1.21 \times 10^{-7} (R^2 = 0.9961),$$

which was observed in the linear dynamic range from 0.5 – 5.0  $\mu\text{mol.L}^{-1}$ . Detection limit was estimated using Eq. (5.4), with the slope obtained from the linear plot. It was determined to be 11.0  $\text{nmol.L}^{-1}$  taken from average values in Table 6.2 for PC at ERGO-Au-PGE. The results obtained were comparable with those in Table 5.3.

**Table 6.2:** Calibration data from the experiments conducted for analytical performance of PC at ERGO-Au-PGE.

Experiment no.	Linear range ( $\mu\text{mol.L}^{-1}$ )	Correlation coefficient ( $R^2$ )	LOD ( $\mu\text{mol.L}^{-1}$ )
1	0.5 – 5.0	0.9957	0.011
2	0.5 – 5.0	0.9977	0.012
3	0.5 – 5.0	0.9821	0.012
Average	0.5 – 5.0	0.9961	0.011

### 6.10. Analytical Application of ERGO-Au-PGE for PC

The recovery of PC sample at ERGO-Au-PGE contained in a 500 mg commercial tablet was determined using standard addition method. The triplicate experimental results were collected as DPV measurements and are displayed in Figure 6.11 (A). The accompanying standard addition linear plot is shown in Figure 6.11 (B).

The recoveries were between 98.5 % and 100.3 % PC for samples with additions of 0.662, 1.324, and 1.986  $\mu\text{mol.L}^{-1}$  PC, and the determinations produced average  $\pm$  standard deviation of  $0.655 \pm 0.004 \mu\text{mol.L}^{-1}$  PC in a commercial tablet (Table 6.3) at ERGO-Au-PGE. Additionally, PC was also recovered using calibration curve method for which a consistent concentration of 1.0  $\mu\text{mol.L}^{-1}$  was considered, and the results are also shown in Table 6.3. The results were considered satisfactory for the current study.

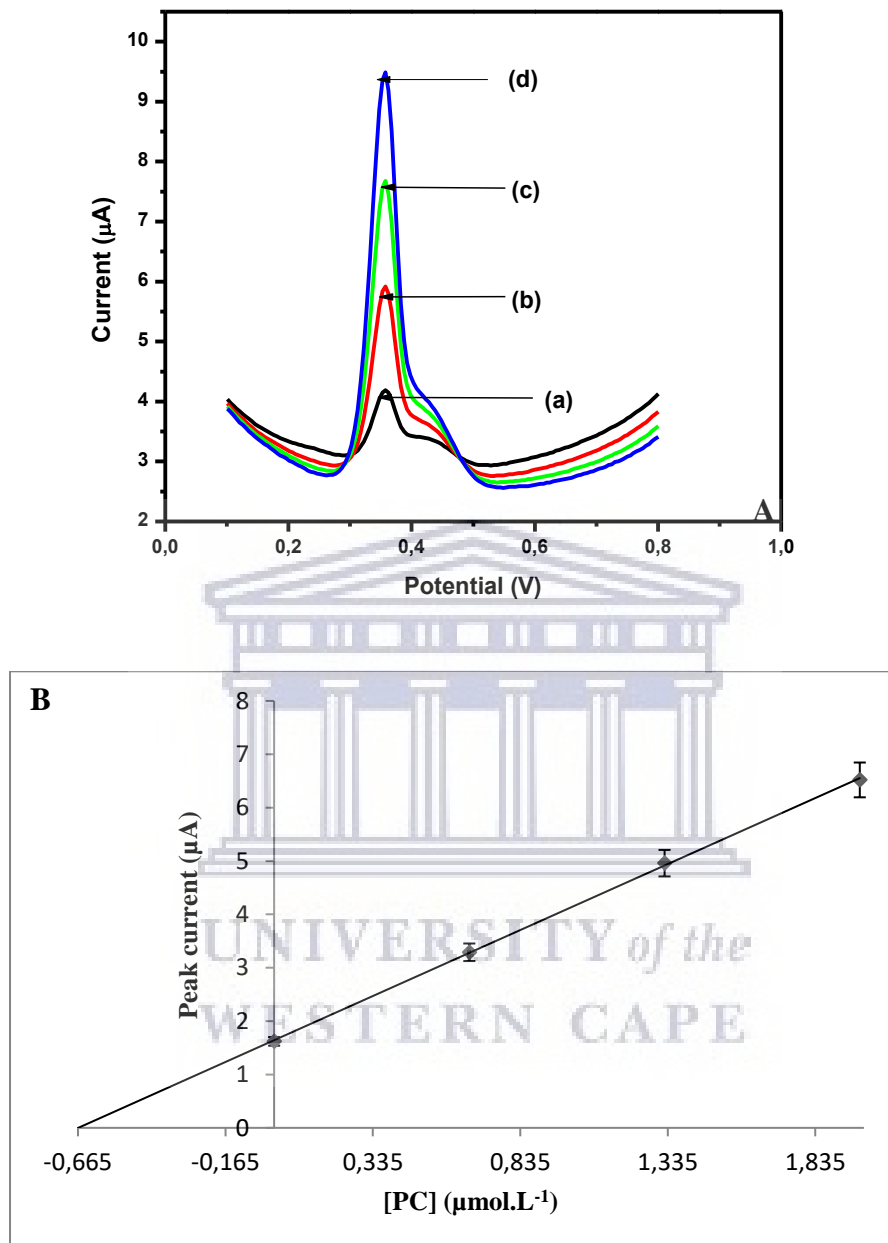


**Figure 6.11:** DPV measurements for the recovery of PC at ERGO-Au-PGE in (A) with standard additions at different concentrations of sample (a); sample +  $0.662 \mu\text{mol.L}^{-1}$  (b), sample +  $1.324 \mu\text{mol.L}^{-1}$  (c), and sample +  $1.986 \mu\text{mol.L}^{-1}$  PC solution (d), and linear plot of the average standards added (B).

**Table 6.3:** Results of the recovered PC from a commercial tablet containing 500 mg PC at ERGO-Au-PGE using standard addition and calibration curve methods.

Method	Recovered [PC] ( $\mu\text{mol.L}^{-1}$ )	Recovery (%)
Standard addition ( $0.662 \mu\text{mol.L}^{-1}$ PC)	0.6552	98.9
	0.6596	99.7
	0.6516	98.5
	0.6607	99.7
	0.6627	100.05
Average $\pm$ STDEV	$0.6579 \pm 0.004$	
Calibration curve ( $1.0 \mu\text{mol.L}^{-1}$ PC)	0.9774	97.7
	1.000	100.02
	1.016	101.6
	0.9969	99.7
	1.011	101.06
Average $\pm$ STDEV	$1.000 \pm 0.0015$	

### 6.11. Modification of PGE with Other Electrochemically Graphene Oxide-Metal Nanocomposites

Gold is considered to be the noblest of metals [289], and noble metal nanoparticles have attracted great interests owing to their high catalytic activities for many chemical reactions [29]. Due to this fact, ERGO-Au-PGE was developed for the current study. Other noble metal NPs (Ag, Pd, and Pt) *in situ* modification on GO sheets with subsequent electrodeposition onto PGEs was tested for electro-oxidation of PC. The DPV experiments were carried out accordingly and the results are shown in Figure 6.12 (A) – (C).

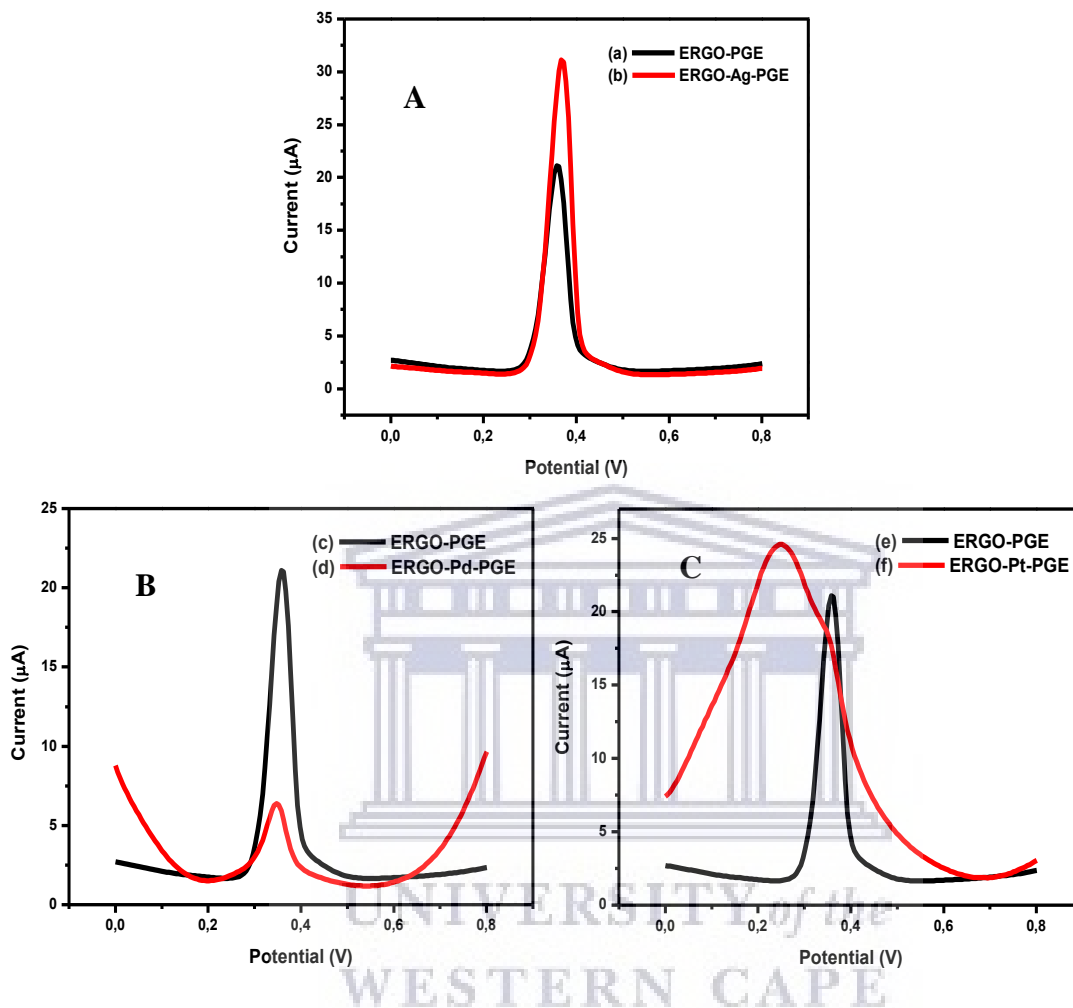


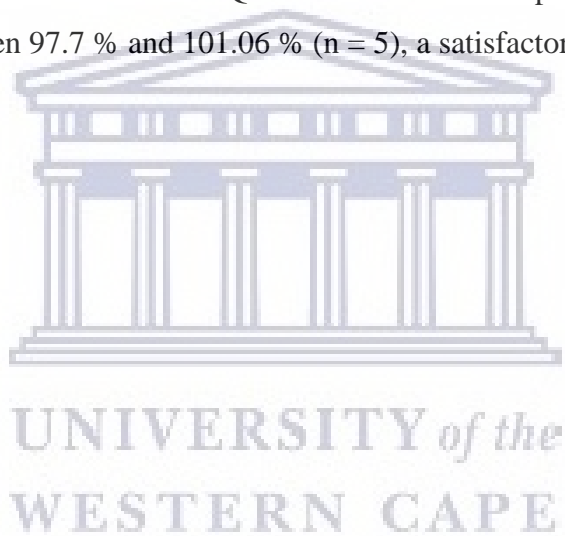
**Figure 6.12:** Differential pulse voltammograms for electro-oxidation of PC at (A) ERGO-Ag-PGE, at (B) ERGO-Pd-PGE, and (C) ERGO-Pt-PGE in  $0.1 \text{ mol.L}^{-1}$  PBS at pH 7.03 containing  $10 \mu\text{mol.L}^{-1}$  PC solution.

In Figure 6.12 (A), ERGO-Ag-PGE showed peak current enhancement of 1.5 when compared to that of ERGO-PGE. However, ERGO-Pd-PGE in Figure 6.12 (B) had poor peak current response with ERGO-PGE being greater by a factor of 3.3. Incorporation of GO and PdNPs has been reported to be used as electrocatalysts in determination of PC. The performance of Pd-based catalysts is emphasized on the supporting matrix and stability to promote the enhancement of synergistic effect [29]. In Figure 6.12 (C), ERGO-Pt-PGE had no distinct PC oxidation peak to

draw any remarks. Therefore, in the current study the results shown by ERGO-Pd-PGE and ERGO-Pt-PGE may be due to instability of the modification on the electrode which may need improvements on the modification technique.

### **6.12. Conclusion**

Modification of PGE with graphene oxide-gold nanoparticles was attempted via electro-deposition on the electrode surface to fulfill a functional sensor. The achieved ERGO-Au-PGE sensor was electrochemically characterized and used to acquire enhancement of electrochemical response of PC using adsorptive stripping differential pulse voltammetry. This response was further enhanced to obtain optimum detection of PC. The ERGO-Au-PGE sensor showed comparable detection limit of  $11.0 \text{ nmol.L}^{-1}$ . Quantification of PC in pharmaceutical commercial tablet had recoveries between 97.7 % and 101.06 % ( $n = 5$ ), a satisfactory result for the study.



## CHAPTER SEVEN:

### Conclusions and Future Work

Pencil graphite electrodes were modified with electrochemically reduced graphene oxide metal nanocomposite through electro-deposition to develop sensors such as ERGO-Sb-PGE and ERGO-Au-PGE, which were used for the electrochemical detection of PC using adsorptive stripping differential pulse voltammetry. This was achievable through synergistic combination of ERGO and an otherwise metal nanocomposite thus increasing surface area for the electrochemical reaction to occur and inducing electrocatalytic activity of the sensor. The sensors showed comparable detection limits with other similar electrodes, with LODs of  $0.57 \text{ nmol.L}^{-1}$  and  $11.0 \text{ nmol.L}^{-1}$  for ERGO-Sb-PGE and ERGO-Au-PGE, respectively. The electrochemical response of each of the sensors was used for detection of PC through recovery in a commercial pharmaceutical tablet. The recovery percentages of PC were between 98.3 % and 101.6 % ( $n = 5$ ) corresponding to ERGO-Sb-PGE, and for ERGO-Au-PGE were between 97.7 % and 101.06 % ( $n = 5$ ), which were found to be satisfactory for the study.

The affirmation of MNPs decoration on GO morphology was to be indicated through HRSEM and HRTEM studies. However, SbNPs were not found as it was to be expected since there was no Sb standard to relate to. With AuNPs, they were also not apparent though this was not expected. These experiments could not be repeated due SEM and TEM machines being not operational at the time of experiments. Experiments were conducted to establish reproducibility and stability within the same electrode and comparing those with individual measurements at different periods. Individual electrode experiments displayed inconsistencies and not only that, but it was difficult to obtain precise and accurate calibration curves. Due to these electrodes being cheap and disposable, a maximum of 5 – 10 measurements were performed within the same electrode for certain experiments. Although there were indications of fouling for experiments on the same electrode, the marginal error was negligible.

The current study prompted interest into future research of highly sensitive, simple, accurate, and cost-effective electrodes. Therefore, this enables the introduction of microfluidic paper-based analytical devices ( $\mu$ PADs). These not only fit the aforementioned attributes but they are also comprised of lightness, low thickness, and flexibility. Future studies will also ensure the

implementation of green approach to the determination of analytes. With the consideration of GO, the study will be facilitated by its spectacular properties, as the research into the field of graphene-based sensing platform is growing rapidly.



## REFERENCES

1. Eaton, D. L. and Gallagher, E. P. (2010). Comprehensive Toxicology, Fourteen Volume Set Electronic Source p. 10. *Elsevier*. USA.
2. Barrenberg, E. and Garbe, E. (2015). Use of over-the-counter (OTC) drugs and perceptions of OTC drug safety among German adults. *Eur. J. Clin. Pharmacol.* 71, 1389-1390.
3. Wazaify, M., Shields, E., Hughes, C. M., McElnay, J. C. (2005). Societal perspectives on over-the-counter (OTC) medicines. *Fam. Pract.* 22, 170-176.
4. Brune, K., Hinz, B., Otterness, I. (2009). Aspirin and acetaminophen: should they be available over the counter? *Curr. Rheumatol. Rep.* 11, 36-40.
5. Michelsen, A. (2012). Medikamente sind keine Smarties [Medicines aren't smarties]. In: Fuhrmann T (Ed.) ZDF *Morgenmagazin*.
6. Hackenbroch, V. and Höflinger, L. (2011). Verblüffende Sorglosigkeit [astonishing carelessness]. *Spiegel Verlag.* 50, 146–148.
7. Mensing, M., Streich, W., Ter schüren, C. (2011). Die Bevölkerungsbefragung zur Gesundheit 2009. Eine repräsentative Erhebung für NRW [A representative population health survey for North Rhine-Westphalia]. In: *LIGA.NRW* (Ed.). Landesinstitut für Gesundheit und Arbeit Nordrhein- Westfalen, Düsseldorf.
8. Zafar, S., Syed, R., Waqar, S. *et al.* (2008). Self-medication amongst university students of Karachi: prevalence, knowledge and attitudes. *Journal of the Pakistan Medical Association.* 58 (4): 214-217.
9. Filho, L., Antonio, I., Lima-Costa. M. F., Uchoa, E. (2004). Bambui Project: a qualitative approach to self-medication. *Cad Saude Publica.* 20, 1661-1669.
10. Bretagne, J. F., Richard Molyoivd, B., Honnorat, C. *et al.* (2006). [Gastroesophageal reflux in the French general population: national survey of 8000 adults]. *Presse Med.* 35, 23-31.
11. Shankar, P. R., Partha, P., Shenoy, N. (2002). Self-medication and non-doctor prescription practices in Pokhara valley, Western Nepal: a questionnaire-based study. *BMC Fam. Pract.* 3, 17.

12. Abahussain, E., Matowe, L. K., Nicholls, P. J. (2005). Self-reported medication use among adolescents in Kuwait. *Med Princ Pract.* 14, 161-164.
13. Mensing, M., Streich, W., Ter schüren, C. (2011). Die Bevölkerungsbefragung zur Gesundheit 2009. Eine repräsentative Erhebung für NRW [A representative population health survey for North Rhine-Westphalia]. In: LIGA.NRW (Ed.). *Landesinstitut für Gesundheit und Arbeit Nordrhein-Westfalen, Düsseldorf.*
14. Beitz, R., Dören, M., Knopf, H., Melcher t, H-U (2004) Selbstmedikation mit Over-the-Counter (OTC) Präparaten in Deutschland [Self-medication with OTC drugs in Germany]. *Bundesgesundheitsblatt-Gesundheitsforschung-Gesundheitsschutz* 47, 1043-1050.
15. Tennis, P. (1990). Drug utilization by the 30 – 64 year-old people in two cities in the Federal Republic of Germany in 1984. *Eur. J. Clin. Pharmacol.* 38, 447-452.
16. Krska, J., Jones, L., McKinney, J., Wilson, C. (2011). Medicine safety: experiences and perceptions of the general public in Liverpool. *Pharmacoepidemiol Drug Saf.* 20, 1098-1103.
17. Calamusa, A., Di Marzio, A., Cristofani, R. *et al.* (2012). Factors that influence Italian consumers' understanding of over-the-counter medicines and risk perception. *Patient. Educ. Couns.* 87, 395-401.
18. Brabers, A. E., Van Dijk, L., Bouvy, M. L., De Jong, J. D. (2013). Where to buy OTC medications? A cross-sectional survey investigating consumers' confidence in over-the-counter (OTC) skills and their attitudes towards the availability of OTC painkillers. *BMJ Open.* 3, e003455.
19. Wazaify, M., Kennedy, S., Hughes, C. M., McElnay, J. C. (2005). Prevalence of over-the-counter drug-related overdoses at accident and emergency departments in Northern Ireland – a retrospective evaluation. *J. Clin. Pharm. Ther.* 30, 39-44.
20. Ker, J. and Erasmus, R. J. E. (1995). Acute Paracetamol Poisoning: Two Case Studies and a Review. *S. Afr. Fam. Pract.* 16, 102-106.
21. Monteagudo, F. S. E and Folb, P. I. (1987). Paracetamol poisoning at Groote Schuur Hospital. A 5 year experience. *S. Afr. Med. J.* 72, 773-776.

22. Taylor Jr., R., Pergolizzi Jr., J. V., Raffa, R. B. (2012). Acetaminophen (Paracetamol): Properties, Clinical Uses, and Adverse Effects, p.1. *Nova Science Publishers, Inc.* New York.
23. de Carvalho, R. M., Freire, R. S., Rath, S., Kubota, L. T. (2004). *J. Pharm. Biomed. Anal.* 34, 871.
24. Toes, M. J., Jones, A. L., Prescott, L. (2005). Drug interactions with paracetamol. *Am. J. Ther.* 12 (1): 56-66.
25. Grattan, T., Hickman, R., Darby-Dowman, A. *et al.* (2000). A five way crossover human volunteer study to compare the pharmacokinetics of paracetamol following oral administration of two commercially available paracetamol tablets and three development tablets containing paracetamol in combination with sodium bicarbonate or calcium carbonate. *Eur. J. Pharm. Biopharm.* 49 (3): 225-229.
26. McNeil Consumer Healthcare (2011). *TYLENOL® Professional Product Information.*
27. Mitchell, J. R., Thorgeirsson, S. S., Potter, W. Z. *et al.* (1974). Acetaminophen-induced hepatic injury: protective role of glutathione in man and rationale for therapy. *Clin. Pharmacol. Ther.* 16 (4): 676-684.
28. Ngai, K. S., Tan, W. T., Zainal, Z. *et al.* (2015). Electrocatalytic Study of Paracetamol at a Single-Walled Carbon Nanotube/Nickel Nanocomposite Modified Glassy Carbon Electrode. *Hindawi.* 2.
29. Li, J., Liu, J., Tan, G. *et al.* (2014). High-sensitivity paracetamol sensor based on Pd/graphene oxide nanocomposite as an enhanced electrochemical sensing platform. *Biosensors and Bioelectronics.* 54, 468-475.
30. Sultan, M. A., Maher, H. M., Alzoman, N. Z., Alshehri, M. M., Rizk, M. S., Elshahed, M. S., Olah, I. V. (2013). Capillary electrophoretic determination of antimigraine formulations containing caffeine, ergotamine, paracetamol and domperidone or metoclopramide. *J. Chromatogr. Sci.* 51, 502–510.
31. Abdelaleem, E. A. and Abdelwahab, N. S. (2013). Validated stability indicating RP-HPLC for determination of paracetamol, methacarbamol, and related substances. *Anal. Methods.* 5, 541-545.

32. Abirami, G. and Vetrichelvan, T. (2013). Simultaneous determination of tolperisone and paracetamol in pure and fixed dose combination by UV spectrometry. *Int. J. Pharm. Pharm. Sci.* **5** (1): 488-492.
33. Modick, H., Schütze, A., Pälme, C., Weiss, T. (2013). Rapid determination of N-acetyl-4-aminophenol (Paracetamol) in urine by tandem mass spectrometry coupled with on-line clean-up by two-dimensional turbulent flow/reversed phase liquid chromatography. *J. Chromatogr. B* **925**, 33-39.
34. Khanmohammadi, M., Soleimani, M., Morovvata, F. *et al.* (2012). Simultaneous determination of paracetamol and codeine phosphate in tablets by TGA and chemometrics. *Thermochim. Acta* **530**, 128-132.
35. Görçay, H., Türkoğlu, G., Şahin, Y., Berber, H. (2014). Electrochemical Determination of Paracetamol by a Novel Derivative of Formazan Modified Pencil Graphite Electrode. *Sensors Journal*. **14** (8): 2529-2530.
36. Montastruc, J. L., Bagheri, H., Geraud, T., Lapeyre-Mestre, M. (1997). [Pharmacovigilance of self-medication]. *Therapie*. **52**, 105-110.
37. Bateman, D. N., Carroll, R., Pettie, J. *et al.* (2014). Effect of the UK's revised paracetamol poisoning management guidelines on admissions, adverse reactions and costs of treatment. *Br. J. Clin. Pharmacol.* **78** (3): 610-618.
38. Nematollahi, D., Shayani-Jam, H., Alimoradi, M., Niroomandi, S. (2009). Electrochemical oxidation of acetaminophen in aqueous solutions: Kinetic evaluation of hydrolysis, hydroxylation, and dimerization processes. *Electrochim. Acta*. **54**, 7407-7415.
39. Ebadi, M. (2003). Electrocatalytic oxidation of hydroxylamine by (RuPc)<sub>2</sub> graphite modified electrode. *Electrochim. Acta*. **48** (28): 4233-4238.
40. Özcan, A. and Şahin, Y. (2011). A novel approach for the determination of paracetamol based on the reduction of N-acetyl-p-benzoquinoneimine formed on the electrochemically treated pencil graphite electrode. *Analytica Chimica Acta*. **685**, 9-10.
41. Lapuente, R., Cases, F., Garcés, P. *et al.* (1998). A voltammeter and FTIR-ATR study of the electro polymerization of phenol on platinum electrodes in carbonate medium: influence of sulfide. **451**, 163-171.
42. Koile, R. C. and Johnson, D. C. (1979). Electrochemical removal of phenolic films from a platinum anode. *Anal. Chem.* **51** (6): 741-744.

43. HongChao, Y. Kangbing, W., Shengshui, H., Dafu, C. (2001). Adsorption stripping voltammetry of phenol at Nafion-modified glassy carbon electrode in the presence of surfactants. *Talanta*. **55** (6): 1205-1210.
44. Karikalan, N., Karthik, R., Chen, S-M. *et al.* (2016). Electrochemical properties of the acetaminophen on the screen printed carbon electrode towards the high performance practical sensor applications. *Journal of Colloid and Interface Science*. 483, 109-117.
45. Baranowska, I., Markowski, P., Gerle, A., Baranowski, J. (2008). Determination of selected drugs in human urine by differential pulse voltammetry technique. *Bioelectrochemistry*. 73, 5-10.
46. Kachoosangi, R. T., Wildgoose, G. G., Compton, R. G. (2008). Sensitive adsorptive stripping voltammetric determination of paracetamol at multiwalled carbon nanotube modified basal plane pyrolytic graphite electrode. *Anal. Chim. Acta*. 618, 54-60.
47. Chu, Q. C., Jiang, L. M., An, X. H., Ye, J. N. (2008). Rapid determination of acetaminophen and p-aminophenol in pharmaceutical formulations using miniaturized capillary electrophoresis with amperometric detection. *Anal. Chim. Acta*. 606, 246-251.
48. Li, M. Q. and Jing, L. H. (2007). Electrochemical behavior of acetaminophen and its detection on the PANI-MWCNTs composite modified electrode. *Electrochim. Acta*. 52, 3250-3257.
49. Baranowska, I. and Koper, M. (2009). The preliminary studies of electrochemical behavior of paracetamol and its metabolites on glassy carbon electrode by voltammetric methods. *Electroanalysis*. 21, 1194-1199.
50. Norouzi, P., Dousty, F., Ganjali, M. R., Daneshgar, P. (2009). Dysprosium nanowire modified carbon paste electrode for the simultaneous determination of naproxen and paracetamol: Application in pharmaceutical formulation and biological fluid. *Int. J. Electrochem. Sci*. 4, 1373-1386.
51. Skeika, T., de Faria, M. F., Nagata, N., Pessoa, C. A. (2008). Simultaneous voltammetric determination of dipyrone and paracetamol with carbon paste electrode and multivariate calibration methodology. *J. Braz. Chem. Soc*. 19, 762-768.
52. Su, W. Y. and Cheng, S. H. (2010). Electrochemical oxidation and sensitive determination of acetaminophen in pharmaceuticals at poly (3,4-

- ethylenedioxythiophene)-modified screen-printed electrodes. *Electroanalysis*. 22, 707-714.
53. Quintino, M. S. M., Araki, K., Toma, H. E., Angnes, L. (2002). Batch injection analysis utilizing modified electrodes with tetra-ruthenated porphyrin films for acetaminophen quantification. *Electroanalysis*. 14, 1629-1634.
54. Wang, S. F., Xie, F., Hu, R. F. (2007). Carbon-coated nickel magnetic nanoparticles modified electrodes as a sensor for determination of acetaminophen. *Sensors Actuators B*. 123, 495-500.
55. Zen, J. M. and Ting, Y. S. (1997). Simultaneous determination of caffeine and acetaminophen in drug formulations by square-wave voltammetry using a chemically modified electrode, *Anal. Chim. Acta*. 342, 175-180.
56. Xu, Z. M., Yue, Q., Zhuang, Z. J., Xiao, D. (2009). Flow injection amperometric determination of acetaminophen at a gold nanoparticle modified carbon paste electrode. *Microchim. Acta*. 164, 387-393.
57. Teixeira, M. F. S., Marcolino, L. H., Fatibello, O. *et al.* (2009). Determination of analgesics (dipyron and acetaminophen) in pharmaceutical preparations by cyclic voltammetry at a copper (II) hexacyanoferrate(III) modified carbon paste electrode. *Curr. Anal. Chem.* 5, 303-310.
58. Cervini, P. and Cavalheiro, E. T. G. (2008). Determination of paracetamol at a graphite polyurethane composite electrode as an amperometric flow detector. *J. Braz. Chem. Soc.* 19, 836-841.
59. Safavi, A., Maleki, N., Moradlou, O. (2008). A selective and sensitive method for simultaneous determination of traces of paracetamol and p-aminophenol in pharmaceuticals using carbon ionic liquid electrode. *Electroanalysis*. 20, 2158-2162.
60. Gomez-Caballero, A., Goicolea, M. A., Barrio, R. J. (2005). Paracetamol voltammetric microsensors based on electro copolymerized-molecularly imprinted film modified carbon fiber microelectrodes. *Analyst*. 130, 1012-1018.
61. Cui, X. P., Hong, L., Lin, X. Q. (2002). Electrochemical preparation, characterization and application of electrodes modified with hybrid hexacyanoferrates of copper and cobalt. *J. Electroanal. Chem.* 526, 115-124.

62. Zidan, M., Tee, T. W., Abdullah, A. H. *et al.* (2011). Electrochemical oxidation of paracetamol mediated by nanoparticles bismuth oxide modified glassy carbon electrode. *Int. J. Electrochem. Sci.* 6, 279-288.
63. Fan, Y., Liu, J. -H., Lu, H. -T., Zhang, Q. (2011). Electrochemical behavior and voltammetric determination of paracetamol on Nafion/TiO<sub>2</sub>-graphene modified glassy carbon electrode. *Colloids and Surfaces B: Interfaces.* 85, 289-292.
64. Ogata, C., Koinuma, M., Hatakeyama, K. *et al.* (2014). Metal Permeation into Multi-layered Graphene Oxide. *Science.* 4, 3647.
65. Pokpas, K., Zbeda, S., Jahed, N. *et al.* (2014). Electrochemically Reduced Graphene Oxide Pencil-Graphite *in situ* Plated Bismuth-film Electrode for the Determination of Trace Metals by Anodic Stripping Voltammetry. *Int. J. Electrochem. Sci.* 9, 736-759.
66. Hirsch, A. (2010). The era of carbon allotropes. *Nat. Mater.* 9, 868-870.
67. Karfunkel, H. R. and Dressler, T. (1992). New hypothetical carbon allotropes of remarkable stability estimated by MNDO solid-state SCF computations. *J. Amer. Chem. Soc.* 114, 2285-2288.
68. Diederich, F. and Rubin, Y. (1992). Synthetic Approaches toward Molecular and Polymeric Carbon Allotropes. *Angew. Chem. Int. Ed.* 31, 1101-1123.
69. Pierson, H. O. (2012). Handbook of carbon, graphite, diamonds, and fullerenes: processing, properties, and applications.
70. Kroto, H. W., Heath, J. R., O'Brien, S. C., Curl, R. F., Smally, R. E. (1985). C<sub>60</sub>: Buckminsterfullerene. *Nature.* 318, 162-163.
71. Iijima, S. (1991). Helical microtubules of graphitic carbon. *Nature.* **354** (6348): 56-58.
72. Harris, P. J. F. (1999). Carbon nanotubes and related structures- New Materials for the Twenty-First Century. *Cambridge Press.* Cambridge, UK.
73. Al-Nafiey, A. K. H. (2016). Reduced graphene oxide-based nanocomposites: Synthesis, characterization, and application. Lille.
74. Shrantberg, A. A., Hudgins, R. R., Guiterrez, R. *et al.* (1999). Ball-and-chain dimers from hot fullerene plasma. *J. Phys. Chem. A.* **103** (27): 5275-5284.
75. Nievengarten, J. -F. and Bonifazi, D. (2014). Fullerenes and Other Carbon-Rich Nanostructures. *Springer.*

76. Kroto, H. W., Petrukhina, M. A., Scott, L. T. (2011). Fragments of fullerenes and carbon nanotubes: designed synthesis, unusual reactions, and coordination chemistry. John Wiley & Sons.
77. Saito, R., Dresselhaus, M. S., Dresselhaus, G. (1998). Physical properties of Carbon Nanotubes. *Imperial College Press*. pp. 259.
78. Lazzeri, M. and Barreiro, A. (2014). Carbon-Based Nanoscience. *Elements*. **10** (6): 447-452.
79. Chehren Chelgani, S., Rudolph, M., Kratzch, R. *et al.* (2016). A Review of Graphite Beneficiation Techniques. *Mineral Processing and Extractive Metallurgy Review*. **37** (1): 58-68.
80. Seabel, M. C. and Martins, J. L. (1992). Energetics interplanar binding in graphite. *Phys. Rev. B*. **46**, 7185-7188.
81. Ponnamma, D., Guo, Q., Krupa, I. *et al.* (2015). Graphene and graphitic derivative filled polymer composites as potential sensors. *Phys. Chem. Chem. Phys.*
82. Novoselov, K. S., Geim, A. K., Morozov, S. V. *et al.* (2004). Electric field in atomically thin carbon films. *Science*. **306** (5696): 666-669.
83. Johra, F. T., Lee, J. -W., Jung, W. -G. (2014). Facile and safe graphene preparation on solution-based platform. **20**, 2883-2887.
84. Bolotin, K. I., Sikes, K. J., Jiang, Z. *et al.* (2008). Ultrahigh electron mobility in suspended graphene. *Solid State Commun.* **146**, 351.
85. Morozov, S. V., Novoselov, K. S., Katsnelson, M. I. *et al.* (2008). Giant Intrinsic Carrier Mobilities in Graphene and Its Bilayer. *Phys. Rev. Lett.* **100**, 016602.
86. Lee, C., Wei, X. D., Kysar, J. W. *et al.* (2008). Measurement of the elastic properties and intrinsic strength of monolayer graphene. *Hone. Science*. **321**, 385.
87. Balandin, A. A., Ghosh, S., Bao, W. Z. *et al.* (2008). Superior Thermal Conductivity of Single-Layer Graphene. *Nano. Lett.* **8**, 902.
88. Nair, R. R., Grigorenko, A. N., Novoselov, K. S. *et al.* (2008). Fine structure constant defines visual transparency of graphene. *Science*. **320**, 1308.
89. Geim, A. K. and Novoselov, K. S. (2007). The rise of graphene. *Nat. Mater.* **6** (3): 183-191.

90. Cai, W., Zhu, Y., Li, X. *et al.* (2009). Large area few-layer graphene/graphite films as transparent thin conducting electrodes. *Appl. Phys. Lett.* **95**, 123115.
91. Li, X., Zhu, Y., Cai, W. *et al.* (2009). Transfer of Large-Area Graphene Films for High-Performance Transparent Conductive Electrodes. *Nano. Lett.* **9**, 4359.
92. Cooper, D. R., D'Anjou, B., Ghattamaneni, M. I. *et al.* (2012). Experimental Review of Graphene. *Review Article.* **2**.
93. Wallace, P. R. (1947). The band theory of graphite. *Phys. Rev.* **71** (9): 622-634.
94. Rao, C. N. R., Subrahmanyam, K. S., Matte, H. S. S. R. *et al.* (2011). Graphene: Synthesis, functionalization, and properties. *Modern Physics Letters.* **25** (7): 47-451.
95. Sharma, K. L. (2014). Graphene Nanomaterials. *Momentum Press, LLC.* New York, NY. pp. 159-176.
96. Dervishi *et al.* (2012). Few-layer nano-graphene structures with large surface areas synthesized on a multifunctional Fe: Mo: MgO catalyst system. *J. Mater. Sci.* **47** (4): 1910-1919.
97. Huang, S., Weis, J. E., Costa, S. *et al.* (2015). Properties of Carbon: An Overview-Electrochemistry of Carbon Electrodes. *Wiley-VCH Verlag GmbH & Co.* Weinheim, Germany. pp. 2-5.
98. Nezich, D. and Palacios, T. (2009). Graphene frequency multipliers. *Electron Device Lett.* **30** (5): 547-549.
99. Wang, H., Hsu, A., Wu, J. *et al.* (2010). Graphene-based ambipolar RF mixers. *Electron Device Lett.* **31** (9): 906-908.
100. Ci, L. Song, L., Jin, C. *et al.* (2010). Atomic layers of hybridized boron nitride and graphene domains. *Nat. Mater.* **9** (5): 430-435.
101. Reddy, A. L. M., Srivastava, A., Gowda, S. R. *et al.* (2010). Synthesis of nitrogen-doped graphene films for lithium battery application. *ACS Nano.* **4** (11): 6337-6342.
102. Yoo, J. J., Balakrishnan, K., Huang, J. *et al.* (2011). Ultrathin planar graphene supercapacitors. *Nano Lett.* **11** (4): 1423-1427.
103. Luo, X. Qiu, T., Lu, W. *et al.* 2013). Plasmons in graphene: recent process and applications. *Mater. Sci. Eng.* **74** (11): 351-376.
104. Grigorenko, A. N., Polini, M., Novoselov, K. S. (2012). Graphene plasmonics. *Nat. Photonics.* **6** (11): 749-758.

105. Abedmpour, S. H., Vignale, G., Principi, A. *et al.* (2011). Drude weight, plasmon dispersion, and ac conductivity in doped graphene sheets. *Phys. Rev. B.* **84** (4): 045429.
106. Polini, M., Asgari, R., Borghi, G. *et al.* (2008). Plasmons and the spectral function of graphene. *Phys. Rev. B.* **77** (8): 081411.
107. Hwang, E. H. and Das Sarma, S. (2007). Dielectric function, screening, and plasmons in two-dimensional graphene. *Phys. Rev. B.* **75** (20): 205418.
108. Wunsch, B., Stauber, T., Sols, F. *et al.* (2006). Dynamical polarization of graphene at finite doping. *New. J. Phys.* **8** (12): 318.
109. Fei, Z., Rodin, A. S., Andreev, G. O. *et al.* (2012). Gate-tuning of graphene plasmons revealed by infrared nano-imaging. *Nature.* **487** (7405): 82-85.
110. Ju, L., Geng, B., Horng, J. *et al.* (2011). Graphene plasmonics for tunable terahertz metamaterials. *Nat. Nanotechnol.* **6** (10): 630-634.
111. Bao, Q. and Loh, K. P. (2012). Graphene photonics, plasmonics, and broadband optoelectronic devices. *ACS Nano.* **6** (5): 3677-3694.
112. Mak, K. F., Sfeir, M. Y., Wu, Y. *et al.* (2008). Measurement of optical conductivity of graphene. *Phys. Rev. Lett.* **101** (19): 196405.
113. Mak, K. F., Ju, L., Wang, F. *et al.* (2012). Optical spectroscopy of graphene: from the far infrared to the ultraviolet. *Solid State Commun.* **152** (15): 1341-1349.
114. Eberlein, T., Bangert, U., Nair, R. *et al.* (2008). Plasmon spectroscopy of free-standing graphene films. *Phys. Rev. B.* **77** (23): 233406.
115. Chen, J., Badioli, M., Alonso-Gonzalez, P. *et al.* (2012). Optical nano-imaging of gate-tunable graphene plasmons. *Nature.* **487** (7405): 77-81.
116. Yan, H., Li, X., Chandra, B. *et al.* (2012). Tunable infrared plasmonic devices using graphene/insulator stacks. *Nat. Nanotechnol.* **7** (5): 330-334.
117. Jung, N., Kim, N., Jockusch, S. *et al.* (2009). Charge transfer chemical doping of few layer graphenes: charge distribution and bandgap formation. *Nano. Lett.* **9** (12): 4133-4137.
118. Zhang, W., Lin, C. -T., Liu, K. -K. *et al.* (2011). Opening an electrical bandgap of bilayer graphene with molecular doping. *ACS Nano.* **5** (9): 7517-7524.

119. Das, S., Pisana, S., Chakraborty, B. *et al.* (2008). Monitoring dopants by Raman scattering in electrochemically top-gated graphene transistor. *Nat. Nanotechnol.* **3** (4): 210-215.
120. Kalbac, M., Farhat, H., Kong, J. *et al.* (2011). Raman spectroscopy and *in situ* Raman spectroelectrochemistry of bilayer  $^{12}\text{C}/^{13}\text{C}$  graphene. *Nano. Lett.* **11** (5): 1957-1963.
121. Frank, O., Dresselhaus, M. S., Kalbac, M. (2015). Raman spectroscopy and *in situ* Raman spectroelectrochemistry of isotopically engineered graphene systems. *Acc. Chem. Res.* **48** (1): 111-118.
122. Kalbac, M. S., Kong, J., Dresselhaus, M. S. (2012). Raman spectroscopy as a tool to address individual graphene layers in few-layer graphene. *J. Phys. Chem. C.* **116** (35): 19046-19050.
123. Kalbac, M. S., Reina-Cecco, A., Farhat, H. *et al.* (2010). The influence of strong electron and hole doping on the Raman intensity of chemical vapour deposition graphene. *ACS Nano.* **4** (10): 6055-6063.
124. Freitag, M., Steiner, M., Martin, Y. *et al.* (2009). Energy dissipation in graphene field-effect transistors. *Nano. Lett.* **9** (5): 1883-1888.
125. Malard, L. M., Pimenta, M. A., Dresselhaus, G. *et al.* (2009). Raman spectroscopy in graphene. *Phys. Rep.* **473** (5-6): 51-87.
126. Yan, J., Zhang, Y., Kim, P. *et al.* (2007). Electric field effect tuning of electron-phonon coupling in graphene. *Phys. Rev. Lett.* **98** (16): 166802.
127. Meyer, J. C., Kurasch, S., Park, H. J. *et al.* (2011). Experimental analysis of charge redistribution due to chemical bonding by high-resolution transmission electron microscopy. *Nat. Mater.* **10** (3): 209-215.
128. Ambrosi, A., Chun Kiang, C., Bonanni, A. *et al.* (2014). Electrochemistry of Graphene and Related Materials. *Chem. Rev.* **114**, 7150-7188.
129. Novoselov, K. S., Fal'ko, V. I., Colombo, L. *et al.* (2012). A roadmap for graphene. *Nature.* **490**, 192-200.
130. Novoselov, K. S., Jiang, D., Schedin, F. *et al.* (2005). Two-dimensional electron and hole gases at the surface of graphite. *Proc. Natl. Acad. Sci.* **102**, 10451.
131. Wu, J. S., Pisula, W., Mullen, K. (2007). Graphenes as Potential Material for Electronics. *Chem. Rev.* **107**, 718.

132. Guinea, F., Katsnelson, M. I., Geim, A. K. (2009). Energy gaps and a zero-field quantum Hall effect in graphene by strain engineering. *Nat. Phys.* **6**, 30.
133. Balandin, A. A., Ghosh, S., Bao, W. Z. *et al.* (2008). Superior thermal conductivity of single-layer graphene. *Nano. Lett.* **8** (3): 902-907.
134. Geim, A. K. (2009). Graphene: Status and Prospects. *Science*. 324, 1530.
135. Banks, C, Moore, R., Davies, T. *et al.* (2004). Investigation of modified basal plane pyrolytic graphite electrodes: definitive evidence for the electrocatalytic properties of the ends of carbon nanotubes. *Chem. Commun.* 1804.
136. Li, W., Tan, C., Lowe, M. *et al.* (2011). Electrochemistry of Individual Monolayer Graphene Sheets. *ACS Nano*. **5** (3): 2264-2270.
137. Valota, A. T., Kinloch, I. A., Novoselov, K. S. *et al.* (2011). Electrochemical Behavior of Monolayer and Bilayer Graphene. *ACS Nano*. **5**, 8809-8815.
138. Hernandez, Y., Nicolosi, V., Lotya, M. *et al.* (2008). High-yield production of graphene by liquid-phase exfoliation of graphite. *Nat. Nanotechnol.* **3** (9): 563-568.
139. Hernandez, Y., Lotya, M., Rickard, D. *et al.* (2010). Measurement of Multicomponent Solubility Parameters for Graphene Facilitates Solvent Discovery. *Langmuir*. **26** (5): 3208-3213.
140. Blake, P., Brimicombe, P. D., Nair, R. R. *et al.* (2008). Graphene-Based Liquid Crystal Device. *Nano. Lett.* **8** (6): 1704-1708.
141. Green, A. and Hersam, M. (2009). Solution Phase Production of Graphene with Controlled Thickness via Density Differentiation. *Nano. Lett.* **9** (12): 4031-4036.
142. Wang, L.; Ambrosi, A.; Pumera, M. (2013). Metal-Free Catalytic Oxygen Reduction Reaction on Heteroatom-Doped Graphene is Caused by Trace Metal Impurities. *Angew. Chem., Int. Ed.* **52**, 13818– 13821.
143. Jnioui, A., Metrot, A., Storck, A. (1982). Electrochemical production of graphite salts using a 3-dimensional electrode of graphite particles. *Electrochim. Acta.* **27**, 1247-1252.
144. Takada, Y. and Fujii, R. (1985). The Electrochemical Formation of Graphite Intercalation Compound in  $\gamma$ -Butyrolactone. *Tanso*. 110.
145. Noel, M., Santhanam, R., Flora, M. F. (1994). Effect of polypyrrole film on the stability and electrochemical activity of fluoride-based graphite intercalation compounds in HF media. *J. Appl. Electrochem.* **24**, 455.

146. Takenaka, H., Kawaguchi, M., Lerner, M. *et al.* (1987). Synthesis and characterization of graphite fluorides by electrochemical fluorination in aqueous and anhydride hydrogen fluoride. *J. Chem. Soc. Chem. Commun.* 1431.
147. Inagaki, M., Iwashita, N., Wang, Z. *et al.* (1988). Electrochemical synthesis of graphite intercalation compounds with nickel and hydroxides. *Synth. Met.* **26** (1): 41-47.
148. Low, C. T. J., Walsh, F. C., Chakrabarti, M. H. *et al.* (2013). Electrochemical approaches to the production of graphene flakes and their potential applications. *Carbon.* 54, 1.
149. Wang, G., Wang, B., Park, J. *et al.* (2009). Highly efficient and large-scale synthesis of graphene by electrolytic exfoliation. *Carbon.* 47, 3242.
150. Su, C. -Y., Lu, A. -Y., Xu, Y. *et al.* (2011). High-Quality Thin Graphene Films from Fast Electrochemical Exfoliation. *ACS Nano.* 5, 2332.
151. Alanyalioglu, M., Jose Segura, J., Oro-Sole, J. *et al.* (2012). The synthesis of graphene sheets with controlled thickness and order using surfactant-assisted electrochemical processes. *Carbon.* 50, 142.
152. Brodie, B. C. (1859). On the Atomic Weight of Graphite. *Philos. Trans. R. Soc. Lon.* 149, 249-259.
153. Staudenmaier, L. (1898). Verfahren zur Darstellung der Graphitsäure. *Ber. Dtsch. Chem. Ges.* 31, 1481.
154. Hoffman, U. and König, E. Z. (1937). Untersuchungen über Graphitoxyd. *Anorg. Allg. Chem.* 234, 311.
155. Hummers, W. S. and Offeman, R. E. (1958). Preparation of Graphitic Oxide. *J. Am. Chem. Soc.* **80** (6): 1339.
156. Marcano, D., Kosynkin, D., Berlin, J. *et al.* (2010). Improved Synthesis of Graphene Oxide. *ACS Nano.* **4** (8): 4806-4814.
157. Dreyer, D. R., Park, S., Bielawski, C. W. *et al.* (2010). The chemistry of graphene oxide. *Chem. Soc. Rev.* 39, 228.
158. Zhu, Y. W., Murali, S., Cai, W. W. *et al.* (2010). Graphene and Graphene Oxide: Synthesis, Properties, and Applications. *Adv. Mater.* **22** (35): 3906-3935.
159. Yang, X. Y., Dou, X., Rouhanipour, A. *et al.* (2008). Two-dimensional graphene nanoribbons. *J. Am. Chem. Soc.* 130, 4216-4217.

160. Cai, J. M., Ruffieux, P., Jaafar, R. *et al.* (2010). Atomically Precise Bottom-Up Fabrication of Graphene Nanoribbons. *Nature*. **466** (7305): 470-473.
161. Chen, L., Hernandez, Y., Feng, X. *et al.* (2012). From Nanographene and Graphene Nanoribbons to Graphene Sheets: Chemical Synthesis. *Angew. Chem. Int. Ed.* **51** (31): 7640-7654.
162. Berger, C., Song, Z. M., Li, T. B. *et al.* (2004). Ultrathin epitaxial graphite: 2D electron gas properties and a route toward graphene-based nanoelectronics. *J. Phys. Chem. B.* **108**, 19912.
163. Berger, C., Song, Z. M., Li, X. *et al.* (2006). Electronic Confinement and Coherence in Patterned Epitaxial Graphene. *Science*. **312** (5777): 1191-1196.
164. Emtsev, K. V., Bostwick, A., Horn, K. *et al.* (2009). Towards Wafer-Size Graphene Layers by Atmospheric Pressure Graphitization of Silicon Carbide. *Nat. Mater.* **8** (3): 203-207.
165. de Heer, W. A., Berger, C., Wu, X. S. *et al.* (2007). Epitaxial graphene. *Solid State Commun.* **143**, 92-100.
166. Lim, C. X., Hoh, H. Y., Ang, P. K. *et al.* (2010). Direct Voltammetric Detection of DNA and pH Sensing on Epitaxial Graphene: An Insight into the Role of Oxygenated Defects. *Anal. Chem.* **82** (17): 7387-7393.
167. Farmer, D., Chiu, H. -Y., Lin, Y. -M. *et al.* (2009). Utilization of a Buffered Dielectric to Achieve High Field-Effect Carrier Mobility in Graphene Transistors. *Nano. Lett.* **9** (12): 4474-4478.
168. Ambrosi, A. and Pumera, M. (2013). Electrochemistry at CVD Grown Multilayer Graphene Transferred onto Flexible Substrates. *J. Phys. Chem. C.* **117** (5): 2053-2058.
169. Chen, S., Brown, L., Levendorf, M. *et al.* (2011). Oxidation Resistance of Graphene-Coated Cu and Cu/Ni Alloy. *ACS Nano.* **5** (2): 1321-1327.
170. Prasai, D., Turbequia, J. C., Harl, R. R. *et al.* (2012). Correction to Graphene: Corrosion-Inhibiting Coating. *ACS Nano.* **6**, 1102.
171. Rafiee, J., Mi, X., Gullapalli, H. *et al.* (2012). Wetting Transparency of Graphene. *Nat. Mater.* **11** (3): 217-222.

172. Yudasaka, M., Kikushi, R., Matsui, T. *et al.* (1995). Specific conditions for Ni catalyzed carbon nanotube growth by chemical vapour deposition. *Appl. Phys. Lett.* **67** (17): 2477-2479.
173. Sutter, P. W., Flege, J. –L., Sutter, E. A. (2008). Epitaxial Graphene on Ruthenium. *Nat. Mater.* **7** (5): 406-411.
174. Roumen, V., Alexander, M., Roumen, H. P. *et al.* (2010). *Nanotechnology.* 21, 095602.
175. Coraux, J., NDiaye, A. T., Busse, C. *et al.* (2008). Structure of epitaxial graphene on Ir(111). *Nano. Lett.* **8**, 565.
176. Reina, A., Jia, X., Ho, J. *et al.* (2009). Large area, few-layer graphene films on arbitrary substrates by chemical vapour deposition. *Nano. Lett.* **9** (1): 30-35.
177. Li, X., Cai, W., An, J. *et al.* (2009). Large-Area Synthesis of High-Quality and Uniform Graphene Films on Copper Foils. *Science.* **324** (5935): 1312-1314.
178. Kim, K. S., Zhao, Y., Jang, H. *et al.* (2009). Large-scale pattern growth of graphene films for stretchable transparent electrodes. *Nature.* **457**, 706-710.
179. Bae, S., Kim, H., Lee, Y. *et al.* (2010). Roll-to-roll production of 30-inch graphene films for transparent electrodes. *Nat. Nanotechnol.* **5**, 574-578.
180. Li, X., Magnuson, C. W., Venugopal, A. *et al.* (2011). Large-Area Graphene Single Crystals Grown by Low-Pressure Chemical Vapor Deposition of Methane on Copper. *J. Am. Chem. Soc.* **133** (9): 2816-2819.
181. Sun, Z., Yan, Z., Yao, J. *et al.* (2010). Growth of graphene from solid carbon sources. *Nature.* **468**, 549-552.
182. Ambrosi, A., Bonanni, A., Sofer, Z. *et al.* (2013). Large-scale quantification of CVD graphene surface coverage. *Nanoscale.* **5**, 2379.
183. Brownson, D. A. C. and Banks, C. E. (2012). Limitations of CVD graphene when utilised towards the sensing of heavy metals. *RSC Adv.* **2**, 5385-5389.
184. Brownson, D. A. C. and Banks, C. E. (2011). CVD graphene electrochemistry: the role of graphitic islands. *Phys. Chem. Chem. Phys.* **13**, 15825.
185. Brownson, D. A. C., Gomez-Mingot, M., Banks, C. E. (2011). CVD graphene electrochemistry: biologically relevant molecules. *Phys. Chem. Phys. Chem.* **13**, 20284.

186. Çiplak, Z., Yildiz, N., Çalimli, A. (2014). Investigation of Graphene/Ag Nanocomposites Synthesis Parameters for Two Different Synthesis Methods. *Fullerenes, Nanotubes, and Carbon Nanostructures*. 23, 361-370.
187. Luceño-Sánchez, J. A., Maties, G., Gonzalez-Arellano, C., Diez-Pascual, A. M. (2019). Synthesis and Characterization of Graphene Oxide Derivatives via Functionalization Reaction with Hexamethylene Diisocyanate. 3, 8.
188. Manoratne, C. H., Rosa, S. R. D., Kottegoda, I. R. M. (2017). XRD-HTA, UV Visible, FTIR, and SEM Interpretation of Reduced Graphene Oxide Synthesized from High Purity Vein Graphite. *Mat. Sci. Res. India*. 14 (1): 19-30.
189. Wang, K., Ruan, J., Song, H., Zhang, J., Wo, Y., Guo, S., Cui, D. (2011). Biocompatibility of Graphene Oxide. *Nano Lett.* 6 (1): 1-8.
190. Szarbo, T., Berkesi, D., Dekany, I. (2005). DRIFT study of deuterium-exchanged graphite oxide. *Carbon*. 43, 3186-3189.
191. Diez-Pascual, A. M. and Diez-Vicente, A. L. (2016). Poly(propylene fumarate)/polyethylene glycol-modified graphene oxide nanocomposites for tissue engineering. *ACS Appl. Lett. Interfaces*. 8, 7902-17914.
192. Ferrari, A., Meyer, J., Scardaci, V. *et al.* (2006). Raman spectrum of graphene and graphene layers. *Phys. Rev. Lett.* 97 (18): 187401.
193. Piscanec, S., Lazzeri, M., Mauri, F. *et al.* (2004). Kohn anomalies and electron-phonon interactions in graphite. *Phys. Rev. Lett.* 93 (18): 185503.
194. Lee, J. E., Ahn, G., Shim, J. *et al.* (2012). Optical separation of mechanical strain from charge doping in graphene. *Nat. Commun.* 3, 1024.
195. Xu, J. Z., Chen, C., Wang, Y. *et al.* (2011). Graphene nanosheets and shear flow induced crystallization in isotactic polypropylene nanocomposites. *Macromolecules*. 44 (8): 2808-2818.
196. Gascho, J. L. S., Costa, S. F., Recco, A. A. C., Pezzin, S. H. (2019). Graphene Oxide Films Obtained by Vacuum Filtration: X-Ray Diffraction Evidence of Crystalline Reorganization. *J. Nanomater.* 1-12.
197. Shin, H. -J., Kim, K. K., Benayad, A. (2009). Efficient reduction of graphite oxide by sodium borohydride and its effect on electrical conductance. *Advanced Functional Materials*. 19 (12): 1987-1992.

198. Li, Z. Q., Lu, C. J., Xia, P., Zhou, Y., Luo, Z. (2007). X-ray diffraction patterns of graphite and turbostratic carbon. *Carbon*. **45** (8): 1686-1695.
199. Williams, D. B. and Carter, C. B. (1996). The transmission electron microscope. *Springer*.
200. Newbury, D. E., Joy, D. C., Echlin, P. *et al.* (2003). Scanning electron microscope and X-ray microanalysis. *Springer*.
201. Buchsteiner, A., Lerf, A., Pieper, J. (2006). Water dynamics in graphite oxide investigated with neutron scattering. *J. Phys. Chem. B*. **110** (45): 22328-22338.
202. Ogata, C., Koinuma, M., Hatakeyama, K. *et al.* (2014). Metal Permeation into Multi-layered Graphene Oxide. *Science*. **4**, 3647.
203. Chen, X. *et al.* (2011). Synthesis of “clean” and well-dispersive Pd nanoparticles with excellent electrocatalytic property on graphene oxide. *J. Am. Chem. Soc.* **133**, 3693-3695.
204. Zhu, C., Han, L., Hu, P. *et al.* (2012). *In situ* loading of well-dispersed gold nanoparticles on two-dimensional graphene oxide/SiO<sub>2</sub> composite nanosheets and their catalytic properties. *Nanoscale*. **4**, 1641-1646.
205. Dimiev, A. *et al.* (2011). Layer-by-layer removal graphene for device patterning. *Science*. **331**, 1168-1172.
206. Chen, D., Feng, H., Li, J. (2012). Graphene oxide: preparation, functionalization, and electrochemical applications. *Chem. Rev.* **112**, 6027-6053.
207. Koinuma, M. *et al.* (2012). Photochemical engineering of graphene oxide nanosheets. *J. Phys. Chem.* **116**, 19822-19827.
208. Matsumoto, Y. *et al.* (2013). Electrolytic graphene oxide and its electrochemical properties. *J. Electroanal. Chem.* **704**, 233-241.
209. Chan, K. T., Neaton, J. B., Cohen, M. L. (2008). First-principles study of metal adatom adsorption on graphene. *Phys. Rev. B*. **77**, 235430-235441.
210. Krasheninnikov, A. V., Lehtinen, P. O., Foster, A. S. *et al.* (2009). Embedding transition-metal atoms in graphene structure, bonding, and magnetism. *Phys. Rev. Lett.* **102**, 126807-126810.
211. Boukhvalov, D. W. and Katsnelson, M. I. (2009). Destruction of graphene by metal adatoms. *Appl. Phys. Lett.* **95**, 023109-023111.

212. Kan, E. -J., Xiang, H. J., Yang, J. *et al.* (2007). Electronic structure of Ti chains on semiconducting graphene nanoribbons: a first-principles study. *J. Chem. Phys.* **127**, 164706-164710.
213. Sevindi, H., Topsakal, M., Durgun, E. *et al.* (2008). Electronic and magnetic properties of 3<sup>rd</sup> transition-metal atom adsorbed graphene and graphene nanoribbons. *Phys. Rev. B.* **77**, 195434-195440.
214. Rigo, V.A., Martins, T. B., Silva, A. J. R. *et al.* (2009). Electronic, structural, and transport properties of Ni-doped graphene nanoribbons. *Phys. Rev. B.* 075435-07543.
215. Jensen, P., Blasé, X., Ordejon, P. (2004). First-principles study of gold adsorption and diffusion on graphite. *Surf. Sci.* **564**, 173-178.
216. Akola, J. and Hakkinen, H. (2006). Density of functional study of gold atoms and clusters on graphite (0001) surface with defects. *Phys. Rev. B.* **74**, 165404-165412.
217. Malola, S., Hakkinen, H., Koskinen, P. (2009). Gold in graphene: in-plane adsorption and diffusion. *Appl. Phys. Lett.* **94**, 043106-043108.
218. Brito, W. H. and Miwa, R. H. (2010). Adsorption and diffusion of gold adatoms on graphene nanoribbons: an *ab initio* study. *Phys. Rev. B.* **82**, 045417-045423.
219. Gan, Y., Sun, L., Banhart, F. (2008). One- and two-dimensional diffusion of metal atoms in graphene. *Small.* **4**, 587-591.
220. Anton, R. and Kreuzer, P. (2000). *In situ* TEM evaluation on the growth kinetics of Au particles on highly oriented pyrolytic graphite at elevated temperatures. *Phys. Rev. B.* **61**, 16077-16083.
221. Ji, Z., Shen, X., Zhu, G. *et al.* (2012). Reduced graphene oxide/ nickel nanocomposites: facile synthesis, magnetic, and catalytic properties. *J. Mater. Chem.* **22** (8): 3471.
222. Zhou, X. Huang, X., Qi, X. *et al.* (2009). *In situ* synthesis of metal nanoparticles on single-layer graphene oxide and reduced graphene oxide surfaces. *J. Phys. Chem. C.* **113** (5): 10842-10846.
223. Huang, X., Zhou, X., Wu, S. *et al.* (2010). Reduced Graphene Oxide-Templated Photochemical Synthesis and *in situ* Assembly of Au Nanodots to Orderly Patterned Au Nanodot Chains. *Small.* **6** (4): 513-516.

224. Hong, T. -K., Lee, D. W., Choi, H. J. *et al.* (2010). Transparent, flexible conducting hybrid multilayer thin films of multi-walled carbon nanotubes with graphene nanosheets. *ACS Nano*. **4** (7): 3861-3868.
225. Tung, V. C., Cheng, L. -M., Allen. M. J. *et al.* (2009). Low-temperature solution processing of graphene-carbon nanotube hybrid materials for high-performance transparent conductors. *Nano. Lett.* **9** (5): 1949-1955.
226. McCreery, R. L. (2008). Advanced Carbon Electrode Materials for Molecular Electrochemistry. *Chem. Rev.* **108** (7): 2646-2687.
227. Kawde, A. -N., Baig, N., Sajid, M. (2016). Graphite pencil electrodes as electrochemical sensors for environmental analysis: a review of features, developments, and applications. *RSC Adv.* **6**, 91325.
228. Teepo, S., Chumsaeng, P., Nethan, P. *et al.* (2012). *Int. J. Electrochem. Sci.* **7**, 4645-4656.
229. David, I. G., Badea, I. A., Radu, G. L. (2013). Disposable carbon electrodes as an alternative for the direct voltammetric determination of alkyl phenols from water samples. *Turk. J. Chem.* **37** (1): 91-100.
230. Aziz, M. A. and Kawde, A. N. (2016). Gold nanoparticle-modified graphite pencil electrode for the high-sensitivity detection of hydrazine. *Talanta*. **115**, 214-221.
231. Rana, A. and Kawde, A. N. (2016). Open-circuit Electrochemical Polymerization for the Sensitive Detection of Phenols. *Electroanalysis*. **28** (4): 898-902.
232. Galeano-Diaz, T., Guibertau-Cabanillas, A., Mora-Diez, N. *et al.* (2000). Rapid and sensitive determination of 4-nitrophenol, 3-methyl-4-nitrophenol, 4,6-dinitro-o-cresol, parathion-methyl, fenitrothion, and parathion-ethyl by liquid chromatography with electrochemical detection. *J. Agric. Food Chem.* **48** (10): 4508-4513.
233. Kawde, A. N. and Aziz, M. A. (2014). Porous Copper-Modified Graphite Pencil Electrode for the Amperometric Detection of 4-Nitrophenol. *Electroanalysis*. **26** (11): 2484-2490.
234. Asadpour-Zeynali, K. and Najafi-Marandi, P. (2011). Bismuth Modified Disposable Pencil-Lead Electrode for Simultaneous Determination of 2-Nitrophenol and 4-Nitrophenol by Net Analyte Signal Standard Addition Method. *Electroanalysis*. **23** (9): 2241-2247.

235. David, I. G., Popa, D. –E., Buleandra, M. (2017). Pencil Graphite Electrodes: A Versatile Tool in Electroanalysis. *Hindawi*. 1-22.
236. Kissinger, P. T. and Heineman, W. R. (1983). Cyclic Voltammetry. *J. Chem. Ed.* **60** (9): 703-706.
237. Chang, B. -Y. and Park, S. -M. (2010). Electrochemical Impedance Spectroscopy. *Annu. Rev. Anal. Chem.* **3**, 207-229.
238. Thomas, F. G. and Henze, G. (1932-1933). Introduction to Voltammetric Analysis: Theory and Practice. *CSIRO Publishing*. Collingwood, Australia. pp. 58-80.
239. Barendrecht, E. (1967). Electroanalytical Chemistry. A. J. Bard (Ed). *Marcel Decker*. New York. **2**, 53.
240. Brainina, K. Z. (1971). Film Stripping Voltammetry. *Talanta*. **18** (5): 513-539.
241. Duic, L., Szechter, S., Srinivasan, S. (1973). Microdetermination of lead in blood: A derivative pulse stripping voltammetric method. *J. Electroanal. Chem.* **41**, 89.
242. Bond, A. M., O'Donnell, T. A., Waugh, A. B. *et al.* (1970). *Anal. Chem.* **40**, 1168.
243. Wang, J. (1982). Anodic stripping voltammetry as an analytical tool. *Environmental Science and Technology*. **16**, 104-109.
244. Nürenberg, H. W. (1983). *Frezenius Z. Analytische Chemie*. **316**, 557.
245. Batley, G. E. and Florence, T. M. (1974). An evaluation and comparison of some techniques of anodic stripping voltammetry. *J. Electroanal. Chem.* **55**, 23.
246. Neeb, R. (1962). Inverse Polagraphie and Voltammetrie. *Angewandte Chemie. Verlag Chemie*. Weinheim. **74**, 203.
247. Colovos, G., Wilson, G. S., Moyers, J. L. (1974). Simultaneous determination of bromide and chloride by cathodic stripping voltammetry. *Anal. Chem.* **46** (8): 1051-1054.
248. Shane, I. and Perome, S. (1961). *Anal. Chem.* **33**, 325.
249. Geyer, R., Henze, G., Henze, J. (1966). *Wissenschaftliche Z. der Technischen Hochschule Leuna/Merseburg*. **8**, 98.
250. Wang, J. (1985). Stripping Analysis: Principles, Instrumentation, and Applications. *VCH Publishing*. Florida.
251. van der Berg, C. M. G. (1991). Potentials and potentialities of cathodic stripping voltammetry of trace elements in natural waters. *Analytical Chimica Acta*. **250**, 265-276.

252. Kalvoda, R. (1994). Instrumentation in Analytical Chemistry. Zyka, J. (Ed). *Ellis Horwood*. New York. 3.
253. Wang, J. (1985). Instrumentation in Analytical Chemistry. *American Laboratory*. 17, 41.
254. Novotny, L. (1989). Instrumental Methods in Analytical Chemistry. Zyka, J. (Ed). *State Publishing House*. Prague.
255. Galpaya, D., Wang, M., George, G. *et al.* (2014). Preparation of graphene oxide/epoxy nanocomposites with significantly improved mechanical properties. *J. Appl. Phys.* 116, 053518.
256. Bera, M., Chandravati, Gupta, P. *et al.* (2018). Facile One-Pot Synthesis of Graphene Oxide by Sonication Assisted Mechanochemical Approach and its Surface Chemistry. *J. Nanosci. Nanotechnol.* **18** (2): 902-912.
257. Paulchamy, B., Arthi, G., Lignesh, B. D. (2015). A simple approach to stepwise synthesis of graphene oxide nanomaterial. *J. Nanomed. Nanotechnol.* 6, 2.
258. Fu, C., Zhao, G., Zhang, H. *et al.* (2013). Evaluation and Characterization of Reduced Graphene Oxide Nanosheets as Anode Materials for Lithium-Ion Batteries. *Int. Electrochem. Sci.* 8, 6269-6980.
259. Ni, Z., Wang, Y., Yu, T. *et al.* (2008). Raman spectroscopy and imaging of graphene. *Nano. Research.* **1** (4): 273-291.
260. Stankovich, S., Dikin, D. A., Piner, R. D. *et al.* (2007). Synthesis of graphene-based nanosheets via chemical reduction of exfoliated graphite oxide. *Carbon.* **45** (7): 1558-1565.
261. Ferrari, A. C. (2007). Raman spectroscopy of graphene and graphite: disorder, electron-phonon coupling, doping, and non-adiabatic effects. *Solid State. Commun.* **143** (1): 47-57.
262. Tuinstra, F. and Koenig, J. L. (1970). Raman spectrum of graphite. *J. Chem. Phys.* **53** (3): 1126-1130.
263. Lucchese, M. M., Stavale, F., Ferreira, E. M. *et al.* (2010). Quantifying ion-induced defects and Raman relaxation length in graphene. *Carbon.* **48** (5): 1592-1597.
264. Chen, J., Yao, B., Li, C. *et al.* (2013). An improved Hummers method for eco-friendly synthesis of graphene oxide. *Carbon.* 64, 225-229.

265. Song, J., Wang, X., Chang, C. T. *et al.* (2014). Preparation and Characterization of Graphene Oxide. *J. Nanomater.* 2014, 1.
266. Cesarino, I., Cincotto, F. H., Machado, S. A. S. (2015). A synergistic combination of reduced graphene oxide and antimony nanoparticles for estriol hormone detection. *Sensors and Actuators. B.* 210, 453-459.
267. Chenxing, G., Wang, J., Chen, X. *et al.* (2019). Construction of a Biosensor Based on a Combination of Cytochrome *c*, Graphene, and Gold Nanoparticles. *Sensors.* 19, 40.
268. Amin, H. M. A., El-Kady, M. F., Atta, N. F. *et al.* (2018). Gold Nanoparticles Decorated Graphene as a High-Performance Sensor for Determination of Trace Hydrazine Levels in Water. *Electroanalysis.* 30, 1-11.
269. Rhieu, S. Y. and VytasReipa (2015). Tuning the Size of Gold Nanoparticles with Repetitive Oxidation-Reduction Cycles. *Am. J. Nanomater.* 3 (1): 15-21.
270. Unknown. Cyclic Voltammetry Study of Ferricyanide/Ferrocyanide Redox Couple.
271. Zaib, M. and Athar, M. M. (2015). Electrochemical Evaluation of *Phanerocheaete Chrysosporium* Based Carbon Paste Electrode with Potassium Ferricyanide Redox System. *Int. J. Electrochem.* 10, 6690-6702.
272. Li, K., Li, Y., Wang, L. *et al.* (2015). Study the voltammetric behaviour of 10-Hydroxycamptothecin and its sensitive determination at electrochemically reduced graphene modified glassy carbon electrode. *Arabian. J. Chem.* 1-8.
273. Aristov, N. and Habeskot, A. (2015). Cyclic Voltammetry- A Versatile Electrochemical Method: Investigating Electron Transfer Processes. *World. J. Chem. Ed.* 3 (5): 115-119.
274. Frayer, S. *et al.* (2002). Synthesis Routes for Enhanced Electrochemical Performance. *Electrochemical and Solid State Letters.* 5 (10): A231-A233.
275. Ramalakshmi, N., Muthukumar, S., Marichamy, B. (2013). Preparation and Characterization of 4-hydroxybenzylidencarbamide-CTAB modified Glassy carbon Electrode by using  $[\text{Fe}(\text{CN})_6]^{4-}/[\text{Fe}(\text{CN})_6]^{3-}$  redox system. *Int. J. Chem. Phys. Sci.* 2 (4): 16-24.
276. Masek, A., Chrzescijanska, E., Zaborski, M. (2014). Electrooxidation of morin hydrate at a Pt electrode studied by cyclic voltammetry. 148, 18-23.

277. Karikalan, N., Karthik, R., Chen, S. –M. *et al.* (2016). Electrochemical properties of the acetaminophen on the screen-printed electrode towards the high performance practical sensor applications. *J. Colloid and Interface Science.* 483, 109-117.
278. Skeika, T., de Faria, M. F., Nagata, N. *et al.* (2008). Simultaneous voltammetric determination of dypirone and paracetamol with carbon paste electrode and multivariate calibration methodology. *J. Brazilian. Chem. Soc.* **19** (4): 762.
279. Săndulescu, R., Mirel, S., Oprean, R. (2000). The development of spectrophotometric and electron analytical methods for ascorbic acid and acetaminophen and their applications in the analysis of effervescence dosage forms. *J. Pharm. Biomed. Anal.* 23, 77-87.
280. Tefera, M., Geto, A., Tessema, M. *et al.* (2016). Simultaneous determination of caffeine and paracetamol by square wave voltammetry at poly(4-amino-3-hydroxynaphthalene sulfonic acid)-modified glassy carbon electrode. *Food Chemistry.* 210, 156-162.
281. Tanuja, S. B., Kumara Swamy, B. E., VasantakumarPai, K. (2017). Electrochemical determination of paracetamol in presence of folic acid at nevirapine modified carbon paste electrode: A cyclic voltammetric study. *J. Electroanal. Chem.* 798, 17-23.
282. Yin, H., Ma, Q., Zhou, Y. *et al.* (2010). Electrochemical behaviour and voltammetric determination of 4-aminophenol based on graphene-chitosan composite film modified glassy carbon electrode. *Electrochim. Acta.* **55** (23): 7102-7108.
283. Kang, X., Wang, J., Wu, H. *et al.* (2010). A graphene-based electrochemical sensor for sensitive detection of paracetamol. *Talanta.* **81** (3): 754-759.
284. Lourenção, B. C., Medeiros, R. A., Rocha-Filho, R. C. *et al.* (2009). Simultaneous determination of paracetamol and caffeine in pharmaceutical formulations using a boron-doped diamond electrode. *Talanta.* **78** (3): 748-752.
285. Kachoosangi, R. T., Wildgoose, G. G., Compton, R. G. (2008). Sensitive adsorptive stripping voltammetric determination of paracetamol at multiwalled carbon nanotube modified basal plane pyrolytic graphite electrode. *Anal. Chim. Acta.* **618** (1): 54-60.
286. Li, M. and Jing, L. (2007). Electrochemical behaviour of acetaminophen and its detection on the PANI-MWCNTs composite modified electrode. *Electrochim. Acta.* **52** (9): 3250-3257.
287. Khaskheli, A. R., Fischerb, J., Barek, J. *et al.* (2013). Differential pulse voltammetric determination of paracetamol in tablet and urine samples at a micro-crystalline natural

- graphite-polystyrene composite film modified electrode. *Electrochim. Acta.* **101** (1): 238-242.
288. Han, J., Liu, Y., Guo, R. (2009). Facile synthesis of stable gold nanoparticles and their unexpected excellent catalytic activity for Suzuki-Miyaura cross-coupling reaction in water. *J. Am. Chem. Soc.* 131, 2060-2061.
289. Pourke, L. D. and Nugent, P. F. (1997). The Electrochemistry of Gold: I The Redox Behaviour of the Metal in Aqueous Media. *Gold Bulletin.* **30** (2): 44.





UNIVERSITY *of the*  
WESTERN CAPE